



## DEFENSE TECHNICAL INFORMATION CENTER

*Information for the Defense Community*

DTIC® has determined on 10/5/2010 that this Technical Document has the Distribution Statement checked below. The current distribution for this document can be found in the DTIC® Technical Report Database.

- ☒ **DISTRIBUTION STATEMENT A.** Approved for public release; distribution is unlimited.
- ☐ **© COPYRIGHTED;** U.S. Government or Federal Rights License. All other rights and uses except those permitted by copyright law are reserved by the copyright owner.
- ☐ **DISTRIBUTION STATEMENT B.** Distribution authorized to U.S. Government agencies only (fill in reason) (date of determination). Other requests for this document shall be referred to (insert controlling DoD office)
- ☐ **DISTRIBUTION STATEMENT C.** Distribution authorized to U.S. Government Agencies and their contractors (fill in reason) (date of determination). Other requests for this document shall be referred to (insert controlling DoD office)
- ☐ **DISTRIBUTION STATEMENT D.** Distribution authorized to the Department of Defense and U.S. DoD contractors only (fill in reason) (date of determination). Other requests shall be referred to (insert controlling DoD office).
- ☐ **DISTRIBUTION STATEMENT E.** Distribution authorized to DoD Components only (fill in reason) (date of determination). Other requests shall be referred to (insert controlling DoD office).
- ☐ **DISTRIBUTION STATEMENT F.** Further dissemination only as directed by (inserting controlling DoD office) (date of determination) or higher DoD authority.
- Distribution Statement F is also used when a document does not contain a distribution statement and no distribution statement can be determined.*
- ☐ **DISTRIBUTION STATEMENT X.** Distribution authorized to U.S. Government Agencies and private individuals or enterprises eligible to obtain export-controlled technical data in accordance with DoDD 5230.25; (date of determination). DoD Controlling Office is (insert controlling DoD office).



DYNAMIC COUPLING OF  
QUASI-ELECTROSTATIC THUNDERCLOUD  
FIELDS TO THE MESOSPHERE  
AND LOWER IONOSPHERE:  
SPRITES AND JETS

Victor Petrovich Pasko

July, 1996

20100827413

**DYNAMIC COUPLING OF  
QUASI-ELECTROSTATIC THUNDERCLOUD  
FIELDS TO THE MESOSPHERE  
AND LOWER IONOSPHERE:  
SPRITES AND JETS**

A DISSERTATION  
SUBMITTED TO THE DEPARTMENT OF ELECTRICAL ENGINEERING  
AND THE COMMITTEE ON GRADUATE STUDIES  
OF STANFORD UNIVERSITY  
IN PARTIAL FULFILLMENT OF THE REQUIREMENTS  
FOR THE DEGREE OF  
DOCTOR OF PHILOSOPHY


By  
Victor Petrovich Pasko

July, 1996

© Copyright by Victor Petrovich Pasko 1996  
All Rights Reserved



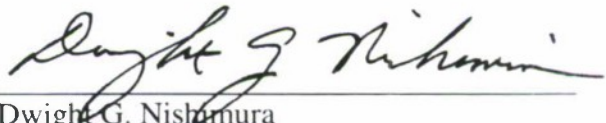
I certify that I have read this dissertation and that in my opinion it is fully adequate, in scope and quality, as a dissertation for the degree of Doctor of Philosophy.

  
\_\_\_\_\_  
Umran S. Inan (Principal Advisor)

I certify that I have read this dissertation and that in my opinion it is fully adequate, in scope and quality, as a dissertation for the degree of Doctor of Philosophy.

  
\_\_\_\_\_  
Timothy F. Bell

I certify that I have read this dissertation and that in my opinion it is fully adequate, in scope and quality, as a dissertation for the degree of Doctor of Philosophy.

  
\_\_\_\_\_  
Dwight G. Nishimura

Approved for the University Committee on Graduate Studies:

\_\_\_\_\_

*This dissertation is dedicated to my mother and father*

Valentina and Petr

*and to my wife*

Tanya

*and daughter*

Sasha

# Contents

<b>Abstract</b>	v
<b>Preface</b>	vii
<b>Contents</b>	x
<b>Tables</b>	xiii
<b>Illustrations</b>	xiv
<b>1 Introduction</b>	1
1.1 Upward Electrodynamic Coupling of Thunderstorms .....	2
1.1.1 Experimental Evidence .....	3
1.1.2 Theoretical Mechanisms .....	3
1.2 Optical Flashes Above Thunderstorms .....	6
1.2.1 First Recorded Image .....	6
1.2.2 Observations from Space Shuttle .....	6
1.2.3 Observations During Summer 1993 .....	9
1.2.4 Terminology for Optical Flashes Above Thunderstorms .....	11
1.2.5 Observations of Sprites During Summer 1994 .....	12
1.2.6 Observations of Sprites During Summer 1995 .....	14
1.2.7 Photometric Properties of Sprites .....	15
1.2.8 Spectral Properties of Sprites .....	18
1.2.9 Observations of Blue Jets During Summer 1994 .....	21

1.3	Scientific Contributions .....	24
<b>2</b>	<b>Quasi-Electrostatic Heating Model</b>	<b>25</b>
2.1	Electric Field and Charge Density .....	25
2.2	Lightning Current and Charge .....	30
2.3	Ambient Conditions in the Atmosphere and Lower Ionosphere .....	32
2.4	Selfconsistent Evaluation of Conductivity .....	34
2.4.1	Electron Mobility .....	34
2.4.2	Ionization Coefficient .....	35
2.4.3	Attachment Coefficient .....	37
2.4.4	Electron Density .....	38
2.5	Optical Emissions .....	39
2.6	Limitations of Analytical Models .....	42
<b>3</b>	<b>Heating, Ionization and Optical Flashes in the Mesosphere</b>	<b>43</b>
3.1	Physical Mechanism .....	43
3.2	Model Parameters .....	44
3.3	Electric Field and Charge Density .....	46
3.4	Ionization and Attachment .....	49
3.5	Optical Emissions .....	52
3.6	Electron and Ion Conductivity .....	58
3.7	Lightning Discharge Duration .....	59
3.8	Lightning Discharge Type .....	62
3.9	Thundercloud Charge Geometry .....	64
3.10	Relaxation Times of Quasi-Electrostatic Fields .....	66
<b>4</b>	<b>Sprites as Luminous Columns of Ionization</b>	<b>71</b>
4.1	Physical Mechanism .....	71
4.2	Model Parameters .....	73
4.3	Electron Density .....	74
4.4	Electric Field .....	75
4.5	Optical emissions .....	77
4.6	Current and Charge Transfer to the Ionosphere .....	79
4.7	Comparison With Observations of Sprites .....	80
4.7.1	Comparison With Video Observations .....	80

4.7.2	Comparison With Photometric Observations .....	82
4.7.3	Comparison With Spectroscopic Observations .....	83
4.8	Sprites and Runaway Electrons .....	84
<b>5</b>	<b>Blue Jets Produced by Pre-Discharge Thundercloud Fields</b>	<b>89</b>
5.1	Physical Mechanism .....	89
5.1.1	Blue Jets as Streamers .....	90
5.1.2	Formation of Blue Jets .....	91
5.2	Model Parameters .....	93
5.3	Electron Number Density, Electric Field and Current .....	96
5.4	Optical Emissions .....	98
5.5	Comparison with Video Observations of Blue Jets .....	100
5.5.1	Geometrical Shape and Velocity of Blue Jets .....	100
5.5.2	Brightness and Color of Blue Jets .....	100
5.6	Blue Jets and Runaway Electrons .....	101
<b>6</b>	<b>Summary and Suggestions for Future Research</b>	<b>103</b>
6.1	Summary of Results .....	103
6.2	Suggestions for Future Research .....	106
<b>A</b>	<b>Comparison with Kinetic Solutions and Swarm Experiments</b>	<b>109</b>
A.1	Electron Mobility .....	110
A.2	Ionization and Attachment Coefficients .....	110
A.3	Optical Emissions .....	112
A.4	Vibrational Excitation of Molecular Nitrogen .....	112
A.5	Average Electron Energy .....	113
<b>B</b>	<b>Comparison with Auroral Optical Emissions</b>	<b>115</b>
	<b>Bibliography</b>	<b>119</b>

# Tables

2.1	Approximation Coefficients. ....	40
3.1	Video response scaling factors. ....	55

# Illustrations

1.1	Phenomena and mechanisms. ....	5
1.2	The first TV image of an optical flash above thunderstorms [ <i>Franz et al.</i> , 1990]. ....	7
1.3	Observations of optical flashes above thunderstorms from the space shuttle [ <i>Boeck et al.</i> , 1995]. ....	8
1.4	An optical flash observed from the ground by <i>Lyons</i> [1994]. ....	10
1.5	An optical event recorded on color video from an aircraft [ <i>Sentman et al.</i> , 1995]. ....	12
1.6	A bright sprite event recorded on the night of July 11-12, 1994 by <i>Winckler et al.</i> [1996]. ....	14
1.7	A collage of three sprite images obtained by <i>Rairden and Mende</i> [1995]. ..	15
1.8	Photometer and sferic traces for a sprite event [ <i>Winckler et al.</i> , 1996]. ....	16
1.9	Lightning-induced transient luminous event [ <i>Fukunishi et al.</i> , 1996]. ....	19
1.10	Spectral scan of a sprite [ <i>Mende et al.</i> , 1995]. ....	20
1.11	Reduced spectrum of a sprite [ <i>Hampton et al.</i> , 1996]. ....	21
1.12	Two images of Blue Jets obtained from an aircraft during summer 1994 Sprites campaign [ <i>Wescott et al.</i> , 1995a]. ....	22



2.1	Thundercloud charge removal models. ....	26
2.2	Thundercloud charge dynamics corresponding to different models. ....	27
2.3	Coordinate system used in calculations. ....	28
2.4	Ambient electron density and ion conductivity. ....	33
2.5	Electron mobility. ....	35
2.6	Ionization and dissociative attachment. ....	36
2.7	Optical excitation coefficients. ....	40
3.1	Physical mechanism of mesospheric optical flashes. ....	45
3.2	Temporal variation of the quasi-static electric field. ....	47
3.3	Electric field and charge density. ....	48
3.4	Model results for electron density and conductivity. ....	50
3.5	Model results for effective electron collision frequency. ....	51
3.6	Space-time dynamics of optical emissions. ....	53
3.7	Optical emission intensity as a function of wavelength. ....	54
3.8	The distribution of time-averaged optical emission intensity. ....	56
3.9	Instantaneous optical emission intensity. ....	57
3.10	Dependence on the ambient electron density. ....	59
3.11	Dependence on the different ambient ion conductivity. ....	59
3.12	Model results for different discharge durations and ambient conductivity profiles. ....	60
3.13	Results for three different models of lightning discharge. ....	62
3.14	Dependence on the type of lightning discharge. ....	63
3.15	Dependence on the thundercloud charge geometries. ....	64

3.16	Relaxation of the quasi-electrostatic field. ....	66
3.17	One dimensional relaxation of the electric field. ....	69
4.1	Models of charge removal. ....	74
4.2	Formation and downward propagation of an ionization channel. ....	76
4.3	Time averaged optical emission intensity. ....	78
4.4	Optical emission intensity for selected bands and corresponding video response. ....	81
4.5	Spatially integrated optical emission intensity as a function of time. ....	83
4.6	Optical emissions produced by runaway electrons. ....	86
5.1	Mechanism of Blue Jets. ....	92
5.2	Electric field and electron density associated with a blue jet. ....	97
5.3	Optical emission intensity associated with a blue jet. ....	99
5.4	Optical emission intensity for different optical bands. ....	99
5.5	Spatially integrated optical emission intensity as a function of time. ....	100
A.1	Comparison of analytical approximations with kinetic solutions and results of swarm experiments. ....	111
B.1	Comparison with auroral optical emissions. ....	116

# Abstract

Red Sprites and Blue Jets are two different types of recently discovered optical flashes observed above large thunderstorm systems. Sprites are luminous glows occurring at altitudes typically ranging from  $\sim 50$  to  $90$  km. In video they exhibit a red color at their top which gradually changes to blue at lower altitudes. Sprites may occur singly or in clusters of two or more. The lateral extent of “unit” sprites is typically  $5$ - $10$  km and they endure for several milliseconds. Jets are upward moving ( $\sim 100$  km/s) highly collimated beams of luminosity, emanating from the tops of thunderclouds, extending up to  $\sim 50$  km altitude and exhibiting a primarily blue color.

We propose that sprites result from large electric field transients capable of causing electron heating, breakdown ionization and excitation of optical emissions at mesospheric altitudes following the removal of thundercloud charge by a cloud-to-ground discharge. Depending on the history of charge accumulation and removal, and the distribution of ambient atmospheric conductivity, the breakdown region may have the shape of vertically oriented ionization column(s). Results of a two-dimensional and selfconsistent quasi-electrostatic (QE) model indicate that most of the observed features of sprites can be explained in terms of the formation and self-driven propagation of streamer type channels of breakdown ionization. Comparison of the optical emission intensities of the 1st and 2nd positive bands of  $N_2$ , Meinel and 1st negative bands of  $N_2^+$ , and the 1st negative band of  $O_2^+$  demonstrates that the 1st positive band of  $N_2$  is the dominant optical emission in the altitude range  $\sim 50$ - $90$

km, which accounts for the observed red color of sprites. Optical emissions of the 1st and 2nd positive bands of  $N_2$  occur in carrot-like vertical structures with typical transverse dimension  $\sim 5$ -10 km which can span an altitude range from  $\sim 80$  km to well below  $\sim 50$  km. The appearance of optical emissions associated with sprites can be delayed in time ( $\sim 1$ -20 ms) with respect to the causative cloud to ground discharge. Theoretical model results are found to be in good agreement with recent video, photometric and spectral measurements of sprites.

We propose that blue jets are streamer type processes occurring on an atmospheric spatial scale during the charge accumulation stage in a thundercloud prior to lightning discharges. The quasi-electrostatic model produces results in general agreement with most features of jets as observed in video. Results indicate that the velocity of upward propagation of jets is  $\sim 100$  km/s, and that the general shape of jets is in the form of upward expanding beams of luminosity with cone angles  $< 30^\circ$ . The model results agree with video observations showing that the brightness of jets drops  $\sim 2$  orders of magnitude between the lower part and the tip of the jet, and the fact that the luminosity fades away simultaneously everywhere along the cone of the jet. The blue color of jets as observed in video is naturally explained as emission from the 2nd positive band of  $N_2$  excited by electron impact. Jets are not necessarily associated with lightning discharges and may appear only in relatively rare cases of large ( $\sim 300$ -400 coulombs) thundercloud charge accumulation at high ( $\sim 20$  km) altitudes. Jets occur during the accumulation phase of the thundercloud charge, so that it is not necessary for large amounts of charge to be removed in order to produce them.

# Preface

It has been a great privilege for me to spend the last four years as a graduate student and research assistant with the VLF group at STAR Laboratory of Stanford University.

I would like to thank Professor Umran Inan, my principal advisor, for his trust, guidance and encouragement during the course of this research. I deeply appreciate his infectious energy, enthusiasm, and ability to see and formulate new and exciting physical problems, some of which constituted the basis for this dissertation work. I also would like to express gratitude for his extreme patience and moral support during crucial periods of my studies at Stanford and this dissertation research.

Sincere appreciation is also expressed to Dr. Timothy Bell, my associate advisor, for his invaluable ideas, suggestions and comments at various stages of this work. The door of his office was always open for me, and he was always ready to discuss new physical ideas for many hours, even if I dropped in at 1 a.m. in the morning.

I have thoroughly enjoyed many conversations with Professors Robert Helliwell and Don Carpenter, and especially with Professor Martin Walt, and are grateful to them for their persistent interest in my work and critical reading and commenting on my papers before they were submitted for publication.

I would like to express my appreciation to Professor Thomas Kailath for his chairing my oral defense committee, and to Professor Dwight Nishimura for his careful reading and



commenting on this dissertation, despite their very busy schedules. I would like to express my thanks also to Professors Antony Fraser-Smith and Leonard Tyler for serving on the committee for my Ph.D. defense, as well as their instruction and continual friendly support during my years at Stanford.

I would like to thank Dr. Yuri Taranenko for many fruitful discussions on topics related to this research, for his contributions of valuable ideas, and for his help during my work on the optical part of this dissertation.

I am grateful for discussions on various topics and the help I received from the late Professor Oscar Buneman, Professor Vikas Sonwalkar, Mr. Jerry Yarbrough and Mr. Bill Trabucco, and present and former students of the VLF group: Juan Rodriguez, Bill Burgess, Jasna Ristic-Djurovic, Tom Mielke, Dave Shafer, Alan Brown, Jay Littlefield, Alex Slingeland, Kyle Walworth, Wes Sampson, Dave Lauben, Sean Lev-Tov, Steve Cummer, Steve Reising, Mike Johnson, Chris Barrington-Leigh, Nikolai Lehtinen, Craig Heinselman, Jeff DiCarlo, Frank Kolor, and Josh Snodgrass.

The TeX macros software which has been used to typeset this dissertation was written by Dr. Bill Burgess to whom I am grateful for saving me a lot of time. I would like also to thank Mrs. June Wang for her valuable everyday help with administrative work.

This dissertation would not have become a reality without the knowledge and experience which I had acquired before my Stanford years back in Kiev, Ukraine. I am very grateful to my high school teacher Dr. Yuri Belyavsky who infected me with a love of physical science. I would like to sincerely thank my first scientific advisor Dr. Sergey Silich who put his knowledge, energy and trust in me, resulting in the publication of my first scientific paper more than ten years ago during my student years at Kiev University. I gratefully acknowledge the contribution of my former advisor Professor Nikolay Kotsarenko, and my former colleagues Georgy Lizunov, Slava Glukhov, and Anisim Silivra from Kiev University. I also significantly benefited from scientific collaboration with Drs. Vitaly Chmyrev

and David Shklyar of the Institute of Terrestrial Magnetism, Ionosphere and Radio Wave Propagation (IZMIRAN) from Troitsk, Moskow Region.

I wish to express special gratitude to my friends and colleagues Drs. Yuri Taranenko and Sasha Draganov who helped me in initiating an exciting scientific collaboration with the VLF group of Stanford University. My special thanks are directed to Drs. Vitaly Chmyrev and David Shklyar who introduced me to Professor Umran Inan in October 1991 during his visit to Russia, starting a completely new and absolutely fantastic page in my life.

I am grateful to Mr. Tom Sege, Mrs. Nancy Okimoto, Drs. Sasha Draganov and Yuri Taranenko, for the organization of financial support which helped me to reunite with my wife and child during the first several months of my studies at Stanford. I sincerely appreciate the friendly everyday support which me and my family received from Sasha and Yuri and their families during our years at Stanford.

My special thanks are directed to Mrs. Glenna Violette and Mr. Joe Violette and to their large and very nice family, especially to their daughters Corinne and Sharm, who supported me and my family in many different ways for all these four years starting from the very first day after my arrival in this country. I deeply appreciate the help of Mr. and Mrs. Violette in bringing my wife and child to Stanford soon after the start of my studies here.

This dissertation is dedicated to my mother Valentina Pasko, my father Petr Pasko, to my wife Tanya, and my daughter Sasha. A brief paragraph here cannot begin to express the gratitude due them for their love, patience and moral support through the course of my academic years.

VICTOR P. PASKO

*Stanford, California*  
*July 4, 1996*

This research was supported by the National Aeronautics and Space Administration under grants NAGW-2871 and NAGW-2871-2, and by the National Science Foundation under grant ATM-9113012 to Stanford University.



# 1

## Introduction

In this introductory chapter we briefly survey the information available concerning the recently discovered phenomena of optical flashes above thunderstorms, spanning the altitude range from cloud tops and up to the lower edge of the ionosphere ( $\sim 90$  km), and referred to as “sprites” and “blue jets”.

Sprites are luminous glows occurring at altitudes typically ranging from  $\sim 50$  to  $90$  km. In video, they exhibit a red color at their top which gradually changes to blue at lower altitudes. Sprites may occur singly or in clusters of two or more [Sentman *et al.*, 1995]. The lateral extent of “unit” sprites is typically  $5$ - $10$  km and they endure for several milliseconds. Blue jets or jets in short are upward moving ( $\sim 100$  km/s) highly collimated beams of luminosity, emanating from the tops of thunderclouds, extending up to  $\sim 50$  km altitude and exhibiting a primarily blue color [Wescott *et al.*, 1995a].

The intent of this introductory survey is to give the reader a general understanding of the observed properties of the phenomenon of sprites and jets which constitute an important component of the complex of physical processes which are not yet fully understood and which manifest upward electrodynamic coupling of energy originating in tropospheric thunderstorms to the mesosphere and lower ionosphere. The scope of this dissertation work and the specific contributions to knowledge are discussed at the end of this chapter in Section 1.3.

## 1.1 UPWARD ELECTRODYNAMIC COUPLING OF THUNDERSTORMS

A thunderstorm is the final product of the growth of a series of clouds which are formed through the upward transfer of energy from surface heating effects leading to buoyant vertical air motions or through the lifting effects associated with the motion of atmospheric frontal weather zones. The thunderstorm electromagnetic activity is spectacular and dangerous, in spite of the fact that it represents an energy expenditure of less than 1% of the thermal, gravitational, and kinetic energy associated with condensation of moisture and the development of drafts and precipitation [*Braham, 1952*].

The importance of tropospheric thunderstorms in the coupling of electromagnetic energy to the upper atmospheric regions on a global scale is underscored by the fact that the thunderstorms and associated lightning activity are the generators which maintain the more than  $5 \times 10^5$  Coulombs of the earth's charge against the conduction loss due to the total global current of  $\sim 1800$  A flowing through the conducting atmosphere in fair weather regions [e.g., *Stergis, 1957*]. There are more than 2000 thunderstorms active at any given time over the Earth's surface and on average lightning strikes the Earth  $\sim 100$  times per second [*Volland, 1984*]. On the order of 1000 coulombs of bound space charge are separated and maintained during the late growth and active periods of a thunderstorm [e.g., *Marshall et al., 1996*] with cloud-to-ground lightning discharges involving the transfer to the ground of up to 300 coulombs of charge in several ms [*Brook et al., 1982*], leading to large quasi-electrostatic (QE) fields which exist in the mesosphere and lower ionosphere regions over millisecond time scales. These fields, combined with intense electromagnetic pulses (EMP) of  $\sim 20$  Gigawatts peak power [*Uman, 1987, p.115*] generated by lightning currents, are thought to intensely heat the ambient electrons [*Inan et al., 1996b*, and references therein] and accelerate energetic runaway electrons (REL) [*Roussel-Dupre et al., 1994; Bell et al., 1995*], producing ionization and optical emissions.

### 1.1.1 Experimental Evidence

The experimental evidence indicating strong upward electrodynamic coupling of thunderstorms to the mesosphere and lower ionosphere includes early/fast perturbations of subionospherically propagating VLF signals associated with lightning discharges in underlying thunderstorms [Armstrong, 1983; Inan *et al.*, 1988; 1993; 1995; 1996a; Dowden *et al.*, 1994], and optical emissions in clear air above thunderstorms associated with sprites [e.g., Sentman *et al.*, 1995; Lyons, 1994, 1995, 1996; Boeck *et al.*, 1995; Rairden and Mende, 1995; Winckler *et al.*, 1996] and blue jets [Wescott *et al.*, 1995a] and airglow enhancements [Boeck *et al.*, 1992]. The latter are believed to be closely associated with recently discovered rapid ( $< 1$  ms) optical emissions at 80-95 km altitudes with lateral extents up to 300 km preceding sprites and referred to as “elves” [Fukunishi *et al.*, 1996; Lyons, 1996; Inan *et al.*, 1996b]. Sprites are clearly associated both temporally and spatially with intense lightning discharges in underlying thunderstorms [Boccippio *et al.*, 1995] as well as with early/fast VLF events [Inan *et al.*, 1995] providing strong evidence of significant changes in the mesospheric electrical conductivity. Sprites are almost uniquely associated with positive cloud-to-ground lightning discharges [Boccippio *et al.*, 1995; Winckler *et al.*, 1996; Lyons, 1996]. The first observations of gamma ray bursts of terrestrial origin [Fishman *et al.*, 1994], associated with positive cloud-to-ground lightning discharges [Inan *et al.*, 1996c], and intense wideband VHF bursts [e.g., Holden *et al.*, 1995] constitute additional new examples of upward coupling of energy originating in thunderstorms.

### 1.1.2 Theoretical Mechanisms

The new observations listed above have led to the discovery of new interaction mechanisms which result in troposphere-mesosphere/lower ionosphere coupling. These mechanisms are based on heating of the ambient electrons by electromagnetic pulses generated by lightning discharges [Inan *et al.*, 1991, 1996b; Taranenko *et al.*, 1993a,b; Milikh *et al.*, 1995; Rowland *et al.*, 1995] or by large quasi-electrostatic thundercloud fields [Pasko *et al.*, 1995; 1996a,b,c; Boccippio *et al.*, 1995; Winckler *et al.*, 1996], and on runaway electron processes [Bell



*et al.*, 1995; Winckler *et al.*, 1996; Roussel-Dupre and Gurevich, 1996; Taranenko and Roussel-Dupre, 1996]. It has been proposed by Inan *et al.* [1996d] that quasi-electrostatic thundercloud fields are capable to maintain the ionospheric electrons at a persistently heated level well above their ambient thermal energy. Changes in the thundercloud charge (e.g., in lightning discharges) lead to heating/cooling above/below this quiescent level, and are registered as early/fast VLF events [Inan *et al.*, 1996d]. The simultaneous observations of early/fast VLF events and sprites [Inan *et al.*, 1995], indicate that these two effects may be a manifestation of the same physical process consistent with model predictions of both optical emissions, heating and ionization changes associated with quasi-electrostatic thundercloud fields [Pasko *et al.*, 1995, 1996a,b; Inan *et al.*, 1996d]. Some of these physical processes are illustrated in Figure 1.1.

It should be noted that in existing scientific literature the possibility of breakdown ionization of the upper atmosphere by thundercloud fields was first mentioned in 1925 by *C.T.R. Wilson*. He recognized that the relation between the thundercloud electric field which decreases with altitude  $z$  as  $\sim z^{-3}$  and the critical breakdown field which falls more rapidly (being proportional to the exponentially decreasing atmospheric density) leads to the result that “there will be a height above which the electric force due to the cloud exceeds the sparking limit” [Wilson, 1925]. Three decades later *Wilson* speculated that a discharge between the top of a cloud and the ionosphere might often be the normal accompaniment of a lightning discharge to ground [Wilson, 1956].

In this dissertation we investigate the heating, ionization, attachment and optical emission effects associated with intense quasi-electrostatic thundercloud fields existing above large thunderstorms before (producing blue jets) and after (generating sprites) lightning discharges. In the following section we provide a brief description of the phenomenology of optical flashes above thunderstorms on the basis of selected results of video, photometric and spectroscopic measurements.

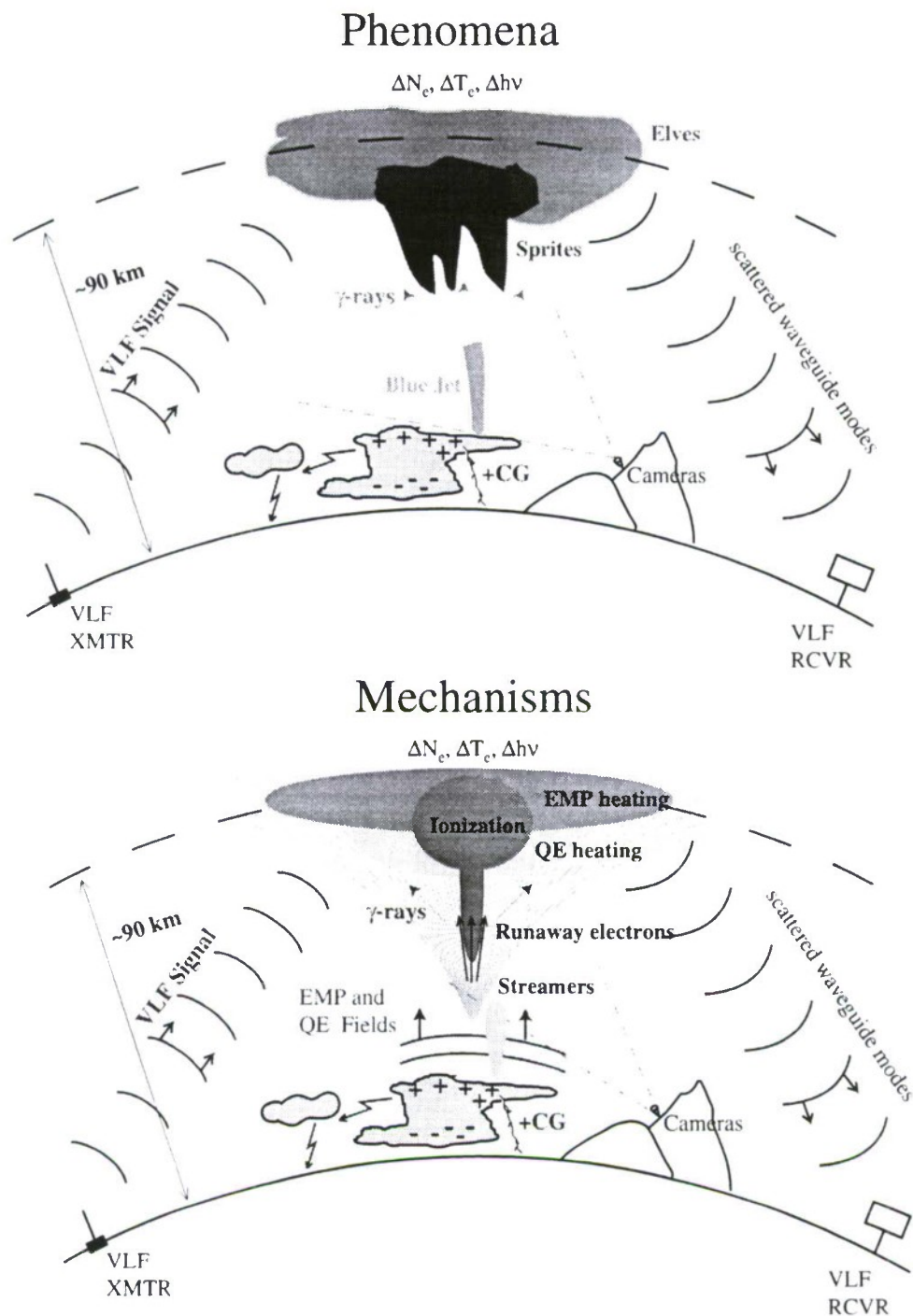


**Fig. 1.1. Phenomena and mechanisms.** Illustration of different phenomena (*top panel*) and theoretical mechanisms (*bottom panel*) of lightning-ionsphere interactions operating at different altitudes and producing optical emissions ( $\Delta\nu$ ) observed as sprites, blue jets and elves, as well as heating ( $\Delta T$ ) and ionization changes ( $\Delta N_e$ ) detected as very low frequency (VLF) signal changes.

## 1.2 OPTICAL FLASHES ABOVE THUNDERSTORMS

The most spectacular evidence of electrodynamic coupling between tropospheric lightning and the overlying mesosphere/lower ionosphere are luminous glows above thunderstorms occurring at altitudes ranging from the cloud-tops to  $\sim 90$  km. Visual accounts of this kind of glow in the clear air above thunderstorms have appeared in the literature since the 19th century, the most vivid accounts being those by air transport pilots [Vaughan and Vonnegut, 1989]. Although most of these reports probably described the known phenomena of lightning channels which terminate in the clear air rather than in the cloud [e.g., Malan, 1963, p. 6; Uman, 1969, p. 2], there were exceptional cases that differed from the description of a typical air discharge. In retrospect, these unusual diffuse optical events are likely to have been associated with recently documented optical flashes above thunderstorms called sprites and jets.

### 1.2.1 First Recorded Image

The first recorded image of unusual optical flashes occupying large volumes of space above thunderstorms was obtained serendipitously on 5 July 1989 during a test of a low-light-level TV camera at the O'Brien Observatory of the University of Minnesota near Minneapolis. This observation is described by Franz *et al.* [1990], and a reproduction of the image from this paper is shown in Figure 1.2.

### 1.2.2 Observations from Space Shuttle

Following the original observation by Franz *et al.* [1990], Vaughan *et al.* [1992] and Boeck *et al.* [1995] reported video observations from the space shuttle of tens of similar optical events. Most of the video examples captured from space have the appearance of thin luminous filaments of glowing gases stretching into the stratosphere above thunderstorm [Boeck *et al.*, 1995]. Some of the video images obtained from the space shuttle [Vaughan *et al.*, 1992; Boeck *et al.*, 1995] are reproduced in Figure 1.3.



**Fig. 1.2. The first TV image of an optical flash above thunderstorms** [Franz *et al.*, 1990]. Low-light-level TV image of a luminous electrical discharge over a thunderstorm  $\sim 250$  km from the observing site. The image, which persisted less than one video frame ( $< 30$  ms), resembled two plume discharges simultaneously extending into the clear sky above thunderstorm. The image is taken from <http://www.ghcc.msfc.nasa.gov/skeets.html> [Courtesy of Dr. O. H. Vaughan, Jr.].

Typical heights of optical flashes were estimated to be 60 to 75 km above the earth with the uncertainty arising from the rather coarse resolution of the digitized image and from the lack of information on the cloud top height or the location at which the stratospheric flash intersects the cloud top [Boeck *et al.*, 1995]. The lateral width of observed luminosities varied considerably between events, with some examples showing thin or several thin vertical filaments while others appearing as broad columns of some kilometers across. In addition, many events exhibited a bulge of luminosity at the top of the flash with dimensions of order of kilometers [Boeck *et al.*, 1995]. The full vertical extent of the flashes were only observable within the time resolution of one video field (17 ms) [Boeck *et al.*, 1995]. It appears from the space shuttle observations that the conditions for the stratospheric flashes may occur over most regions of the globe (in temperate and tropical areas, over the oceans, and over the land) and that the luminosity is definitely associated with a discharge in the cloud below and occurs soon after the onset of the discharge [Boeck *et al.*, 1995].



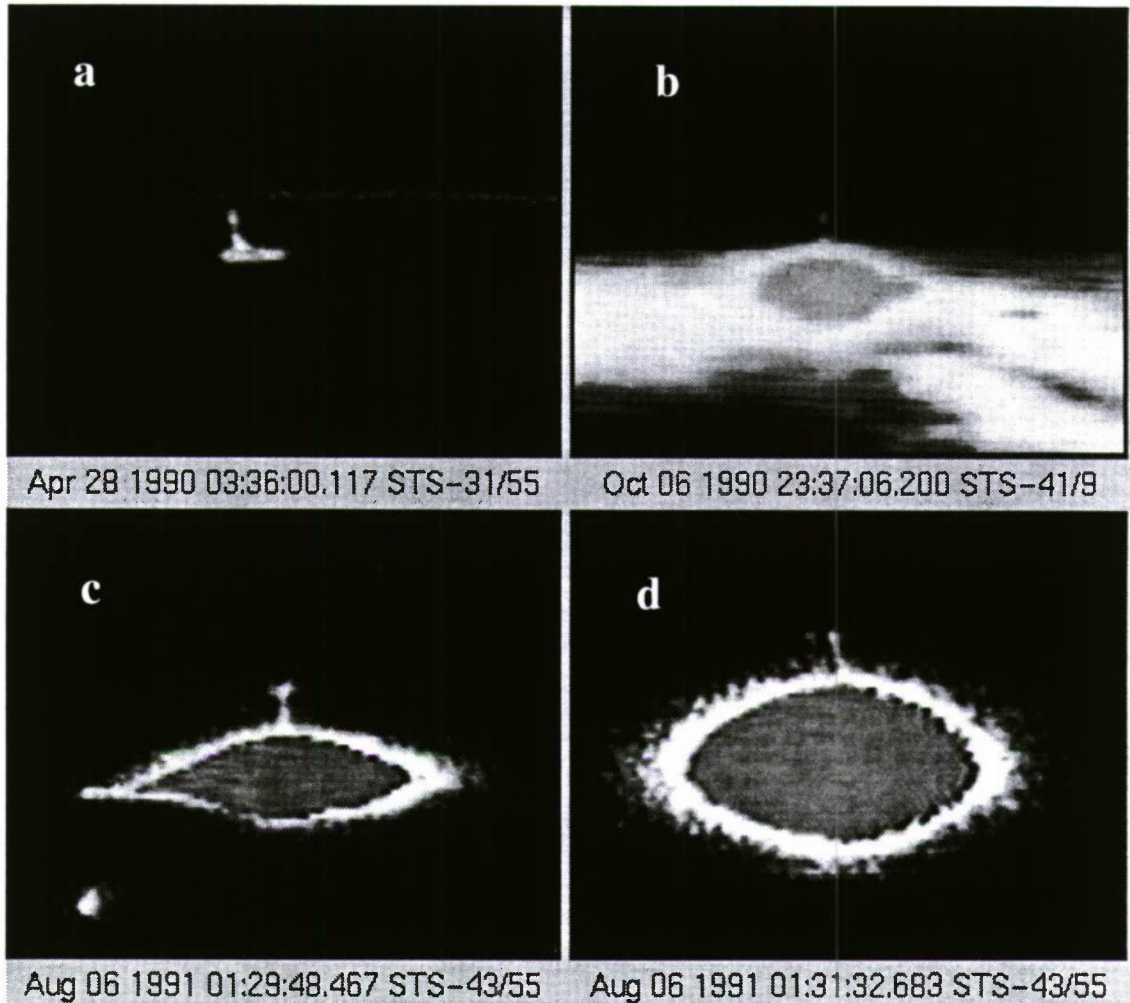


**Fig. 1.3. Observations of optical flashes above thunderstorms from the space shuttle [Boeck *et al.*, 1995].** A single captured image from each stratospheric flash: (a) A distinct bulge or blob of illumination at the upper end of the stratospheric flash. This perception of an upper bulge is further enhanced in this and other cases by the break in the illumination found just below the upper bulge. The length of the vertical column was estimated to be approximately 31 km [Vaughan *et al.*, 1992]; (b) A single-filament stratospheric flash, with a single break in illumination, and a bulge of illumination at the top observed on October 6, 1990, at 23:37:06 UTC. The flash extended above the horizon; (c) A stratospheric flash (01:29:48 UTC) illustrates very clearly a fan-shaped structure at the top of the filament; (d) A double-filament stratospheric flash observed two minutes following previous event (c). The image is taken from <http://wwwghcc.msfc.nasa.gov/skeets.html> [Courtesy of Dr. O. H. Vaughan, Jr.].

### 1.2.3 Observations During Summer 1993

During the summers of 1993-1994 there occurred a marked increase in number of reports of optical flashes above thunderstorms.

Using a low light level all sky black and white television system, *Sentman and Wescott* [1993] imaged nineteen examples of optical flashes during a single flight of NASA's DC-8 airborne laboratory over thunderstorms in Iowa, Nebraska and Kansas in July, 1993. They estimated the terminal heights of the events to be 60 km, with error bars (due to unknown range) extending to 100 km. The duration of the flashes was estimated to be 16 ms or less, and the brightness as calculated from comparison with stellar brightness to be 25-50 kR, roughly that of moderately bright aurorae. The emission volume of flashes was estimated to be  $> 1000 \text{ km}^3$ , with a horizontal extent of  $\sim 10\text{-}50 \text{ km}$  and their occurrence rate was such that an optical flash was observed in association with every 200-300th cloud-to-ground stroke.

In a ground-based program in the high plains area of Fort Collins, Colorado, *Lyons* [1994] obtained black and white images of high altitude flashes above storm systems in Nebraska and Kansas in July and August, 1993. An image-intensified, low-light video camera systematically monitored the stratosphere above distant (100-800 km range) mesoscale convective systems over the high plains of the central United States for 21 nights between 6 July and 27 August 1993. Complex, luminous structures were observed above large thunderstorm clusters on eleven nights, with one storm system (7 July 1993) yielding 248 events in 410 minutes. The duration of events ranged from 33 to 283 ms, with an average of 98 ms. The luminous structures, generally not visible to the naked, dark-adapted eye, exhibited on video a wide variety of brightness levels and shapes including streaks, aurora-like curtains, smudges, fountains and jets. The structures were often more than 10 km wide and their upper portions extended to above 50 km altitude. Some of the shapes appeared to be "frozen in space" as if "illuminated" during the few video fields in which they were visible. The video images, with a time resolution of 17 ms per video field, did not provide any sense of



**Fig. 1.4. An optical flash observed from the ground by Lyons [1994].** The event observed at 0607 UTC on July 7, 1993. The distant storm cloud top heights are estimated to be between 10 and 15 km altitude. If so, the uppermost extent of the structures would be from 50 to 65 km altitudes [Lyons, 1994]. The image is taken from <http://www.ghcc.msfc.nasa.gov/skeets.html> [Courtesy of Dr. O. H. Vaughan, Jr.].

propagation either upward or downward. Figure 1.4 illustrates a typical image of an optical flash observed on July 7, 1993 [Lyons, 1994].

With heights reaching towards 100 km and diameters of 20 km or more, assuming circular symmetry suggests that the larger luminous structures can attain emission volumes of thousands of cubic kilometers. While the mesoscale convective system as a whole is electrically active, mesospheric optical flashes tend to occur in regions characterized by low cloud-to-ground flash rates where positive cloud-to-ground flashes are more common [Lyons, 1994].

Winckler [1995] observed more than 150 optical flashes above a thunderstorm complex moving south-east across the state of Iowa during the night of 9-10 August 1993. Black and white images were obtained through clear air with an intensified CCD TV cameras at the O'Brien Observatory of the University of Minnesota located about 60 km north east of Minneapolis and 250-500 km from the storm center. The optical flashes consisted of

bright vertical striations extending from 50-80 km altitude, often covering tens of kilometers laterally, with tendrils of decreasing intensity visible in the brighter events down to the cloud tops below 20 km altitude. All of the more intense events were coincident with a VLF sferic (i.e., powerful impulsive radio signal radiated by intense return stroke currents involved in a lightning discharge) measured in the 300Hz-12 kHz range, but smaller events often did not occur in association with a detectable sferic. The intense part of the events usually occurred within one TV field (16.7 ms). The brightness for the more intense events was estimated to be 50-100 kR.

Comparison of results obtained with those reported by *Vaughan et al.* [1992], *Sentman and Wescott* [1993], and *Lyons* [1994] led *Winckler* to clearly conclude that all these authors were indeed observing the same phenomena [*Winckler*, 1995].

#### **1.2.4 Terminology for Optical Flashes Above Thunderstorms**

The optical flashes above thunderstorms have from the beginning been variously referred to in the literature as “upward”, “cloud-to-stratosphere”, or “cloud-to-ionosphere” lightning discharges. Use of these terms suggests of unwarranted parallels to normal tropospheric lightning, and also implies an upward direction of propagation which has not yet been determined [see discussion in *Lyons*, 1994 and *Sentman et al.*, 1995]. The term “sprite” has been suggested by D. Sentman [e.g., *Sentman et al.*, 1995] as non-judgmental as to the physics of the phenomenon and the specific production mechanisms. All of the above described optical flashes, including those observed from the space shuttle, might qualify for inclusion in the broad category of sprites.





**Fig. 1.5. An optical event recorded on color video from an aircraft** [Sentman *et al.*, 1995]. A sprite event (one of the largest) observed on 4 July 1994 at 0400:20 UT [Sentman *et al.*, 1995]. The original color image [Sentman *et al.*, 1995] is reproduced here in black and white. The image is taken from <http://www.ghec.msfc.nasa.gov/skeets.html> [Courtesy of Dr. O. H. Vaughan, Jr.].

### 1.2.5 Observations of Sprites During Summer 1994

The first color imagery of optical flashes above thunderstorms and their unambiguously triangulated physical dimensions and heights were obtained using observations from two jet aircraft [Sentman *et al.*, 1995; Wescott *et al.*, 1995a; Sentman and Wescott, 1994, 1995]. Low light level television images, in both color and black and white, show that there are at least two distinctly different types of optical emissions spanning part or all of the distance between the anvil tops of the thunderclouds and the ionosphere. The first of these emissions, called sprites, are luminous structures of brief (typically  $< 16$  ms although some events endure longer) duration with a main body in red color that typically span the altitude range of 50-90 km, and lateral dimensions of 5-30 km. Faint bluish tendrils often extended downward from the main body of sprites, occasionally appearing to reach the cloud tops near 20 km. Figure 1.5 shows one of the brightest events recorded during the campaign.

The brightest red region of a unit sprite, its “head”, lies between the characteristic altitudes

of 66 and 74 km. Above the head there is often a dark band ("hairline") above which a faint, wispy red glow ("hair") is observed to splay upward and outward toward terminal altitude. Beneath the head there sometimes occurs a dark band ("collar") at  $66 \pm 4$  km below which faint tendrils may extend downward to altitudes of 40-50 km, changing from red near the collar to blue at their lowest extremities. Sprites may occur singly, but more typically occur in clusters of two or more. Clusters may be tightly packed together into large structures 40 km or more across, or loosely spread out into distended structures of spatially separated sprites. The onset of luminescence occurs simultaneously (within video resolution of  $\sim 16$  ms) across the cluster as a whole, coincident with the occurrence of cloud-to-ground lightning below. All elements of the cluster typically decay in unison in 100-160 ms, but most of this decay time may be attributed to the image lag of the video cameras [Sentman *et al.*, 1995]. Sprites seem preferentially to occur on the backside of frontal storm systems, and occur in regions of positive lightning ground strokes.

Observations of sprites from the Yucca Ridge Field Station 29 km northeast of Fort Collins, Colorado, on the night of July 11-12, 1994 were performed by Winckler *et al.* [1996] using both wide-field and telescopic image-intensified CCD TV cameras, a telescopic photometer system and a 1 to 50 kHz broad band VLF sferic receiver. Telescopic TV images of bright sprites had a fan shaped upper plume with not well resolved fine features, as well as upward forked and vertically striated forms adjacent to these plumes and bright points of luminosity around the plume shaped regions. Many sprites consisted entirely of groups of vertically aligned striations which sometimes appeared to diverge from a common point of origin at cloud tops. All observed sprites were preceded by a cloud-to-ground stroke with a coincident sferic and sky flash. All cloud-to-ground strokes associated with sprites were positive, and most had 100 kA or more inferred peak current. Using the photometer data, the duration of sky flashes induced by the cloud-to-ground strokes was determined to be  $\sim 3$  ms and the additional sprite total light curve also endured for  $\sim 3$  ms. An image of a large bright sprite event recorded at 05:58:45.371 UT is shown in Figure 1.6. This sprite displays vertical

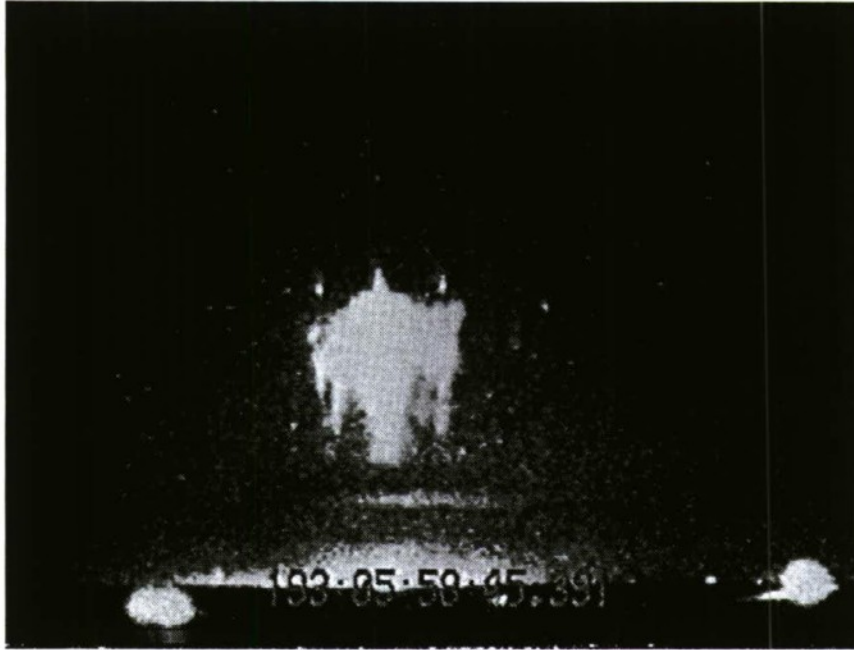


**Fig. 1.6.** A bright sprite event recorded on the night of July 11-12, 1994 by *Winckler et al.* [1996].

striations on each side of a central core. This sprite brightened in the next field (not shown) and greatly faded one video field later.

### **1.2.6 Observations of Sprites During Summer 1995**

Video images of sprites were obtained by *Rairden and Mende* [1995] with a CCD camera during a July 1995 ground-based campaign near Fort Collins, Colorado. These unfiltered intensified images reveal detailed spatial structure within the sprite envelope. The temporal resolution of the standard interlaced video imagery is limited by the 60 fields per second acquisition rate (16 ms). The specific CCD used here, however, is subject to bright events leaking into the readout registers, allowing time resolution on the order of the linescan rate (63  $\mu$ s). Typical sprite onset is found to follow the associated cloud-to-ground lightning by 1.5 to 4 ms. The onsets of the individual sprites within a cluster are generally, but not always, simultaneous to within 1 ms. Sprites tend to have a bright localized core, less than 2 km in horizontal dimension, which rises to peak intensity within 0.3 ms and maintains



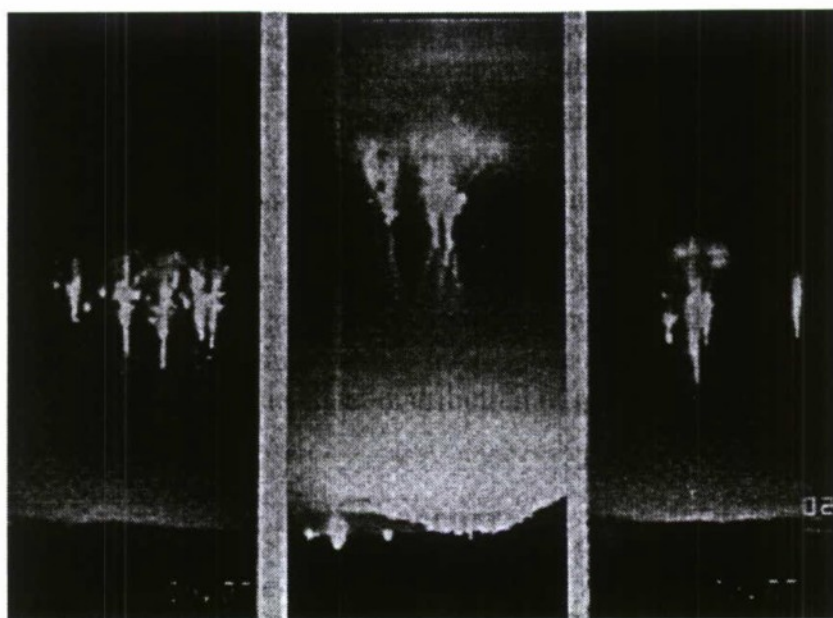


**Fig. 1.7.** A collage of three sprite images obtained by *Rairden and Mende [1995]*. The image is reproduced from [*Rairden and Mende, 1995*].

this level for 5 to 10 ms before fading over an additional 10 ms. Three examples of captured sprite images illustrating fine spatial structure are shown in Figure 1.7.

### **1.2.7 Photometric Properties of Sprites**

It was clear from the very first video observations that essentially all the temporal and spatial development of the sprites occurred within one  $\sim 16$  ms video field [*Winckler et al., 1996*]. Thus, photometric measurements are necessary to extract useful information on the temporal dynamics of sprites on time scales less than 16 ms.

*Winckler et al. [1996]* used a photometric system with high time resolution with the analog photomultiplier outputs sampled at 100 kHz rate. The sprites and associated cloud and sky flashes in each event were identified on the associated video images. Although the video provided only 16.7 ms timing accuracy, for most events millisecond timing accuracy could be obtained from the VLF sferic-photometer correlated responses [*Winckler et al., 1996*]. An example is shown in Figure 1.8, covering 30 ms of data which included a bright

sprite. The cloud-to-ground stroke sferic is coincident with the first rise of the photometer within 1 ms starting at 05:33:28.788 UT on July 12, 1994. The photometer trace is double peaked. *Winckler et al.* [1996] interpret the smaller initial 3 ms duration peak as Rayleigh scattered light in the sky due to the intense light of the cloud-to-ground discharge (termed sky flash in Figure 1.8) and the second larger peak 3 ms later as direct light of the sprite in the photometer field of view.

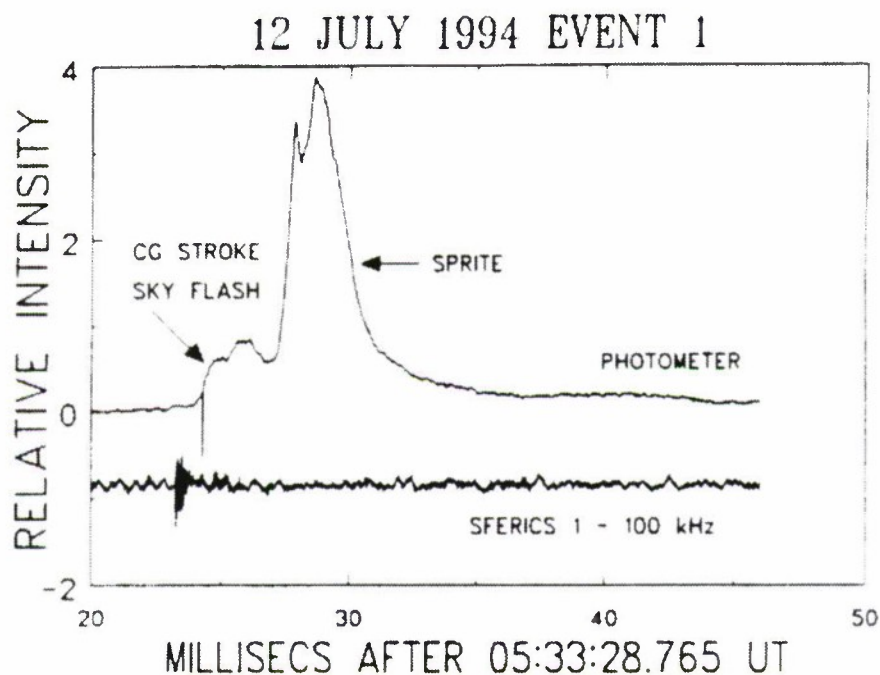


**Fig. 1.8. Photometer and sferic traces for a sprite event [Winckler et al., 1996].** The initial photometer response within 1 ms of the sferic is followed by a small maximum due to the scattered light from the cloud-to-ground stroke, and a large maximum due to the luminosity of the sprite. The figure is reproduced from [Winckler et al., 1996].

The puzzling feature that the total duration of video images of sprites was often longer than that indicated by the photometric data can be understood in terms of the different spectral response of the two instruments, coupled with the spectral time history of the sprite event.

The photometer used by *Winckler et al.* [1996] was blue sensitive with a response peaked at 450 nm. In contrast, the video photocathodes were red sensitive, with broad maximum extending to 850 nm. Results suggest that the sprite began with an intense, wideband optical flash covering both the blue and red portions of the spectrum. The video output, covering primarily the red portion of the spectrum, persisted for up to 10 video fields in contrast to the photometer output, primarily covering the blue region, which decayed on a time scale of one video field [*Winckler et al.*, 1996].

Observations of sprites and related optical phenomena were performed by *Fukunishi et al.* [1996] using a multichannel high-speed (time resolution of 15  $\mu$ s) photometers at Yucca Ridge Field Station, Colorado in June-August 1995. The photometers were used to simultaneously observe two different elevation angles ( $0.2^\circ$  pointing accuracy) with a narrow field of view of  $1.0^\circ$  in the vertical direction and  $9.5^\circ$  in the horizontal direction. A typical example of transient luminous events observed is shown in Figure 1.9. The location of a positive discharge (08:57:53.306 UT, +326 kA) coincident in time with this event was identified by National Lightning Detection Network (NLDN) to be at a distance of 231 km South-East of Yucca Ridge. The figure shows the luminosity variations measured by the photometer over a 40 ms interval, with one photometer channel (without filter) set at  $15^\circ$  elevation, while the remaining two channels, one without filter and the other with a red filter, set at  $9^\circ$  elevation. The luminosity variations consist of two parts, an initial short duration burst coincident in time with the recorded onset of a VLF sferic and a longer duration event starting  $\sim 7$  ms later. The first burst actually consisted of two parts, with an initial portion interpreted to be due to Rayleigh scattered light from the precursor cloud-to-ground lightning flash. The second portion was observed only in the high elevation photometer and was interpreted to be a large scale lower ionospheric diffuse flash lying between  $\sim 75$  to 90 km altitudes. These brief flashes are called “elves” [*Fukunishi et al.*, 1996] and are believed to be produced by the heating of ambient ionospheric electrons by intense electromagnetic pulses (EMPs) radiated by powerful lightning discharges [*Inan et al.*, 1996b]. The longer duration peak which started  $\sim 7$  ms later corresponds to a sprite event [*Fukunishi et al.*,



1996]. The time delay between the onset of the VLF sferic and the onset of the following sprite is found in the case shown to be 7 ms; however, in different cases observed, this time delay ranged from several to several tens of milliseconds [Fukunishi *et al.*, 1996].

In summary, the most recent photometric measurements demonstrate that sprites are typically delayed in time ranging from  $\sim 3$  ms [Winckler *et al.*, 1996] to several tens of ms [Fukunishi *et al.*, 1996] with respect to the onset of the causative cloud-to-ground stroke. The duration of sprite events as observed in photometer data usually decays on a time scale of one video field, although this result may be specific to the spectral range covered by the photometers used.

### 1.2.8 Spectral Properties of Sprites

Spectra of sprites in the stratosphere/mesosphere above electrically active cumulonimbus clouds were acquired on July 16, 1995 from an observation site near Ft. Collins, Colorado by Mende *et al.* [1995]. The spectra, resolved from  $\sim 450$ -800 nm, included four distinct features in the 600-760 nm region which have been identified as the  $N_2$  first positive system with  $\Delta=2,3$ , and 4 from the  $v=2,4,5,6$  vibrational levels of the  $B^3\Pi_g$  state. The spectra were lacking in other features such as the  $N_2^+$  Meinel or the  $N_2^+$  first negative system which led the authors [Mende *et al.*, 1995] to a conclusion that the electron energy causing the excitation is quite low. However, with the available signal-to-noise ratio of the measurement, in order to be detectable these other features would have had to be at levels no less than a factor of ten of that of the  $N_2$  first positive system. The result obtained by Mende *et al.* [1995] is shown in Figure 1.10.

Hampton *et al.* [1996] used a video slit spectrograph to obtain optical spectra of sprites. Twenty five events were observed from the Mt. Evans Observatory over a thunderstorm on the border of Nebraska and Colorado between 0700 and 0900 UT on the night of 22 June 1995. For 10 of these events optical spectra were measured in the wavelength range from 540 to 840 nm. After correcting for the spectrograph response function, digitized

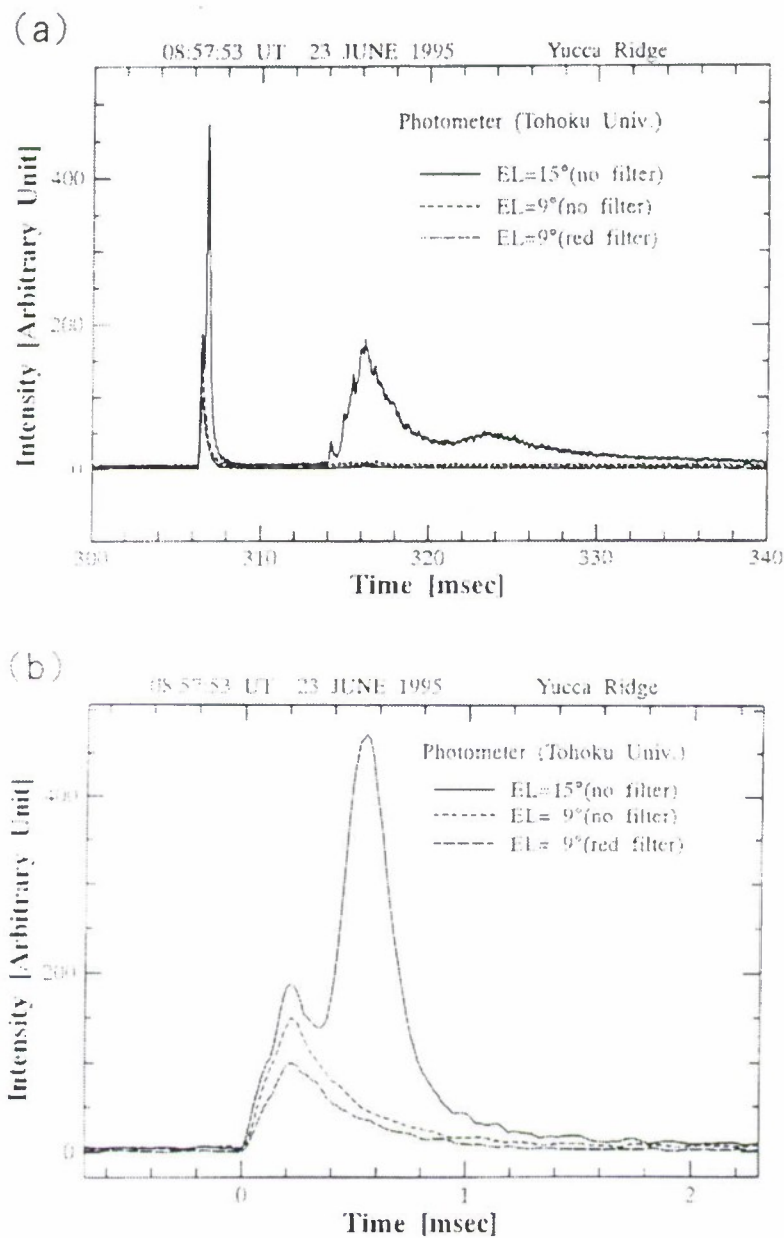


**Fig. 1.9. Lightning-induced transient luminous event** [Fukunishi *et al.*, 1996]. An example of lightning-induced transient luminous events observed at Yucca Ridge Field Station, Colorado: (a) luminosity variations observed by a four-channel photometer during the 40-ms interval between 08h 57m 53.300 sec and 53.340 sec UT on June 23, 1995; (b) enlarged display of photometer signals for the initial 3-ms interval. The figure is reproduced from [Fukunishi *et al.*, 1996].



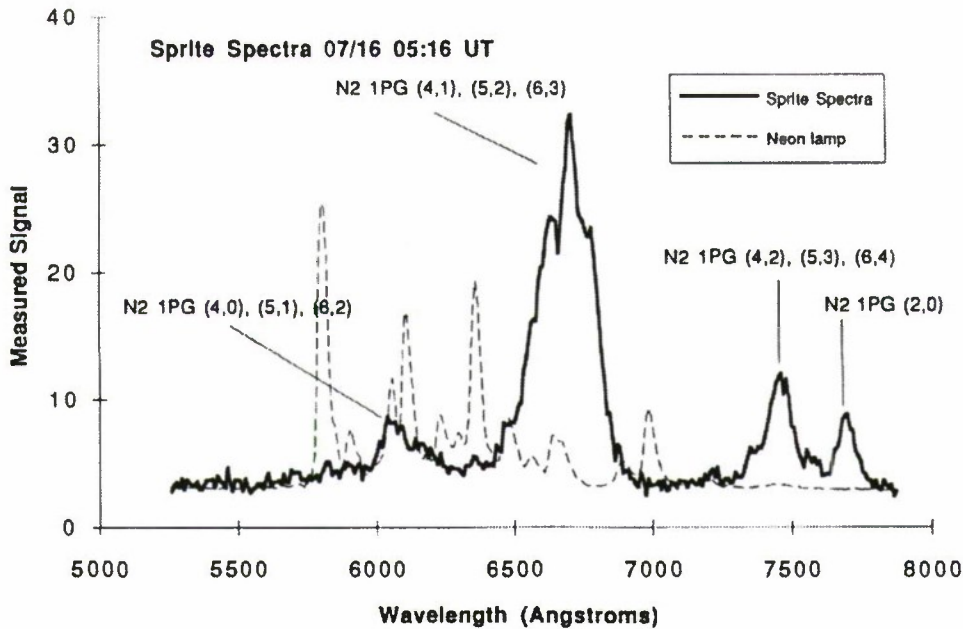


**Fig. 1.10. Spectral scan of a sprite** [Mende *et al.*, 1995]. The thick trace represents the spectra of the sprite while the thin trace shows the spectra of a calibration neon light. The figure is reproduced from [Mende *et al.*, 1995].

spectrograph video images were used to measure the wavelength of, and ratios between, the various emissions. All emissions were found to be those of the first positive bands of  $N_2$ . There was no evidence of the presence Meinel bands of  $N_2^+$ , indicating (in the opinion of the authors) that the mechanism responsible for sprites produces little or no ionization at 70 km altitude. However, it is important to note that, in order to be detectable, the intensity of the Meinel band would have to be no smaller than a factor of  $\sim 10$  below that of the  $N_2$  first positive band. As we show later (Sections 3.5 and 4.7.3), the predicted levels of Meinel band intensities in sprite producing processes which lead to intense ionization columns are  $\sim 10^3$  lower than that of  $N_2$  first positive.

In summary, the red color of sprites was experimentally identified by two independent groups of authors as being primarily due to excitation of the first positive band of molecular nitrogen [Mende *et al.*, 1995; Hampton *et al.*, 1996]. The measurements of both Hampton *et*

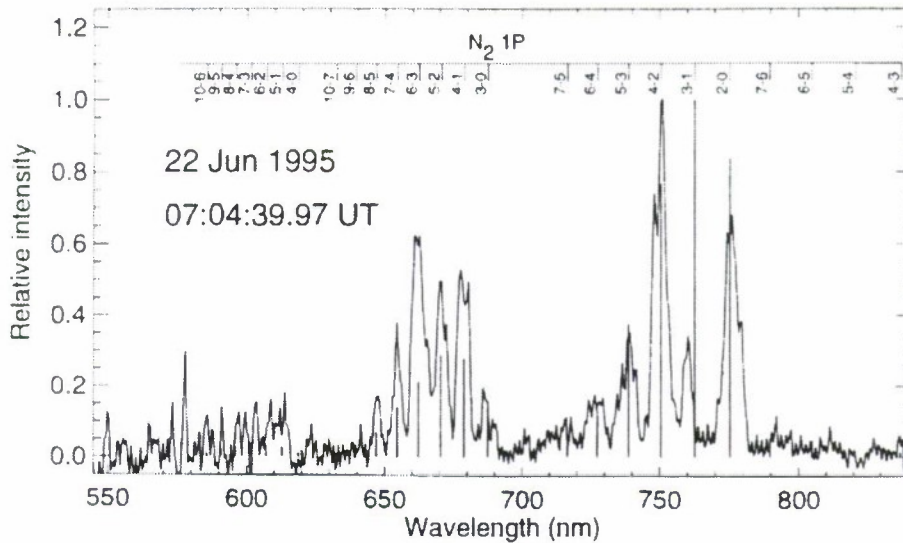


**Fig. 1.11. Reduced spectrum of a sprite** [Hampton *et al.*, 1996]. Reduced spectrum from a sprite event observed at 07:04:39 UT. The wavelengths for the band heads for different transitions of the first positive band of  $N_2$  are marked at top. The vertical lines show the auroral intensities of these transitions. The figure is reproduced from [Hampton *et al.*, 1996].

*al.* [1996] and Mende *et al.* [1995] are fully consistent with the theoretical results put forth in this thesis and are not inconsistent with intense ionization occurring within the luminous regions of sprites. Quantitative interpretation of these results is given in Sections 3.5 and 4.7.3 of this dissertation.

### 1.2.9 Observations of Blue Jets During Summer 1994

During the Sprites 1994 dual aircraft observational campaign conducted by the University of Alaska a completely new and distinctly different (from sprites) optical phenomena called “blue jets” was captured by black and white and color video cameras [Wescott *et al.*, 1995a; Sentman and Wescott, 1994]. Blue jets are narrowly collimated beams of blue light that propagate upwards from the tops of thunderclouds. The jets appear to propagate upward at speeds of about 100 km/s and reach terminal altitudes of 40-50 km. Fifty six examples were recorded during a 22 minute interval during a storm over Arkansas. Two examples of the images recorded are illustrated in Figure 1.12.



**Fig. 1.12.** Two images of Blue Jets obtained from an aircraft during summer 1994 Sprites campaign [Wescott *et al.*, 1995a]. Images are provided through the courtesy of E. Wescott, University of Alaska. Images are taken from <http://www.ghcc.msfc.nasa.gov/skeets.html> [Courtesy of Dr. O. H. Vaughan, Jr.].

Blue jets are narrowly collimated (full cone angle  $\sim 15 \pm 7.5^\circ$ ) with an apparent fan out near their tops (40-50 km). The estimated brightness ranges up to nearly  $10^3$  kR [E. Wescott, personal communication]. Their apparent source duration is  $\sim 200$  ms at the base of the jet. The overall brightness at the bottom is  $\sim 100$  times that at the top of the jet and the luminosity decays simultaneously along the jet beginning at about 200 to 300 ms. A faint hemispherical “shock” is observed beyond the terminus of some jets traveling at the same speed as the earlier rising portion of the jet. The typical lateral dimensions of the jets are few kilometers at the base and  $< 10$  km at the top. Unlike sprites, blue jets may be characterized by a lack of strong electromagnetic emission at VLF and are not observed to be associated with simultaneous cloud-to-ground flashes [Wescott *et al.*, 1995b; 1996].

### 1.3 SCIENTIFIC CONTRIBUTIONS

The purpose of this Ph.D. dissertation research was to theoretically investigate new forms of electrodynamic coupling of energy originating in lightning discharges to the mesosphere and the lower ionosphere. The scientific contributions resulting from this effort are described in Chapters 3, 4 and 5. A summary of the specific contributions to knowledge is presented below:

- Identification of a new type of electrodynamic coupling between tropospheric thunderstorms and the mesosphere and the lower ionosphere based on heating, ionization and optical emission effects produced by quasi-electrostatic thundercloud fields.
- Development of a new two dimensional and selfconsistent model of the nonlinear upward coupling of quasi-electrostatic thundercloud fields.
- Quantitative evaluation of electron heating, ionization of the ambient neutral atmosphere, and the excitation of optical emissions due to intense quasi-electrostatic fields following lightning discharges. Comparison of results with experimental data on mesospheric optical flashes called sprites.
- Investigation of the formation and upward propagation of streamer type ionization channels produced by pre-discharge quasi-electrostatic fields immediately above the thundercloud. Identification of this process as the underlying physical mechanism for the observed upward moving highly collimated beams of blue color emanating from the thundercloud tops and known as blue jets.

Most of the results presented in this dissertation were previously published in [*Pasko et al.*, 1995, 1996a,b].



# 2

## Quasi-Electrostatic Heating Model

In this chapter, we describe our model formulation of the interaction of quasi-electrostatic thundercloud fields with the mesosphere and lower ionosphere.

### 2.1 ELECTRIC FIELD AND CHARGE DENSITY

The quasi-electrostatic field is established in the mesosphere and lower ionosphere due to the accumulation of thundercloud charge and its evolution in time as a portion of the charge is lowered to the ground by a positive cloud-to-ground (+CG) or negative cloud-to-ground (-CG) lightning stroke, or neutralized inside the cloud due to an intracloud (IC) discharge (Figure 2.1). In addition, (see Section 3.8 for more details) we consider the specific cases of the removal or deposition of monopole charges (see cases marked M1 and M2 in the top panel of Figure 2.1).

The quasi-electrostatic fields treated in our model are the slowly varying and long enduring electric component of the total electromagnetic field which is generated by the removal of charge from the cloud. Specifically, we leave out the short duration electromagnetic pulses (EMP) generated primarily by the return stroke currents and which produce bright optical emissions at 80-95 km altitudes emitted in a thin cylindrical (doughnut-like) shell expanding to radial distances up to 150 km [see *Inan et al.*, 1996b, and references cited therein] and referred to as “elves” [*Fukunishi et al.*, 1996]. In terms of calculations of the quasi-static

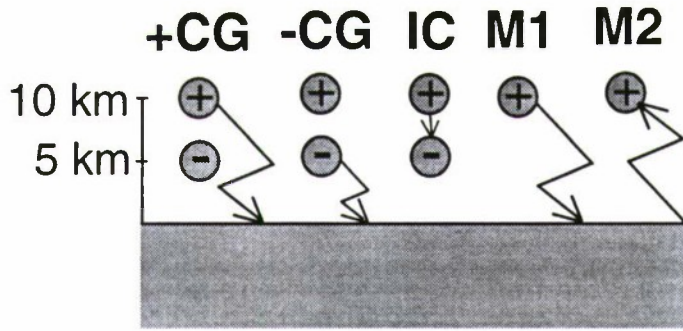


**Fig. 2.1. Thundercloud charge removal models.** Positive (+CG), negative (-CG), intra-cloud (IC), monopole removal (M1) and monopole deposition (M2) models of thundercloud “discharges”.

electric fields this approach appears to be fully sufficient, as was shown by comparing results obtained from the same quasi-static equations used in our model with the results of solutions of a full set of Maxwell equations [Baginski and Hodel, 1994].

Any effects associated with magnetic fields are necessarily left out in our formulation. The effects of the earth’s magnetic field can be neglected in view of the extremely high collision rates that are in effect even under mild heating conditions (Section 3.4). Any magnetic fields generated due to the slow temporal variations of the quasi-static electric fields are too small to have any effect on the electron dynamics. Indeed, simple estimations show that the electric field with amplitude  $\sim 100$  V/m which varies on a characteristic time scale  $\sim 1$  ms and has spatial scale  $\sim 100$  km leads to amplitudes of induced magnetic fields which are at least two orders of magnitude lower than earth’s magnetic field and thus can be ignored.

The thundercloud charges  $+Q$ ,  $-Q$  form a vertical dipole which is assumed to develop over a time  $\tau_f$ . The positive or negative charges, or both are then “discharged” (or removed) by decreasing the magnitude of charge with a time constant  $\tau_s$ , corresponding respectively to +CG, -CG or IC lightning discharges, as illustrated in Figure 2.2. Experimental data on lightning discharges indicates that the charge removal time  $\tau_s$  may vary between  $\sim 1$  ms and several tens of ms [Uman, 1987, pp.124, 196]. In Chapter 3 we concentrate mainly on

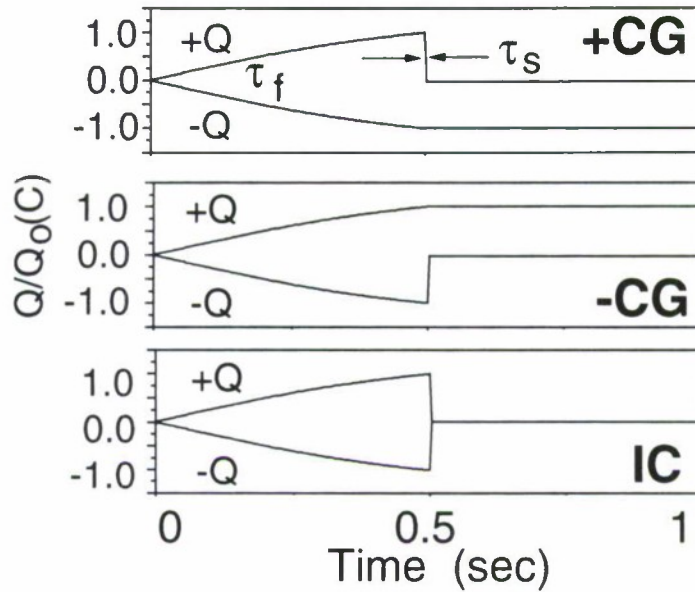


**Fig. 2.2. Thundercloud charge dynamics corresponding to different models.** The assumed behavior of the source charges corresponding to +CG, -CG, and IC models.

CG discharges involving relatively rapid removal of charge, namely cases for which  $\tau_s \sim 1$  ms. Slower discharges are considered in Chapter 4.

A cylindrical coordinate system  $(r, \phi, z)$  is used with the  $z$  axis representing altitude, as illustrated in Figure 2.3. The ground and ionospheric boundaries (taken to be at  $z=90$  km) are assumed to be perfectly conducting and the entire system is taken to be cylindrically symmetric about the  $z$  axis. Two different types of boundary conditions can be utilized at the cylindrical boundary (can be taken, for example, at  $r=60$  km). If we assume a perfect conductor at  $r=60$  km, we have  $\partial\varphi/\partial r = 0$  (or  $\varphi=0$ ), where  $\varphi$  is the electrostatic potential. This condition was used by *Illingworth* [1972] and essentially amounts to considering the solution of the electrostatic fields in a “tin-can”. Alternatively, we can assume that  $\partial\varphi/\partial z=0$ , an assumption adopted by *Tzur and Roble* [1985]. Both of the boundary conditions are rather artificial and lead to unphysical modification of the electric fields near the boundary. However, the temporal and spatial evolution of the electrostatic field system does not depend significantly on these edge fields if the boundaries are chosen to be far enough from the charge sources. The distance  $r=60$  km used in our calculations represents a trade off between

the resolution which is possible with available computer resources and the accuracy of the electric field calculation. As an example, the presence of the conducting boundary at  $r=60$  km leads to an error of less than  $\sim 10\%$  on the magnitude of the electric field at  $r=50$  km and  $z=10$  km.

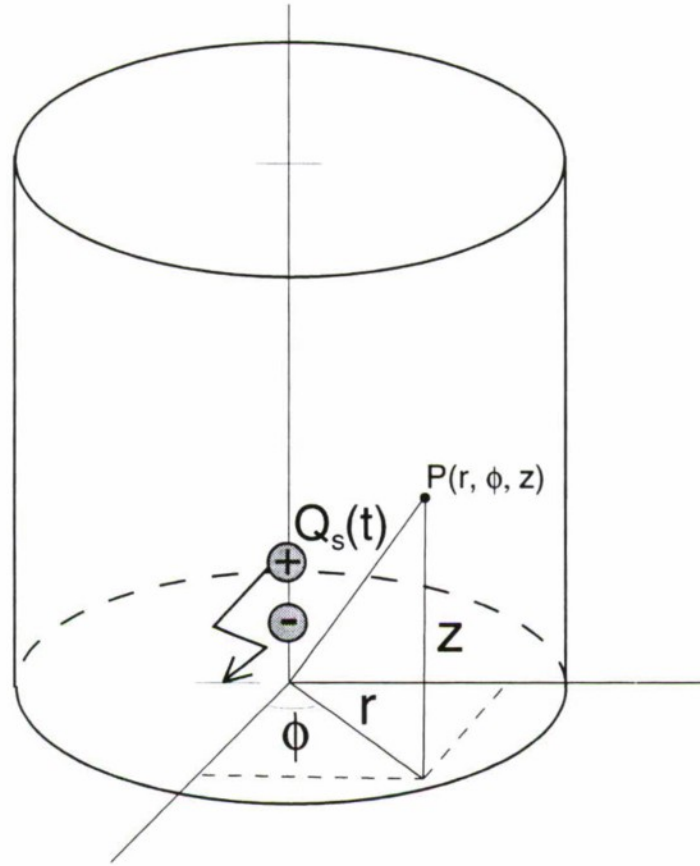


Fig. 2.3. Coordinate system used in calculations.

The electrostatic field  $\vec{E}$ , given by  $\vec{E} = -\nabla\varphi$ , the charge density  $\rho$ , and the conduction current  $\vec{J} = \sigma\vec{E}$  are calculated using the following system of equations:

$$\frac{\partial(\rho + \rho_s)}{\partial t} + \nabla \cdot (\vec{J} + \vec{J}_s) = 0 \quad (2.1)$$

$$\nabla \cdot \vec{E} = (\rho + \rho_s)/\epsilon_0 \quad (2.2)$$



where  $\rho_s$  and  $\vec{J}_s$  are the thundercloud source charge and current which satisfy the equation  $\partial\rho_s/\partial t = -\nabla \cdot \vec{J}'_s$ , where  $\nabla \cdot \vec{J}'_s = \nabla \cdot \vec{J}_s + \rho_s\sigma/\epsilon_o$ , where the effective source current  $\vec{J}'_s$  is introduced so as to compensate any change in the thundercloud charge  $\rho_s$  due to the conduction current. Equation (2.1) can then be written in the form:

$$\frac{\partial\rho}{\partial t} + \nabla\sigma \cdot \vec{E} + \rho\sigma/\epsilon_o = 0 \quad (2.3)$$

If in (2.3) one simply assumes  $\partial\rho_s/\partial t = -\nabla \cdot \vec{J}_s$ , (i.e.,  $\vec{J}_s = \vec{J}'_s$ ), it is necessary that  $\rho\sigma/\epsilon_o$  be substituted with  $(\rho + \rho_s)\sigma/\epsilon_o$ . In this case, if one ignores the effects of the conductivity gradients, the quasi-stationary solution of equation (2.3) is simply  $\rho = -\rho_s$ , so that the source charge is completely compensated by charge induced in the conducting medium over a time scale  $\sim\epsilon_o/\sigma$ . Strictly speaking,  $\rho_s$  is a function of time [i.e.,  $\rho_s = \rho_s(t)$ ] so that the quasi-stationary solution  $\rho = \rho_s$  has physical meaning only in the case when the characteristic time scale of  $\rho_s(t)$  is much longer than  $\epsilon_o/\sigma$ . As can be seen from (2.1) and (2.2), the introduction of  $\vec{J}'_s$  allows us to specify the charge dynamics inside the cloud as an externally determined function of time.

Physically, the current  $\vec{J}'_s$  as a source of  $\rho_s$  is associated with the process of separation of charges inside the cloud and is directed opposite to the resulting electric field [Wilson, 1956]. The current  $\vec{J}'_s$  may be related to the small and light positively charged ice splinters, which are driven upward by a strong stream of convecting air, and heavy negatively charged hail particles which are driven downward by gravity [Malan, 1963, p. 76; Uman, 1987, p. 65]. We note that the model of thundercloud charges used in this dissertation is rather simplified in comparison with the actual vertical distribution of charge density in mesoscale convective systems (MCS) producing sprites, which may sometimes have up to six layers of charge with complicated spatial structure [e.g., Marshall and Rust, 1993; Rust et al., 1996]. However, as we show later, physical results of our model depend mostly on the magnitude and altitude of the charge removed by the cloud-to-ground lightning discharge and are essentially independent of the details of the initial configuration of charges with different polarities in the thundercloud.



We assume that  $\rho_s = \rho_+ + \rho_-$  and that the separated dipole charges (i.e.,  $+Q$  or  $-Q$ ) are represented as distributed charge densities  $\rho_+(\vec{r}, t)$  or  $\rho_-(\vec{r}, t)$  having a Gaussian spatial distribution given by  $\rho_{\pm}(\vec{r}, t) = \rho_o e^{-[(z-z_{\pm})^2 + r^2]/a^2}$  with  $a=3$  km,  $z_-=5$  km,  $z_+=10$  km, so that the total source charges are  $\pm Q(t) = \int \rho_{\pm}(\vec{r}, t) dV$ . Our formulation can also be used to consider of horizontally extended charge distributions similar to those existing in mesoscale convective systems [E. Williams, private communication; Boccippio *et al.*, 1995; Marshall *et al.*, 1996]. In such a case, the charge density corresponding to the thundercloud charges would have a Gaussian distribution in the  $z$  direction while being uniform in the  $r$  direction, with its scale determined by the radius of the “disk” of charge. This disk charge density is normalized accordingly so that we still have  $\pm Q(t) = \int \rho_{\pm}(\vec{r}, t) dV$ .

Equation (2.3) is integrated in time using an explicit two step method of solution of ordinary differential equations [Potter, 1973, p. 34]. At each time step the electric field  $\vec{E}$  to be used in (2.3) is found by integration of equation (2.2) via the method of cyclic reduction [Buneman, 1969] using a FORTRAN routine published by Swarztrauber and Sweet [1975]. The conductivity  $\sigma$  in (2.3) is calculated self-consistently by taking into account the effect of the electric field on the electron component through changes in mobility (due to heating) and electron density (due to attachment and/or ionization). A fourth order Runge-Kutta method and different conservative and nonconservative numerical schemes are also employed to test the accuracy of results obtained.

## 2.2 LIGHTNING CURRENT AND CHARGE

The important input parameters that need to be specified externally for each model calculation are: (1) the altitude profiles of ambient ion conductivity and electron density; (2) the magnitude ( $Q_o$ ) of the charge transferred (e.g., by a CG lightning discharge) and the time constant ( $\tau_s$ ) which determines the rate at which the charge is transferred; and (3) the altitude of the charge removed. None of these parameters are directly available in a typical experimental context, except for the fact that the National Lightning Detection Network

(NLDN) records lightning intensity (or peak current  $I_p$  [e.g., *Idone et al.*, 1993]) does imply some restrictions on the magnitude of the removed charge  $Q$  and the time scale of the charge removal  $\tau_s$ .

In the context of the quasi-electrostatic heating model, the thundercloud charging and discharging process is assumed to consist of two stages. During the predischage stage with duration  $\tau_f$ , charge  $Q_o$  slowly (hundreds of seconds) accumulates in the thundercloud. The second stage is the lightning discharge, during which the thundercloud charge is quickly and completely removed from the thundercloud over a time  $\tau_s$ , usually of the order of several ms. Mathematically, the continuous thundercloud charge dynamics can be represented in the form:

$$Q(t) = Q_o \frac{\tanh(t/\tau_f)}{\tanh(1)}, \quad 0 < t < \tau_f$$

$$Q(t) = Q_o \left[ 1 - \frac{\tanh(t/\tau_s)}{\tanh(1)} \right], \quad \tau_f < t < \tau_f + \tau_s$$

$$Q(t) = 0, \quad \tau_f + \tau_s < t$$

Note that the choice of the functional variation as  $\tanh(\cdot)$  is rather arbitrary but is not critical for the physics of the phenomena modeled. In addition, in Chapter 4, we will consider a more complicated charge removal scenario as illustrated in Figure 4.1e.

For this particular assumed functional dependence of  $Q(t)$  the amplitude of the peak current at  $t = \tau_f$  can be calculated as

$$I_p = \frac{dQ}{dt} = \frac{Q_o}{\tau \tanh(1)}, \quad t = \tau_f$$

Having calculated  $I_p$ , the value of the peak electric field at a distance of 100 km from the lightning discharge can be found as [*Orville*, 1991]

$$E_{100} = \frac{I_p v}{2\pi D \epsilon_o c^2}$$

where  $c$  is speed of light in free space,  $\epsilon_o$  is dielectric permittivity of free space,  $D = 10^5$  m, and  $v = 1.5 \times 10^8$  m/s.

For example,  $E_{100}=75$  V/m corresponds in this model to a peak current of  $I_p=270$  kA and a total charge removed in lightning of  $Q_o=200$  C, if we assume  $\tau_s=1$  ms, a reasonable value based on experimental data [Uman, 1987, pp. 124, 199]. We note that the duration of the lightning discharge  $\tau_s$  as well as the functional time dependence of the charge removal  $Q(t)$  as given above are not available from measurements provided by NLDN. Nevertheless, these parameters constitute critically important inputs for modeling the corresponding heating and ionization changes in the lower ionosphere.

Another important input to the model is the ambient ion conductivity profile, which determines the relaxation time for the quasi-electrostatic field and thus the amount and duration of heating for given values of  $Q_o$  and  $\tau_s$ . Detailed description of the conductivity model is given in the following sections.

### 2.3 AMBIENT CONDITIONS IN THE ATMOSPHERE AND LOWER IONOSPHERE

For the various model calculations in this thesis, we consider three different models of ambient electron number density (Figure 2.4a). These models of electron density were used in previous studies of subionospheric VLF propagation in the presence of localized ionospheric disturbances caused by lightning induced electron precipitation [e.g., Pasko and Inan, 1994]. They were employed in this dissertation to represent a wide range of possible variability of the electron density in the nighttime lower ionosphere.

For the ambient ion conductivity, we consider three different altitude profiles as illustrated in Figure 2.4b. For illustrative purposes the ambient conductivity profiles in Figure 2.4b also include the electron component  $\sigma_e$  which is given by

$$\sigma_e = q_e N_e \mu_e \quad (2.4)$$

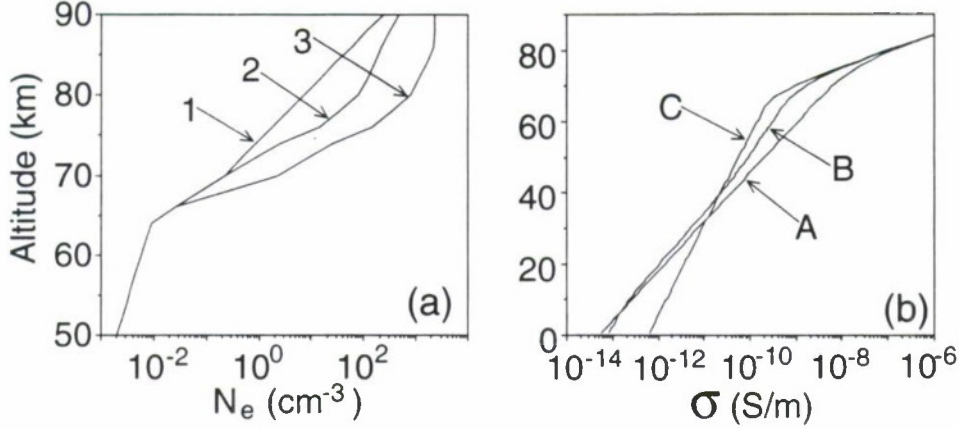


**Fig. 2.4. Ambient electron density and ion conductivity.** Three altitude profiles of ambient electron number density (a), and ion conductivity (b) used in the various calculations reported in this thesis.

where  $q_e$  is the electronic charge,  $N_e$  is the number density of electrons, and  $\mu_e$  is the electron mobility and which is typically dominant at altitudes above  $\sim 60$  km. The total conductivity profiles shown in Figure 2.4b were calculated with the electron component (dominant at  $>60$  km altitude) determined by the electron density profile 1 shown in Figure 2.4a, and electron mobility for essentially cold electrons of  $\mu_e = 1.36N_o/N \text{ m}^2/\text{V/s}$ , where  $N_o = 2.688 \times 10^{25} \text{ m}^{-3}$ , and  $N$  is number density of air molecules (see Section 2.4.1 for further details).

At altitudes  $<60$  km, the total conductivity is dominated by the ion conductivity. Profile A ( $\sigma_A = 5 \times 10^{-14} e^{z/6\text{km}} \text{ S/m}$ ) is taken from [Dejnakarintra and Park, 1974], while Profile C ( $\sigma_C = 6 \times 10^{-13} e^{z/11\text{km}} \text{ S/m}$ ) is derived from experimental measurements of Holzworth *et al.* [1985]. The intermediate profile B is calculated on the basis of the known mobility of ions  $\mu_i$  as a function of altitude ( $\mu_i \sim 2.3N_o/N \text{ m}^2/\text{V/s}$ ) [Davies, 1983]) and assuming the number density of ions to be  $\sim 10^3 \text{ cm}^{-3}$  [Reid *et al.*, 1979]. We note that A, B and C are used to mark ambient ion conductivity profiles. In further calculations we will use different combinations of ions conductivity profiles (A, B, or C) and electron conductivities defined by the electron density profiles (1, 2, or 3, as shown in Figure 2.4a).

We neglect the effects of the magnetic field of the earth on the conductivity since, for the range of parameters considered, the ionospheric plasma is highly collision dominated (see Section 3.4 for detailed justification of this assumption).



## 2.4 SELFCONSISTENT EVALUATION OF CONDUCTIVITY

In a weakly ionized collisional medium such as the lower ionosphere and the mesosphere, both the electron mobility and the electron density depend nonlinearly on the electric field. The heating of the ambient electrons by the intense fields leads to substantial modification of the atmospheric conductivity at altitudes  $>60$  km. The modified conductivity in turn determines the penetration and relaxation of the electric field, so that it is necessary to self consistently determine the evolution of the conductivity as we solve for the evolution of the quasi-static field and the associated consequences (e.g., optical emissions). This self consistent solution is one aspect of our work that was left out in earlier formulations of penetration of thundercloud fields to the ionosphere [e.g., *Dejnakarintra and Park, 1974; Baginski et al., 1988*], in which the conductivity was simply assumed to remain equal to the assumed ambient profiles. Note that the heating of electrons only modifies conductivity at  $>\sim 60$  km altitudes where the electron component of the conductivity is dominant. At altitudes below 60 km, where ions are dominant, the conductivity remains equal to the ambient levels, since the ions are not significantly heated by the electric field.

### 2.4.1 Electron Mobility

The electron mobility  $\mu_e$  is a complicated function of the electric field as determined by the various loss processes each having different cross sections [see *Taranenko et al., 1993a,b* and references therein]. In this dissertation, we adopt a functional dependence of  $\mu_e$  on the magnitude of the electric field  $E$  which is derived from experimental data [*Davies, 1983; Hegerberg and Reid, 1980*]. This function is shown in Figure 2.5 and can be expressed in the following analytical form:

$$\log(\mu_e N) = \sum_{i=0}^2 a_i x^i, \quad EN_o/N \geq 1.62 \times 10^3 \text{ V/m} \quad (2.5)$$

$$\mu_e N = 1.36N_o, \quad EN_o/N < 1.62 \times 10^3 \text{ V/m}$$



where  $x = \log(E/N)$ ,  $a_0 = 50.970$ ,  $a_1 = 3.0260$ , and  $a_2 = 8.4733 \times 10^{-2}$ . The analytical expression (2.5) can be used for computationally efficient calculation of the electron mobility for any combination of electric field and number density of air molecules (i.e., altitude). This analytical method provides results which compare well with those obtained from fully kinetic formulations, as discussed in further detail in Appendix A.

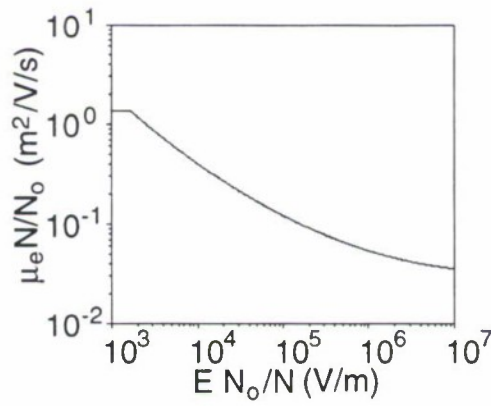


**Fig. 2.5. Electron mobility.** The electron mobility  $\mu_e$  is shown as a function of the electric field  $E$  and the molecular number density  $N$  of atmospheric gas.

Another parameter which is often useful in specifying the degree of electron heating is the effective frequency of electron collisions with ambient neutral gas. This parameter, denoted  $\nu_{\text{eff}}$ , is given as a simple function of the electron mobility  $\mu_e$  as  $\nu_{\text{eff}} = q_e / (\mu_e m_e)$ .

### 2.4.2 Ionization Coefficient

In addition to the nonlinear dependence of  $\mu_e$  on  $E$ , the local value of the electron density  $N_e$  depends highly nonlinearly on the electric field due to impact ionization and dissociative attachment processes. These processes begin to become significant as the electric field exceeds a certain threshold and eventually lead to “dielectric breakdown” of the atmospheric gas.

For quantitative description of atmospheric and ionospheric air breakdown we use the ionization coefficient  $\nu_i$  given in [Papadopoulos *et al.*, 1993], derived from recent results of computer simulations and experimental measurements, which for our quasi-static case ( $\omega \rightarrow 0$ , where  $\omega$  is the angular frequency with which the electric field is assumed to vary) is illustrated in Figure 2.6 and which can be expressed in the following analytical form [Papadopoulos *et al.*, 1993]:

$$\nu_i = 7.6 \times 10^{-13} N x^2 f(x) e^{-4.7(1/x-1)}, \quad (2.6)$$

where

$$f(x) = \frac{1 + 6.3e^{-2.6/x}}{1.5}$$

$x = E/E_k$ , and  $E_k = 3.2 \times 10^6 N/N_o$  V/m is the characteristic air breakdown field shown for reference in Figure 2.6 by a dashed line.

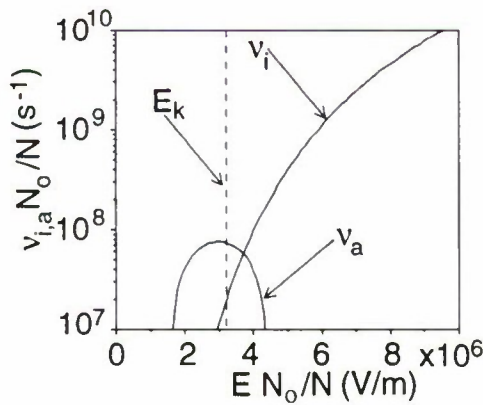


**Fig. 2.6. Ionization and dissociative attachment.** The ionization  $\nu_i$  and dissociative attachment  $\nu_a$  coefficients are shown as a function of the electric field  $E$  and the molecular number density  $N$  of the atmospheric gas.

It should be noted that due to the relatively slow variation of the electric field the conductivity in our model is assumed to be independent of frequency. Similarly, the ionization

coefficient, although originally derived for radio frequency (RF) fields of certain definable frequency  $\omega$  [Papadopoulos *et al.*, 1993], is used in this dissertation to be in DC limit ( $\omega \rightarrow 0$ ). Both assumptions are well justified since for quasi-static electric fields  $\omega < \sim 10^3$  rad/s and always remains much less than  $\nu_{\text{eff}}$  and frequencies in RF range [Papadopoulos *et al.*, 1993].

### 2.4.3 Attachment Coefficient

In our quasi-electrostatic heating formulation, we can include the two-body attachment of electrons to  $\text{O}_2$  molecules with dissociation ( $e^- + \text{O}_2 \rightarrow \text{O} + \text{O}^-$ ). The effective coefficient  $\nu_a$  of this reaction is shown in Figure 2.6 and is a function of electric field which is derived from experimental data [Davies, 1983]. This quantity can be expressed in the following analytical form:

$$\nu_a = \frac{N}{N_o} \sum_{i=0}^2 a_i x^i \quad (2.7)$$

where  $x = EN_o/N$ ,  $a_0 = -2.41 \times 10^8$ ,  $a_1 = 211.92$ , and  $a_2 = -3.545 \times 10^{-5}$ . The attachment coefficient  $\nu_a$  given in (2.7) is an effective coefficient which is a function of the true attachment coefficient (for  $\text{O}^-$  formation), the charge transfer coefficient, and the detachment coefficient [Davies, 1983].

At very low values of  $\nu_i$  and  $\nu_a$  (in the region of electric fields  $E < E_k$ ) the value of the attachment coefficient  $\nu_a$  as given by (2.7) becomes smaller than the ionization coefficient  $\nu_i$  as given by (2.6) and leads to unphysical results. For such low values of  $\nu_a N_o/N$ , which correspond to  $EN_o/N < 1.628 \times 10^6$  V/m, the value of the attachment coefficient can be found from kinetic calculations [Taranenko *et al.*, 1993b] as:

$$\log\left(\frac{\nu_a N_o}{N}\right) = \sum_{i=0}^3 a_i x^i \quad (2.8)$$

where  $x = \log(EN_o/N)$ , and the series of coefficients  $a_0 = -1073.8$ ,  $a_1 = 465.99$ ,  $a_2 = -66.867$ , and  $a_3 = 3.1970$ .

In previous work on swarm experiments [Davies, 1983] it was recognized that the role of dissociative attachment of electrons to O<sub>2</sub> (the fastest process of loss of electrons under heated conditions which may lead to significant modifications of the lower ionosphere [Taratenko *et al.*, 1993a; Inan *et al.*, 1996b]) is difficult to assess since the measured rates for associative detachment and for collisional detachment are known only within one to three orders of magnitude, respectively. A detailed discussion of the importance of the detachment processes in the analysis of swarm experiments is given in [Wen and Wetzer, 1988].

#### 2.4.4 Electron Density

The ionization  $\nu_i$  (2.6) and attachment  $\nu_a$  (2.7), (2.8) coefficients are used to calculate the temporal dynamics of the electron density using following equation:

$$\frac{dN_e}{dt} = (\nu_i - \nu_a)N_e - \alpha N_e^2 \quad (2.9)$$

where  $\alpha$  is an effective recombination coefficient which in most of calculations in this dissertation is assumed to be zero.

As will be discussed further in Chapters 4 and 5, both sprites and jets can be closely associated with streamer type plasma processes, which can be briefly described as a special category of nonlinear space charge waves [e.g., Vitello *et al.*, 1994]. To represent streamers with our model which is essentially based on one fluid system of equations (2.1) and (2.2) we rely upon different assumptions derived from the results of two-fluid simulations of streamer processes [e.g., Vitello *et al.*, 1994]. These assumptions most concern the proper treatment of the steep boundary at the streamer head, and are implemented in our model as different types of limitations on the growth of the electron density due to breakdown ionization. One of these limitations is implemented through the effective recombination coefficient  $\alpha$  in (2.9) which in this context has straightforward physical meaning. The recombination effect is used for the modeling of the downward propagation of channels of the breakdown



ionization to altitudes  $< 50$  km as discussed in Chapter 4. Estimates indicate that at higher altitudes three body attachment processes as well as the bulk of other chemical reactions in the lower ionospheric D-region (including different recombination processes) have time scales  $> 1$  sec [e.g., *Glukhov et al.*, 1992; *Pasko and Inan*, 1994] and can be neglected on the millisecond time scales of interest in this dissertation. Another limitation which is used for modeling of blue jets simply assumes the constancy of the dielectric relaxation time behind the streamer front. This assumption will be additionally discussed in Chapter 5.

In summary, in equation (2.1) the conductivity  $\sigma$  is calculated as a sum of the ambient ion component  $\sigma_i$  which remains constant in time and the electron component  $\sigma_e$  (2.4) which is calculated self-consistently by taking into account the effects of the electric field through changes in mobility  $\mu_e$  (2.5) due to heating, and changes in the number density of electrons  $N_e$  (2.9) due to ionization and attachment processes.

## 2.5 OPTICAL EMISSIONS

Once the temporal and spatial evolution of the electric field is determined via the selfconsistent solution of (2.1) and (2.2), the intensities of the various optical emissions are determined on the basis of kinetic solutions for the electron distribution function and the excitation coefficients of particular bands. We consider optical emissions from the 1st ( $B^3\Pi_g \rightarrow A^3\Sigma_u$ ) and 2nd ( $C_3\Pi_u \rightarrow B^3\Pi_g$ ) positive bands of  $N_2$ , the Meinel ( $A^2\Pi \rightarrow X^2\Sigma_g^+$ ) and 1st negative bands of  $N_2^+$  ( $B^2\Sigma_u^+ \rightarrow X^2\Sigma_g^+$ ), and the 1st negative band of  $O_2^+$  ( $b^4\Sigma_g^- \rightarrow a^4\Pi_u$ ) which have short lifetimes and are expected to produce the most intense optical output during impulsive heating of the lower ionospheric electrons [*Taranenko et al.*, 1993a,b].

Analysis of the excitation coefficients  $\nu_k$  corresponding to these bands obtained from kinetic calculations [*Taranenko et al.*, 1993a,b] for a series of electric field values and air densities shows that relatively simple and accurate analytical approximations similar to those developed for the electron mobility (2.5), ionization (2.6) and attachment (2.7), (2.8) coefficients can be derived (see Appendix A.1 ). The results are shown in Figure 2.7 and



TABLE 2.1. Approximation Coefficients.

Band	$a_0$	$a_1$	$a_2$	$a_3$
1st pos. $N_2$	-1301.0	563.03	-80.715	3.8647
2nd pos. $N_2$	-1877.1	814.70	-117.46	5.6554
1st neg. $N_2^+$	-1760.0	724.7	-99.549	4.5862
1st neg. $O_2^+$	-1802.4	750.91	-104.28	4.8508
Meinel $N_2^+$	-2061.1	870.25	-122.43	5.7668

for the optical bands considered can be expressed in a general form:

$$\log\left(\frac{\nu_k N_o}{N}\right) = \sum_{i=0}^3 a_i x^i \quad (2.10)$$

where  $x = \log(EN_o/N)$ , and the series of coefficients  $a_0, a_1, a_2, a_3$  corresponding to the different optical bands are given in Table 2.1.

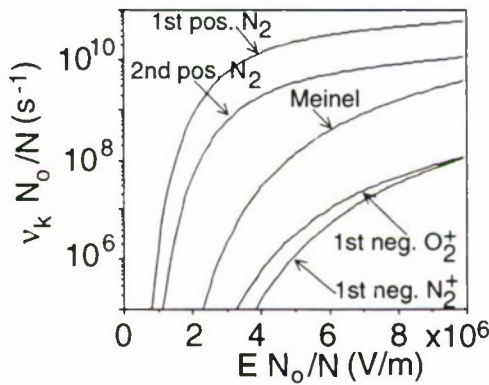


**Fig. 2.7. Optical excitation coefficients.** The excitation coefficients  $\nu_k$  of different optical bands are shown as a function of electric field  $E$  and molecular number density  $N$  of atmospheric gas.

The intensity of each optical line in Rayleighs is given by the expression [Chamberlain, 1978, p. 213]:

$$I_k = 10^{-6} \int_L A_k n_k dl, \quad (2.11)$$

where  $n_k$  is the number density of excited particles in state  $k$ ,  $A_k$  is the radiation transition rate, and the integral is taken along  $L$ , representing the horizontal line of sight. In our calculations, we do not take into account the effects of radiative transfer between the altitude of the emission and the ground which might be important for the interpretation of the total intensity of optical emissions and their fine spectral features (i.e., the strong attenuation of the (3,1) component of the first positive band of  $N_2$  due to the absorption by  $O_2$  at 762 nm over slant paths [Mende *et al.*, 1995; Hampton *et al.*, 1996]). The quantity  $n_k$  is governed by the relation [Sipler and Biondi, 1972]:

$$\frac{\partial n_k}{\partial t} = -\frac{n_k}{\tau_k} + \sum_m n_m A_m + \nu_k N_e \quad (2.12)$$

where  $\tau_k = [A_k + \alpha_1 N_{N_2} + \alpha_2 N_{O_2}]^{-1}$  is the total lifetime of state  $k$ ,  $\alpha_1$  and  $\alpha_2$  are the quenching rates due to collisions with  $N_2$  and  $O_2$  molecules, respectively,  $N_{N_2}$  and  $N_{O_2}$  are the number densities of  $N_2$  and  $O_2$  molecules respectively, and the sum over the terms  $n_m A_m$  represents increases in  $n_k$  resulting from cascading from higher energy states.

The intensity of the optical bands in equation (2.11) is obtained from the number of excited molecules in the upper state  $n_k$  which is given by equation (2.12). In equation (2.12) the electron number density  $N_e$  and the excitation coefficients  $\nu_k$  are the variables which evolve in time and give rise to the optical emissions, and are calculated as functions of the electric field using equations (2.9) and (2.10), as previously described.

The optical emissions from the 1st and 2nd positive bands of  $N_2$ , the Meinel and 1st negative bands of  $N_2^+$ , and the 1st negative band of  $O_2^+$  have the transition rates  $1.7 \times 10^5/s$ ,  $2 \times 10^7/s$ ,  $7 \times 10^4/s$ ,  $1.4 \times 10^7/s$ , and  $8.5 \times 10^5/s$  respectively [Valence-Jones, 1974, p. 119]. Quenching of the 1st positive band emissions occurs primarily through collisions with  $N_2$

molecules, with  $\alpha_1=10^{-11}$  cm<sup>3</sup>/s [Valence-Jones, 1974, p. 119]. Quenching of the 2nd positive band occurs primarily through collisions with O<sub>2</sub> molecules with  $\alpha_2=3 \times 10^{-10}$  cm<sup>3</sup>/s [Valence-Jones, 1974, p. 119]. For the quenching of the Meinel and 1st negative bands of N<sub>2</sub><sup>+</sup> we have  $\alpha_1 = 5 \times 10^{-10}$  cm<sup>3</sup>/s and  $\alpha_1 = 4 \times 10^{-10}$  cm<sup>3</sup>/s respectively, and for the 1st negative band of O<sub>2</sub><sup>+</sup> we have  $\alpha_1 = 2 \times 10^{-10}$  cm<sup>3</sup>/s [Valence-Jones, 1974, p. 119].

## 2.6 LIMITATIONS OF ANALYTICAL MODELS

The simple expressions for mobility (2.5), ionization (2.6), attachment (2.7), (2.8), and optical excitation (2.10) coefficients are supported by experimental measurements as well as by results of kinetic simulations (see Appendix A.1 for details). These analytical expressions are useful from a computational point of view since they provide fast and reasonably accurate solutions for a wide range of input parameters. However, these models are only valid only for  $EN_o/N < 1.6 \times 10^7$  V/m since for fields above this value the mean electron energy approaches the ionization energy and the ionization process becomes nonstationary (see Papadopoulos *et al.* [1993] and references cited therein). The criteria  $EN_o/N < 1.6 \times 10^7$  V/m is equivalent to the condition  $E/E_k < 5$  given by Papadopoulos *et al.* [1993]. At 70 km altitude, this criteria requires that  $E < 1200$  V/m, a condition comfortably satisfied for all the cases considered in this work. In addition, the above expressions cannot be used on time scales less than  $\sim 10$   $\mu$ s (this estimate is valid for altitudes  $\sim 80$ -90 km) which is the time required for the establishment of the stationary electron distribution function [Taranenko *et al.*, 1993a].

# 3

## Heating, Ionization and Optical Flashes in the Mesosphere

In this chapter, we present results obtained using the quasi-electrostatic heating model described in the previous chapter for a variety of ambient atmospheric/lower ionospheric conditions.

### 3.1 PHYSICAL MECHANISM

The basic mechanism of the penetration of the thundercloud electric fields to the higher altitude regions is illustrated in Figure 3.1. As the thundercloud charges slowly build up before a lightning discharge, high altitude regions are shielded from the quasi-electrostatic fields of the thundercloud charges by space charge induced in the conducting atmosphere at lower altitudes. The appearance of this shielding charge is a consequence of the finite vertical conductivity gradient of the atmosphere above the thundercloud. When one of the thundercloud charges (e.g., the positive one as shown in Figure 3.1) is quickly removed by a lightning discharge, the remaining charges of opposite sign in and above the thundercloud produce a large quasi-electrostatic field that appears at all altitudes above the thundercloud, and endures for a time equal to approximately (see discussion in Section 3.10) the local relaxation time ( $\tau_r = \epsilon_0/\sigma$ ) at each altitude. This large electric field can be thought of as being the difference between the electrostatic field dictated (via Coulomb's law) by the



dipole configuration of thundercloud charges and the polarization charge which are in effect before the discharge, and that required by the combination of the single thundercloud charge remaining after the discharge and the polarization charge. These temporarily existing electric fields lead to the heating of ambient electrons and the generation of ionization changes and optical emissions.

In cases of more complex charge distributions in the thundercloud which sometimes involve up to six charge layers in the vertical direction [e.g., *Marshall and Rust*, 1993], each of the charge centers can be viewed as generating its own polarization charge in and above thundercloud, and the resultant configuration of the electric field and charge density can be obtained by using principle of superposition. This consideration is helpful in visualization of the fact that the electric field appearing at mesospheric altitudes after the charge removal by cloud-to-ground lightning discharge is defined mostly by the absolute value and altitude of the removed charge and is essentially independent of the complexity of the charge configuration in the cloud. The charge removal can also be viewed as the “placement” of an identical charge of opposite sign. The initial field above the cloud is simply the free space field due to the “newly placed” charge and its image in the ground which is assumed to be perfectly conducting. This effect will be further illustrated in the context of the results of our calculations (Section 3.8).

### 3.2 MODEL PARAMETERS

In most of the calculations in this chapter we assume the lightning discharge duration to be  $\sim 1$  ms. We evaluate the electron density changes due to the dissociative attachment of electrons to  $O_2$  and the impact ionization of  $O_2$  and  $N_2$ , as well as the dynamics and the two-dimensional distribution of the optical emission intensity of the 1st and 2nd positive bands of  $N_2$ , Meinel and 1st negative bands of  $N_2^+$ , and the 1st negative band of  $O_2^+$ , caused by quasi-electrostatic heating and ionization in the lower ionosphere. We examine the dependence of the heating and ionization upon the altitude profile of ion conductivity and the number



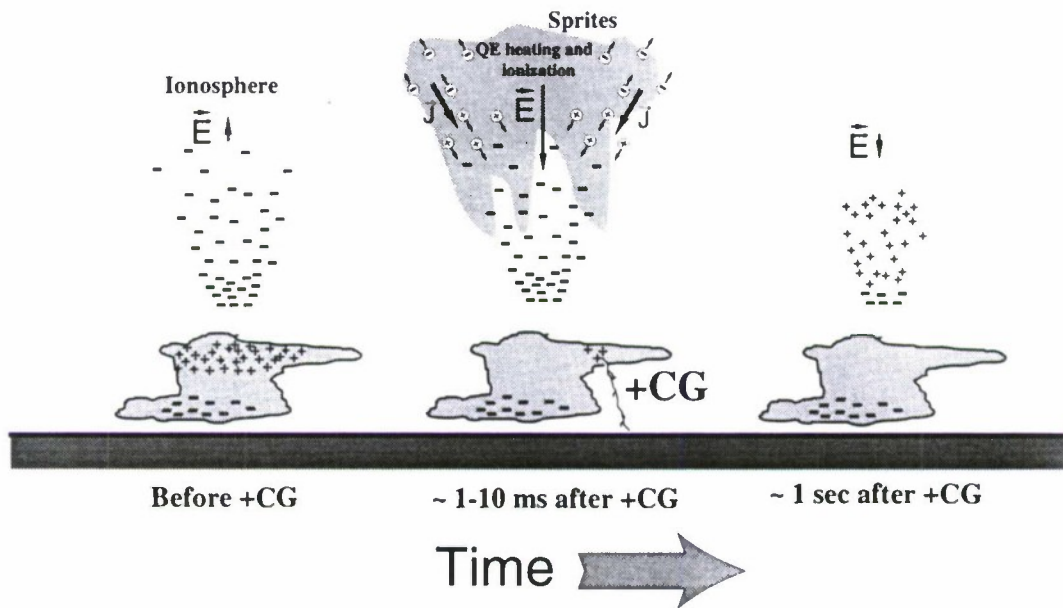


**Fig. 3.1. Physical mechanism of mesospheric optical flashes.** Illustration of the mechanism of penetration of large quasi-electrostatic thundercloud fields to mesospheric altitudes, leading to electron heating, breakdown ionization and excitation of optical emissions.

density of electrons. Some effects associated with the duration of the lightning discharge are also discussed, although further discussion of this subject is provided in Chapter 4. We also discuss the dependence of the quasi-electrostatic heating on the lightning discharge type (i.e., intracloud versus positive or negative cloud-to-ground) as well as on the thundercloud charge geometry. Finally, we analyze the relaxation properties of the electric field in the conducting medium.

In all of the calculations leading to the results presented below in Sections 3.3, 3.4 and 3.5, we use the ambient electron density profile 1 (Figure 2.4a), the ambient ion conductivity profile A (Figure 2.4b), and a lightning discharge duration of  $\tau_s = 1$  ms. In these sections we consider the +CG type of lightning discharge (see Figures 2.1, 2.2). In Sections 3.3, 3.4 and 3.5, the distribution of thundercloud charges is assumed to be spherically symmetric and Gaussian with a spatial scale  $a = 3$  km. The effects produced for different values of above mentioned parameters are investigated in Sections 3.6 through 3.9. In all cases, we assume that the thundercloud charge is removed by a lightning discharge from

10 km altitude. Results obtained for given charge values at 10 km altitude are valid for different combinations of charge value and altitude as long as the total thundercloud dipole moment is kept constant. From this point of view, the variation of the altitude of the charge is equivalent (in terms of the resultant physical effects) to the variation of the value of charge at a given altitude, and vice versa. For instance, a 100 C charge removed from 10 km altitude produces approximately the same effects in the lower ionosphere as a 50 C charge removed from 20 km altitude.

### 3.3 ELECTRIC FIELD AND CHARGE DENSITY

Figures 3.2 and 3.3 show the results of model calculations for the case of dipole thundercloud charges of  $\pm 200$  C. These results are similar to the monopole case considered in [Pasko *et al.*, 1995] and marked M1 in Figure 2.1. The slow ( $\tau_f = 0.5$  s) build-up of the charges leads to the formation of small but finite quiescent quasi-electrostatic fields, which are similar in nature to the fair weather electric field produced by the charges maintained on the earth [e.g., Uman, 1974; Ogawa, 1985]. The removal of a positive charge in  $\tau_s = 1$  ms leads to the appearance of electric fields of up to  $\sim 100$  V/m at ionospheric altitudes. Figure 3.3 shows the spatial distribution of the charge density  $\rho$  and the electric field  $\vec{E}$  just before ( $t = 0.5$  s) and right after ( $t = 0.501$  s) the cloud-to-ground lightning discharge and at  $t = 1$  s. The physical causes of the “explosive” appearance of the electric field at higher altitudes at  $t = 0.501$  s (as already briefly discussed in Section 3.1) can be understood as follows:

As the thundercloud charges accumulate before the lightning discharge, free charges in the mesosphere and lower ionosphere redistribute (Figure 3.3, top left panel) to create an electric field  $\vec{E}$  approximately equal and opposite to the “applied” electric field  $\vec{E}$  due to the large thundercloud charges. Once the thundercloud charge of any polarity is removed, only the electric field  $\vec{E}$  due to the charge remaining in thundercloud and the space charge above it remains, and this large field endures for a time determined approximately (see discussion

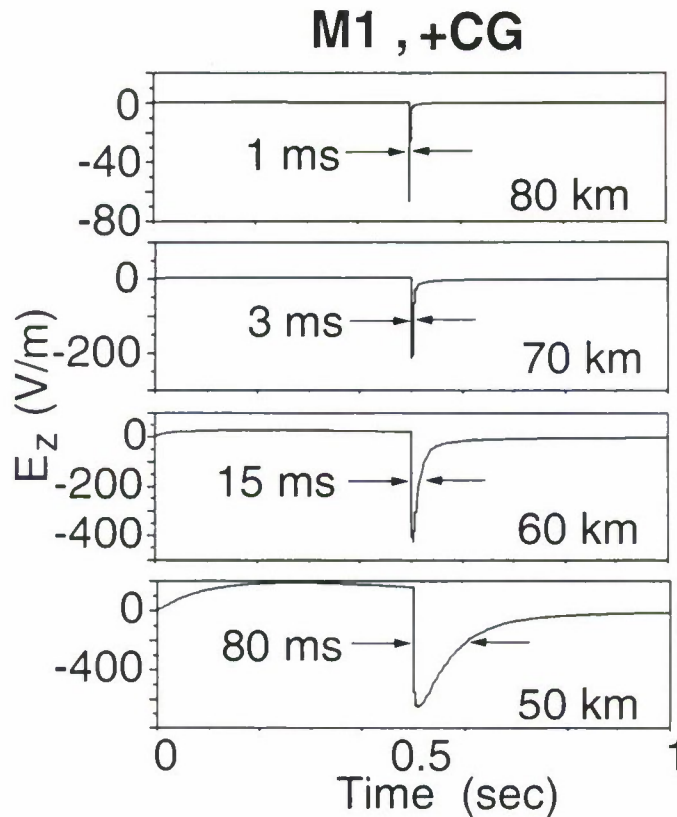


**Fig. 3.2. Temporal variation of the quasi-static electric field.** The establishment and relaxation of the  $z$  component of the electric field at various altitudes at  $r=0$  km for the +CG and M1 models of charge removal (see Figures 2.1 and 2.2).

in Section 3.10) by the local relaxation time ( $\tau_r = \epsilon_o/\sigma$ ) at each altitude. As we discussed in Section 3.1, since charge removal can alternately be viewed as the “placement” of an identical charge of opposite sign, the initial field at ionospheric altitudes is approximately the free space field due to the “newly placed” charge and its image in the ground. Thus, the important physical consequences depend primarily on the magnitude and altitude of the removed charge and are essentially independent of the configuration of all other charges in the system. In this regard we note that +CG and M1 models of charge removal (Figure 2.1) lead to essentially the same electric fields at ionospheric altitudes as is discussed further in Section 3.8.



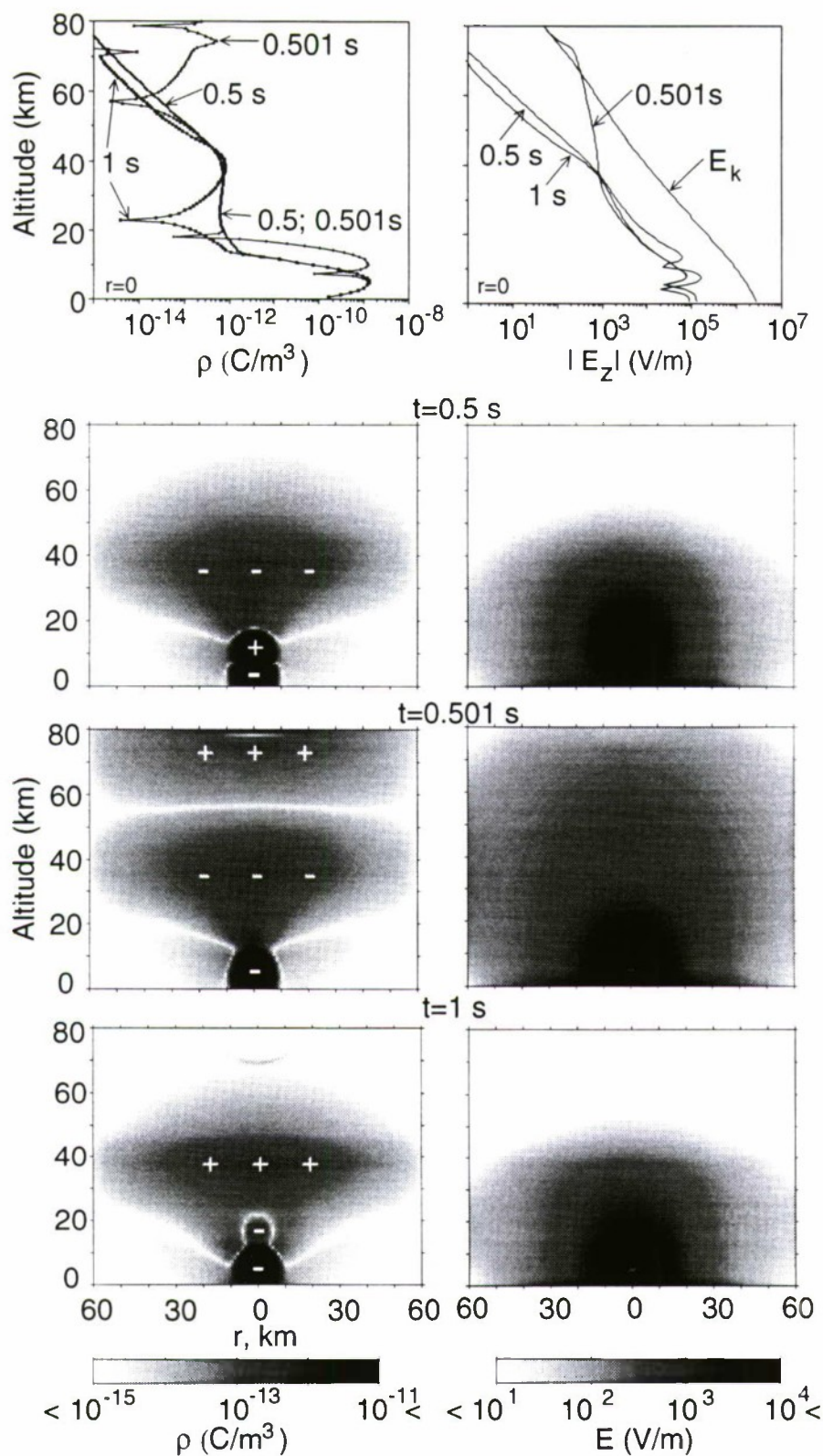


**Fig. 3.3. Electric field and charge density.** A cross sectional view of the distribution of the absolute values of the charge density  $\rho$  (left panels) and the total electric field  $E$  (right panels) at selected instants of time. The top panels show altitude scans at  $r=0$ .

### 3.4 IONIZATION AND ATTACHMENT

Figure 3.4 shows the altitude profile of electron density  $N_e$  and the conductivity  $\sigma$  for different values of removed thundercloud charge  $Q$  ( $Q=50, 100, 150, 200$  and  $250$  C) at the termination of a lightning discharge ( $t=1$  ms). Corresponding profiles of effective electron collision frequency  $\nu_{\text{eff}}$ , which provides a measure of electron heating, are shown in Figure 3.5.

During the charge accumulation stage prior to the lightning discharge, the electric field remains below the critical breakdown field  $E_k$  (see Section 2.4.2) everywhere above the thundercloud (see top right panel in Figure 3.3). However, the large electric field which appears after the removal of the charge exceeds the breakdown threshold  $E_k$  above  $\sim 70$  km altitude, leading to intense ionization changes in the lower ionosphere (Figure 3.4) and optical emissions (Figure 3.9).

For higher values of the removed thundercloud charge  $Q$  we see from Figure 3.4 a transition from a regime in which attachment dominates leading to electron density decreases of several orders of magnitude below ambient values to an ionization regime in which dramatic increases in electron density occur. For low  $Q$  values such as 50 C (Figure 3.4) the attachment and ionization thresholds are not reached, but nevertheless a large change in effective electron collision frequency occurs (Figure 3.5), indicating significant changes in electron conductivity (and thus the total conductivity at altitudes  $>60$  km) purely due to the heating of the electrons.

The changes in the electron density  $N_e$  result in corresponding changes in conductivity  $\sigma$  (right hand panels in Figure 3.4), although the resultant conductivity changes are determined by the interplay between changes in electron density  $N_e$  (due to ionization and attachment) and electron mobility  $\mu_e$  (due to heating) (2.4). For example, the factor of  $\sim 10$  lower conductivity at  $\sim 80$  km altitude for  $Q=200$  C versus 100 C is dominantly due to electron heating, since the electron density changes are relatively small.

The altitude scan of the effective electron collision frequency  $\nu_{\text{eff}}$ , modified by heating,



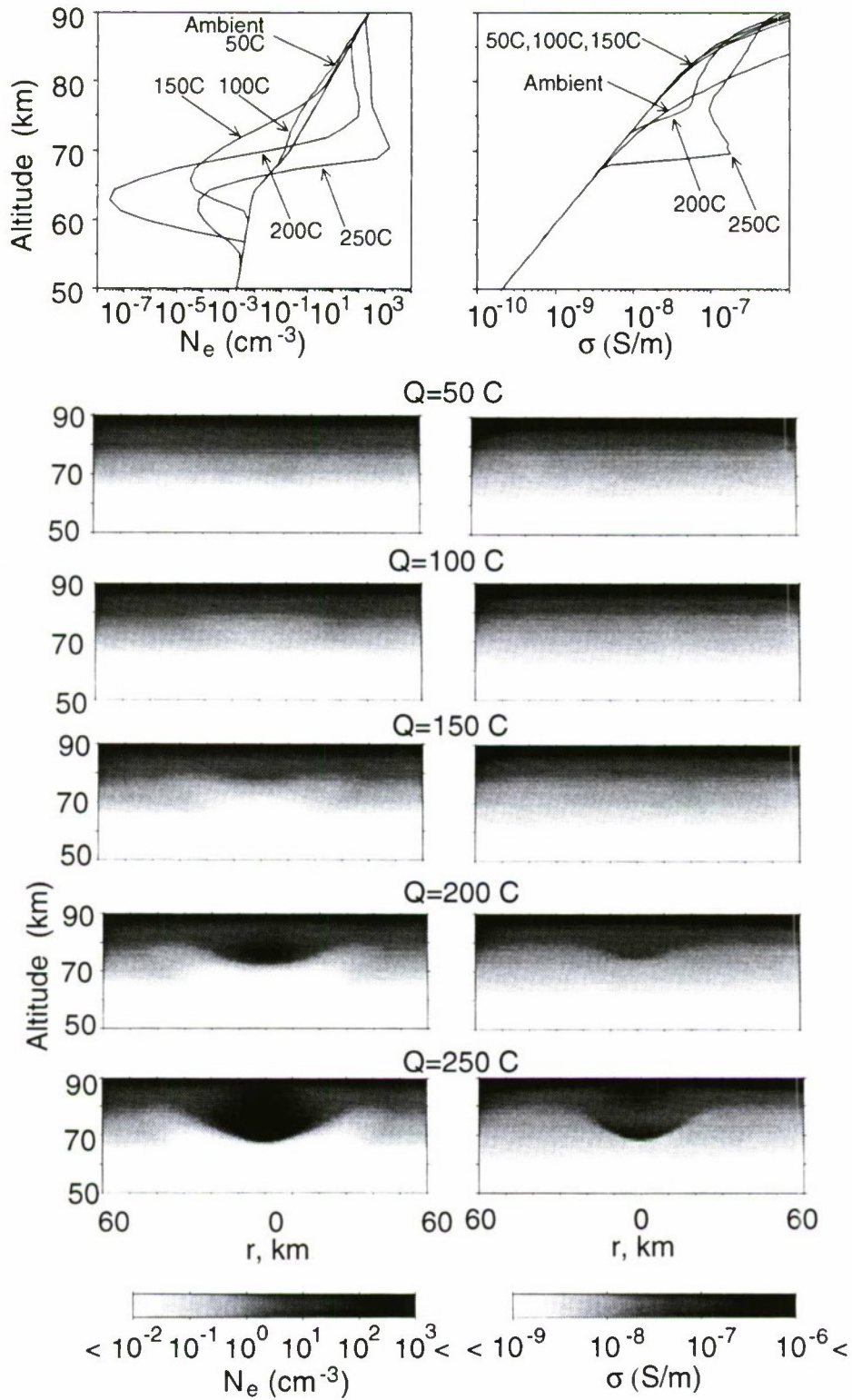


**Fig. 3.4. Model results for electron density and conductivity.** The altitude distribution of the electron density  $N_e$  and conductivity  $\sigma$  for different values of thundercloud charge  $Q$  at the moment of time  $t=1\text{ms}$ . The top panels show altitude scans at  $r=0$ .

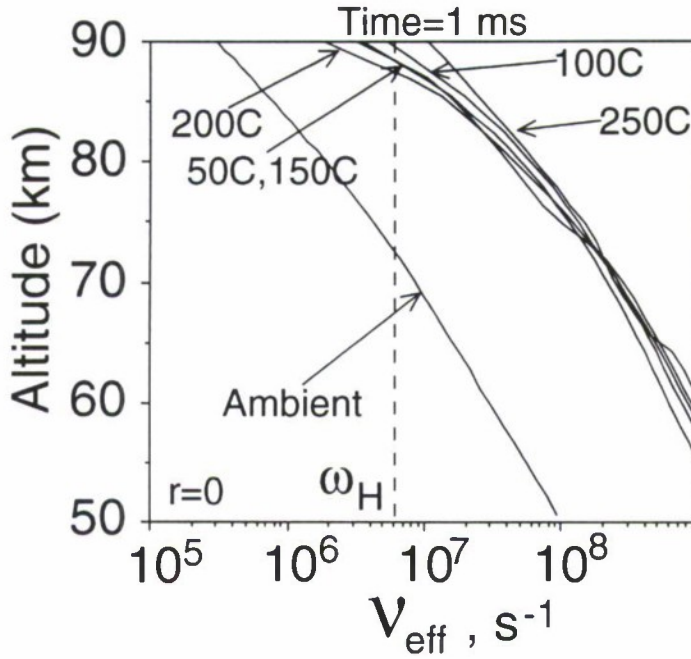


**Fig. 3.5. Model results for effective electron collision frequency.** The effective electron collision frequency  $\nu_{\text{eff}}$  is shown as function of altitude for the same thundercloud charge values as in Figure 3.4.

is shown in Figure 3.5 for the same thundercloud charge values as in Figure 3.4. For purposes of comparison, the electron gyrofrequency is shown in Figure 3.5 by a vertical dashed line. We note that  $\nu_{\text{eff}} > \omega_H$  below  $\sim 87$  km altitude for all charge values considered here. Our assumption concerning the neglect of the effects associated with the external geomagnetic field (Section 2.1) is justified since the most important region of the optical emissions associated with sprites is well below this altitude (see Section 3.5).

The results in Figure 3.4 indicate that quasi-electrostatic fields can significantly change the mesospheric/lower ionospheric electron density  $N_e$  and conductivity  $\sigma$  at  $\sim 50$  to  $90$  km altitudes and in regions with  $\sim 50$ - $60$  km transverse extent. One of the manifestations of such conductivity changes in experimental data may be some early/fast VLF signal perturbations observed in association with lightning discharges and sprites [Inan *et al.*, 1988, 1993, 1995, 1996a].

Often the time period between consecutive discharges from thunderstorm centers [see

*Uman*, 1987, p. 19] is much less than the typical D-region relaxation time for electron density enhancements (10 to 100 s [e.g., *Pasko and Inan*, 1994]). In such cases quasi-electrostatic fields associated with successive lightning discharges as well as electromagnetic pulses (EMP) generated by lightning strokes can lead to accumulation of the ionization or depletion of the electron density in the lower ionosphere leading to the build up of ionization “bubbles” or attachment “holes” above thunderstorms. Such an effect was predicted by *Inan et al.* [1991] and also discussed by *Taranenko* [1993] in relation to heating and ionization produced by electromagnetic impulses generated by lightning.

### 3.5 OPTICAL EMISSIONS

The dynamics of the spatial distribution of optical emissions is shown in Figure 3.6 for  $Q = 250$  C. The local optical emissivities of the first (red) positive band of  $N_2$  excited via impact excitation at different points in a cylindrically symmetric volume were integrated along the horizontal line of sight to determine the emission intensities in Rayleighs observed when viewed horizontally from a distant point.

For direct comparison with video observations of sprites [*Sentman et al.*, 1995] the optical emissions are averaged over the total duration of sprite luminosity ( $\sim 1.6$  ms), which in this case is substantially less than the duration of one video field ( $\sim 16$  ms). Results of the averaging are shown in the lower two panels and are in good agreement with observations of the upper part (“head” and “hair” [*Sentman et al.*, 1995]) of the sprites. Following the occurrence of the cloud-to-ground discharge, the optical emission initially starts at high altitudes and then moves down, its motion being controlled by the development of ionization and the relatively more rapid relaxation of the electric field at higher altitudes. We note that since the total duration of the optical emission is approximately one-tenth the duration of one video field, the maximum intensity of  $\sim 10^5$  kR corresponds to  $\sim 10^4$  kR when averaged over a 16 ms field, a value larger than the maximum reported intensity ( $\sim 500$  kR) of sprites [*Sentman et al.*, 1995] by a factor  $\sim 10$ -100 when viewed through the center of the heated

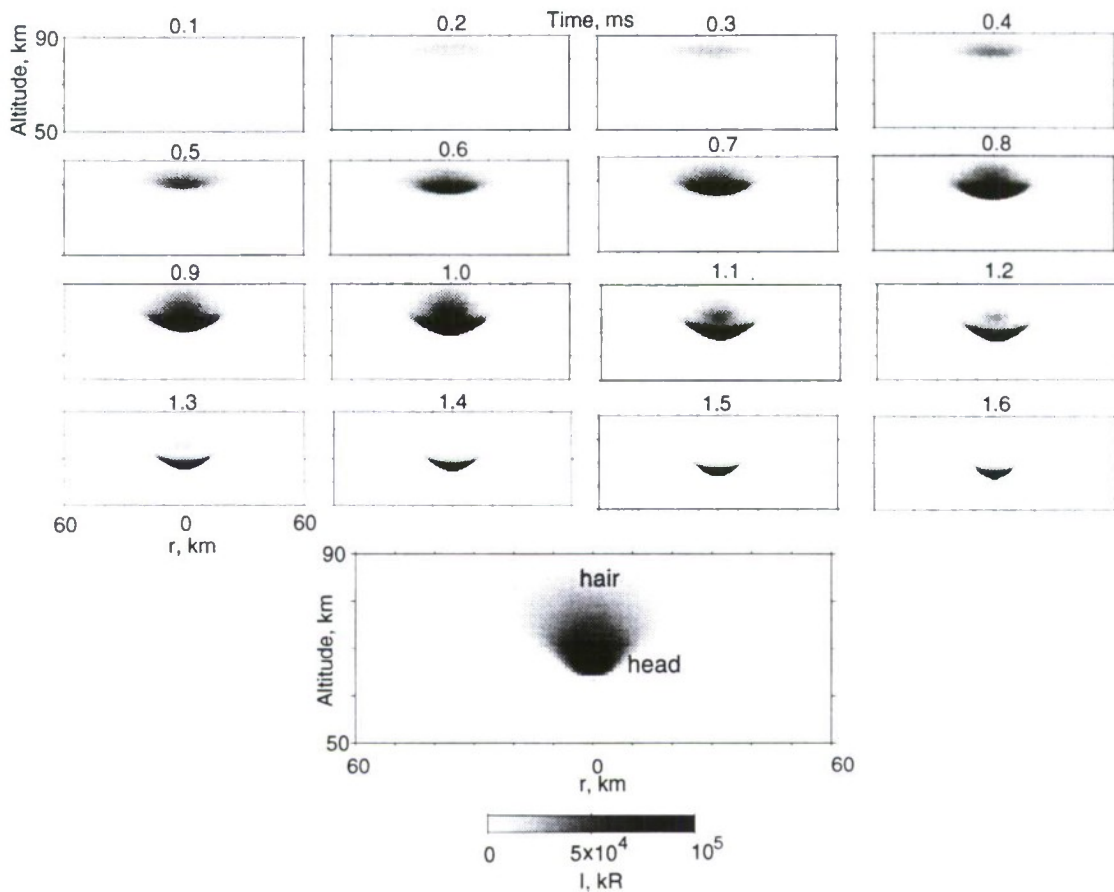


**Fig. 3.6. Space-time dynamics of optical emissions.** The distribution of intensities (in units of Rayleighs) of emissions of the 1st positive band of  $N_2$  as a function of time for the case of 250 C charge removed from altitude 10 km in 1 ms. The bottom panel shows the corresponding quantities averaged over a time of 1.6 ms.

region (at  $\sim 70$  km). This apparent discrepancy is likely due to the response of the optical instruments used to observe sprites.

It is important to note that the optical excitation rates for selected bands (i.e., 1st positive band of  $N_2$ ) are calculated using integral cross sections which do not provide information about the particular wavelength of emitted photons [Taranenko *et al.*, 1993]. Typical video cameras have well defined red, green, and blue filters [e.g., Wescott *et al.*, 1995a] (an example is shown in upper left corner of Figure 3.7) which extract only a narrow part of the spectrum in the visible range of wavelengths. To determine the number of photons corresponding to the 1st positive band of  $N_2$  which produces, for example, the red response



of the video camera, one needs to integrate the normalized distribution of emissions in different wavelengths over the band corresponding to the red filter. This consideration is important since most of the energy of the  $N_2$  1st positive band is distributed in the infrared region of the spectrum with only a small fraction in the visible region covered by the red video filter.

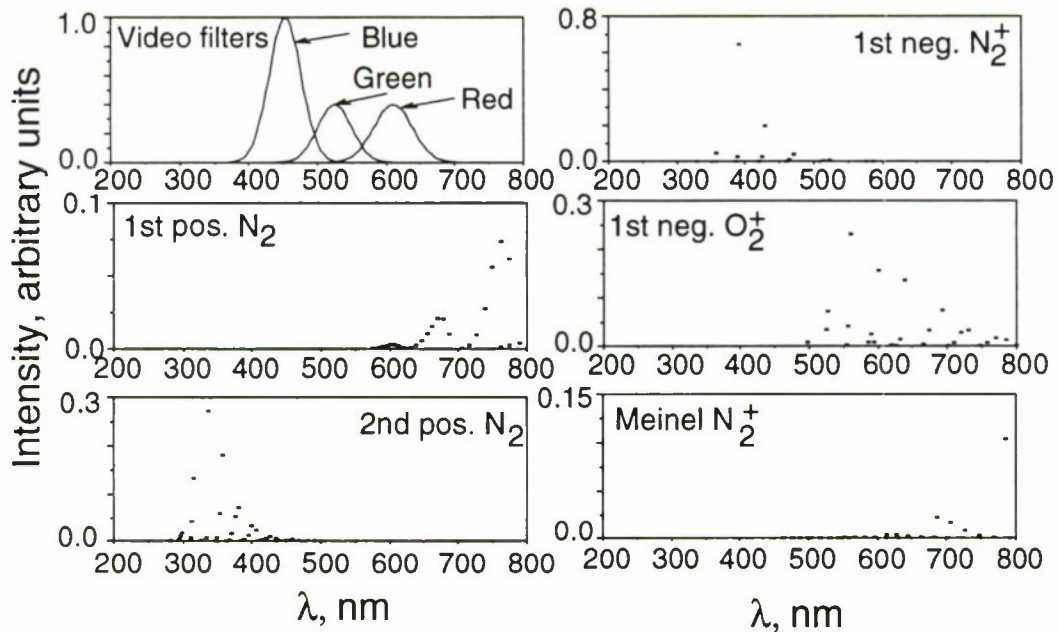


**Fig. 3.7. Optical emission intensity as a function of wavelength.** Normalized (to unity) distribution of optical emission intensity as a function of wavelength (assumed to be the same as in aurora) corresponding to different optical bands. Top left corner shows typical red, green, and blue video filters.

The distribution of the intensities as a function of wavelength within all of the different optical bands corresponding to sprites is not yet known. However, on the basis of the first spectral observations of the 1st positive band of  $N_2$  associated with sprites [Mende *et al.*, 1995; Hampton *et al.*, 1996] (see also Section 1.2.8) the distribution of intensities of the different wavelengths within this band appear similar to that observed in auroral emissions [Valance Jones, 1974, pp.129-132,139] (Figure 3.7). Although the wavelength distribution

for the various components of other emission bands is not yet known, we assume in our further calculations below that the distribution within these bands to be also similar to that in aurorae. Calculations based on this assumption indicate the  $N_2$  1st and 2nd positive bands produce the largest (in comparison with other optical bands) red and blue video response, respectively. Only 1% of the total number of emitted photons corresponding to the  $N_2$  1st positive band appear in the pass band of the red filter of a typical video camera. The corresponding scaling factor for the predominantly blue  $N_2$  2nd positive band is 2.9%. Based on these estimates the optical intensities shown in Figure 3.6 are in good agreement with video observations of sprites [Sentman *et al.*, 1995]. Scaling factors for selected optical bands and different colors calculated on the basis of video filter responses given in [Wescott *et al.*, 1995a] are summarized in Table 3.1. These scaling factors are provided here for illustrative purposes to stress the importance of this type of scaling for the interpretation of the experimental video data, and may be different for video cameras with different technical characteristics. Furthermore, the scaling factors may strongly depend on the assumption on the auroral-like distribution of optical emissions as a function of wavelength within the bands considered.

TABLE 3.1. Video response scaling factors.

Band	Red	Green	Blue
1st pos. $N_2$	$1.04 \times 10^{-2}$	$9.23 \times 10^{-5}$	$5.65 \times 10^{-10}$
2nd pos. $N_2$	$7.10 \times 10^{-8}$	$3.17 \times 10^{-4}$	$2.86 \times 10^{-2}$
1st neg. $N_2^+$	$3.60 \times 10^{-4}$	$5.10 \times 10^{-3}$	$1.80 \times 10^{-1}$
1st neg. $O_2^+$	$1.30 \times 10^{-1}$	$8.60 \times 10^{-2}$	$1.90 \times 10^{-3}$
Meinel $N_2^+$	$3.80 \times 10^{-3}$	$3.63 \times 10^{-4}$	$4.56 \times 10^{-5}$

Figure 3.8 shows the results of time averaging of the optical emission intensity of the  $N_2$  1st positive band for different values of removed thundercloud charge. Values of the maximum intensity of the first positive band corresponding to  $Q=250, 200, 150, 100, 50$  C are  $10^5$  kR,  $10^4$  kR,  $10^3$  kR,  $100$  kR,  $2$  kR, respectively, demonstrating a highly nonlinear dependence of the peak intensity on the removed charge value  $Q$ , as expected on the basis of the threshold-like behavior of the optical excitation cross sections. This result is also consistent with the experimental fact that sprites are associated with only the most intense (usually positive [e.g., Boccippio *et al.*, 1995]) lightning discharges.

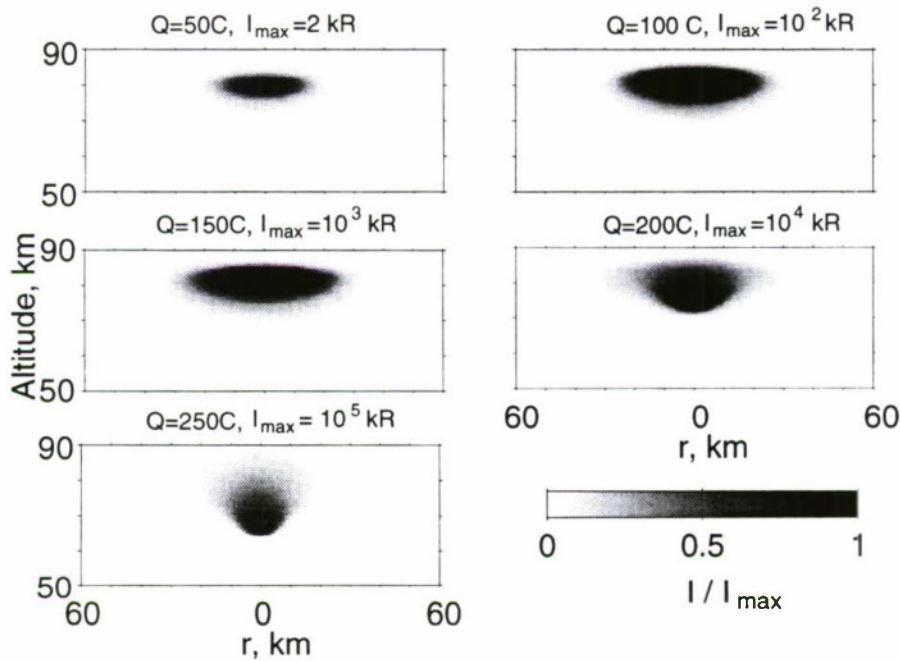


**Fig. 3.8. The distribution of time-averaged optical emission intensity.** The distribution of the time-averaged intensity (in units of Rayleighs) of emissions of the 1st positive band of  $N_2$  is shown on linear scale and for different values of removed thundercloud charge. It was assumed in all cases that the charge was removed by a lightning discharge from 10 km altitude in 1 ms.

The highly nonlinear dependence of the optical emission intensity on  $Q$  as demonstrated

in Figure 3.8 is also supported by the altitude profiles of resultant optical emission intensity at the termination of the lightning discharge ( $t = 1$  ms) as shown in Figure 3.9a for different values of thundercloud charges.

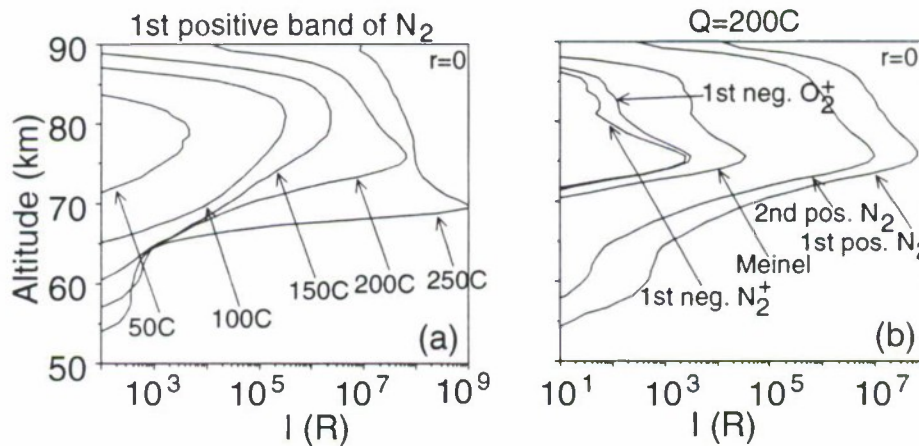


**Fig. 3.9. Instantaneous optical emission intensity.** (a) Altitude scans at  $r=0$  of optical emission intensity corresponding to 1st positive band of  $N_2$  for different values of removed thundercloud charge; (b) Altitude scans at  $r=0$  of optical emission intensity corresponding to different optical bands for  $Q=200$  C.

The altitude distribution of the optical intensities corresponding to the first and second positive bands of  $N_2$ , Meinel and first negative bands of  $N_2^+$ , and first negative band of  $O_2^+$  are shown in Figure 3.9b. The red band (first positive band of  $N_2$ ) is clearly the dominant optical emission, with its intensity being  $\sim 10$  times larger than that of the blue ( $N_2$  second positive band), consistent with the dominant red color of the sprites [Pasko *et al.*, 1995]. The Meinel band intensity is approximately three orders of magnitude below than that of the  $N_2$  first positive band. The first negative bands of  $N_2^+$  and  $O_2^+$  are approximately four orders of magnitude lower than the intensity of the dominant  $N_2$  1st positive band. These definitive predictions concerning relative excitation levels of different bands provide a basis for direct comparisons with spectroscopic measurements.

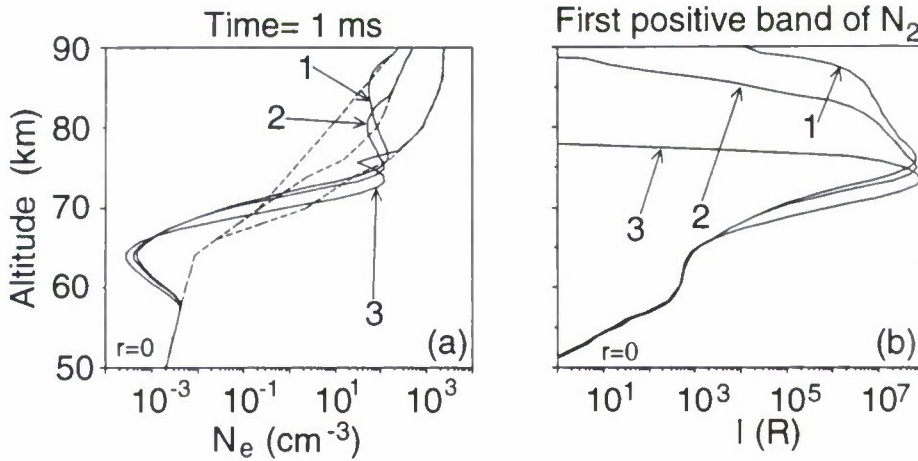


### 3.6 ELECTRON AND ION CONDUCTIVITY

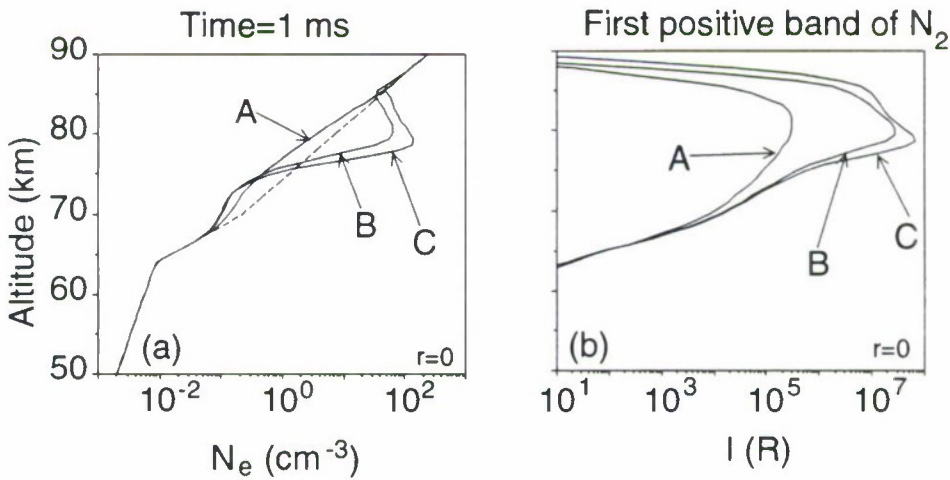
Due to the highly nonlinear nature of the interaction of quasi-electrostatic thundercloud fields with the mesosphere and the lower ionosphere it is expected that both the electron density changes and the optical emission intensities are sensitively dependent on the ambient electron and ion conductivity profiles.

Figure 3.10 compares the electron density changes and optical emission intensities corresponding to the three models of ambient electron number density shown in Figure 2.4a. All of the results shown up to this point have been for the most tenuous ambient electron density (profile 1). Two major effects associated with larger values of ambient electron density (profiles 2,3). Firstly, the relative ionization changes are lower, with the maximum changes occurring at lower altitudes. Secondly, the corresponding optical emission intensities are dramatically reduced at the higher altitudes. Both effects are due to the shorter relaxation time of the electric field at high altitudes for higher ambient electron densities. The peak intensity of optical emissions at  $\sim 70$  km is not affected by the ambient electron number density since this quantity is defined mostly by the amplitude of the electric field (in other words by the value and amplitude of the removed thundercloud charge).

The dependence of ionization and optical effects on the ambient ion conductivity is illustrated in Figure 3.11. For the same value of the removed thundercloud charge (100 C), but for different ion conductivity profiles, we find either depletion in electron density due to attachment or increased density due to ionization. In terms of optical emissions, the results obtained with profiles B, C and A differ by more than two orders of magnitude at  $\sim 80$  km. We note that the ion conductivity profiles A and C are similar to ion conductivity profiles experimentally measured and/or used in previous studies [e.g., *Dejnakarintra and Park, 1974; Holzworth et al., 1985*]. Our results for these two profiles can thus be considered respectively as lower and upper bound estimates of expected levels of optical emissions and ionization changes.



**Fig. 3.10. Dependence on the ambient electron density.** (a) Results of calculations for electron density changes corresponding to different models of ambient electron density (Figure 2.4a). The ambient profiles of electron density are shown for reference by dashed line; (b) Dependence of the optical emission intensity on the model of ambient electron number density (Figure 2.4a). It was assumed in all cases that a charge of 200 C was removed by the lightning discharge from 10 km altitude in 1 ms.



**Fig. 3.11. Dependence on the different ambient ion conductivity.** Dependence of the optical emission intensity (right panel) on ambient ion conductivity (Figure 2.4b). Left panel shows results of calculations for electron number density changes. The assumed ambient profile of electron density is shown for reference by dashed line. It was assumed in all cases that a charge of 100 C was removed by the lightning discharge from 10 km altitude in 1 ms.

### 3.7 LIGHTNING DISCHARGE DURATION

The production of intense optical emissions by quasi-electrostatic fields does not necessarily require large charge transfer rates from cloud to ground. In this context, it is important to

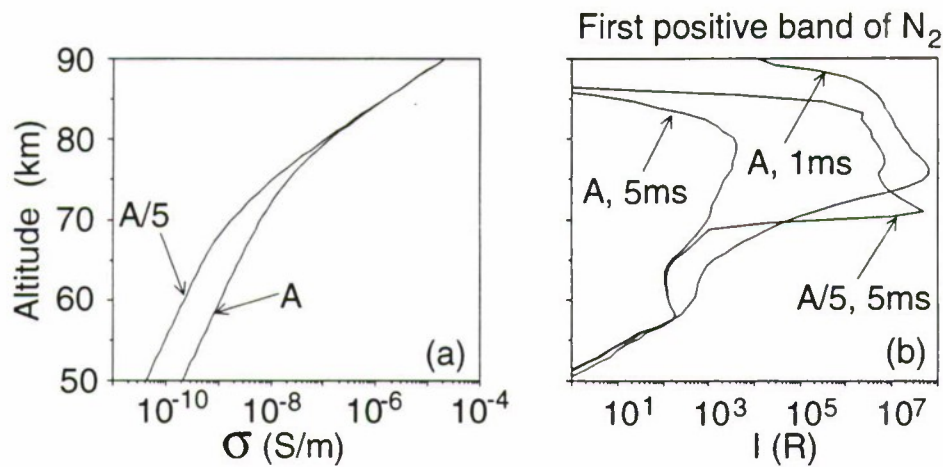


**Fig. 3.12. Model results for different discharge durations and ambient conductivity profiles.** Dependence of the optical emission intensity (right panel) on ambient conductivity profile (left panel) and discharge duration (1 ms and 5 ms). It was assumed that a charge of 200 C was removed by the lightning discharge from 10 km altitude.

note that in all of the results shown up to now the duration of the lightning discharge was assumed to be 1 ms. The rate of charge transfer required for achieving observable levels of optical emissions depends, in addition to the magnitude of the total removed charge, upon the conductivity profile in the 60-90 km altitude range, and the corresponding relation between the duration of the discharge and the specific relaxation time of the electric field in the conducting medium. If we assume that the value of the total removed charge remains constant the observable levels of optical emissions considered in previous sections can still be achieved with longer charge transfer times as long as they do not significantly exceed the relaxation time at 50-90 km altitudes.

To illustrate this point, we show in Figure 3.12 results for two different ambient ion conductivity profiles which differ by a factor of five at  $<60$  km altitudes where the ion conductivity is dominant. Profile A/5 shown in Figure 3.12 represents conductivity values reduced by a factor of 5 with respect to profile A. We assume the electron component of the ambient conductivity to be the same for both profiles, and determined by the electron density profile 1 shown in Figure 2.4a.

Optical emission intensities corresponding to two different durations of the lightning



discharge (1 ms and 5 ms) for profile A, and for 5 ms duration for profile A/5 are shown in the right hand panel of Figure 3.12. Results shown correspond to times at the termination of the lightning discharges (i.e., 1 ms or 5 ms). The intensity of the optical emission is significantly reduced for profile A and the 5 ms discharge duration in comparison with the 1 ms case. However, the intensity distribution is similar for profile A with 1 ms discharge duration and profile A/5 with the 5 ms duration. The fast drop of the optical emission intensity above 85 km altitude for the latter case is due to the increase of conductivity of the medium resulting from ionization. Since the range of known ion conductivity profiles span more than an order of magnitude at mesospheric altitudes (Figure 2.4b), one can conclude that similar optical emission intensities would occur with charge removal times substantially longer than the 1 ms used in most of the calculations reported in previous sections. For lower ion conductivities, the predicted optical output would be different primarily in terms of the duration of the emission at ionospheric altitudes. The peak optical emission intensities do not depend significantly on the ambient conductivity profile since this quantity is determined primarily by the magnitude of the electric field (and thus the value and the altitude of the removed thundercloud charge). The latter point was already mentioned as part of the discussion of results corresponding to different ambient electron density profiles (Figure 3.10), and is also illustrated by the results shown in Figure 3.11 indicating a saturation effect corresponding to profiles B and C. Further reduction of conductivity at mesospheric altitudes (below those represented by profile C) would not produce a significant increase in the optical emission intensity or the ionization.

Although up to now we have primarily considered the removal of  $\leq 300$  C of charge in  $\sim 1$  ms, removal of larger amounts of charge (e.g.,  $\sim 400$  C) over longer times (e.g.,  $\sim 10$  ms) may lead to the formation of streamer-type channels of breakdown ionization at altitudes  $\sim 50$ -70 km. This regime of excitation and various consequences are discussed in Chapter 4.



### 3.8 LIGHTNING DISCHARGE TYPE

Figure 3.13 shows postdischarge distributions of electric field and optical emission intensity as a function of altitude for three different lightning discharge models, M1, M2 and +CG as shown in Figure 2.1. We note that the M2 case corresponds to the deposition of a monopole charge, in contrast to removal of charge as represented by the M1 and +CG cases.

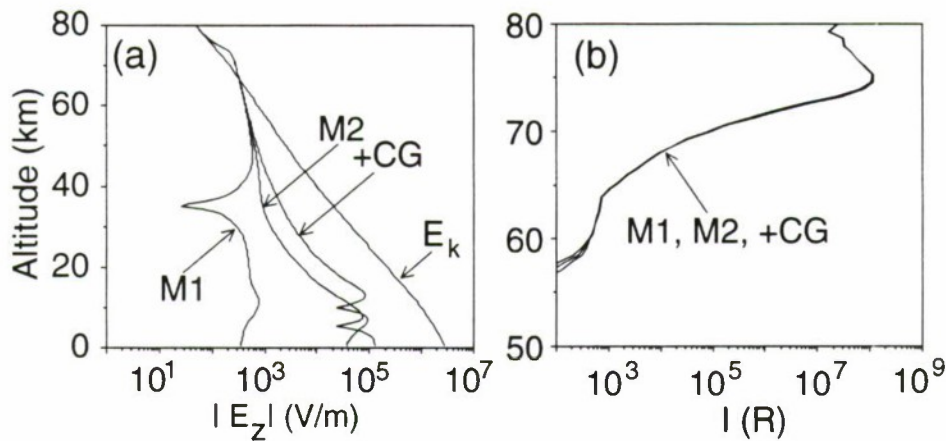


**Fig. 3.13. Results for three different models of lightning discharge.** Dependence of the optical emission intensity (right panel) on the model of lightning discharge (M1, M2, +CG) (Figure 2.1). Left panel shows the corresponding distribution of postdischarge electric field at  $\tau = 0$ . All calculations were performed for the removed charge value 200 C.

The results obtained for three different lightning discharge models are identical above  $\sim 60$  km altitude, as expected since the electric field at high altitudes is defined mainly by the value of the removed/deposited charge and its altitude, independent of the charge configuration inside the cloud before or after the lightning discharge. The range of altitudes over which the electric field is independent of the lightning discharge model extends lower with increasing charge accumulation time. In this Chapter we use a charge accumulation time of  $\tau_s = 0.5$  sec [Pasko *et al.*, 1995] since optical emissions appear at altitudes well above 60 km. Calculations with  $\tau_s$  longer than 0.5 sec lead to identical results, and  $\tau_s = 0.5$  sec value was chosen from the point of view of computational efficiency.

Figure 3.14 shows results for +CG, -CG and IC discharges. The +CG flashes clearly produce larger electric fields and optical emission intensities, with the optical intensity being three orders of magnitude above that for -CG and IC. This result is a simple consequence of the fact that +CG discharges remove charge from the higher altitude, producing larger values of postdischarge electric fields. Note that for the IC case the field of the lower removed charge significantly reduces the field of the upper charge and the resulting optical output. It should be noted that we model a +CG discharge as the removal of the thundercloud positive charge which is assumed to be located at a higher altitudes than the accompanying negative charge. In a real situation, positive charge may well be accumulated at and removed from the lower parts of the thundercloud [e.g., *Boccippio et al.*, 1995; *Marshall et al.*, 1996].

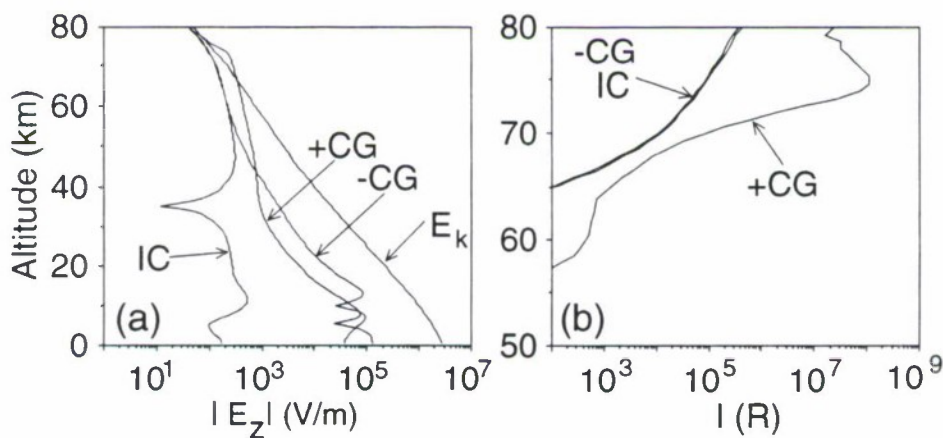


**Fig. 3.14. Dependence on the type of lightning discharge.** Results are shown in the same format as in Figure 3.13 but for +CG, -CG, and IC (Figure 2.1) models of the lightning discharge.

### 3.9 THUNDERCLOUD CHARGE GEOMETRY

The dependence of optical emission characteristics on the geometry of the thundercloud charge is of particular interest since sprites usually appear above mesoscale convective systems with spatially distributed charges [E. Williams, private communication; Boccippio *et al.*, 1995; Marshall *et al.*, 1996]. Figure 3.15 shows the postdischarge distribution of electric fields and optical emissions corresponding to +CG discharge for three different geometries of the thundercloud, namely, (1) Gaussian spherically symmetric charge density distributions with scale  $a=3$  km (used in most of the calculations in this thesis); (2) Also Gaussian spherically symmetric distribution but with  $a=6$  km; (3) Gaussian distribution in the  $z$  direction with  $a=3$  km and flat (uniform) in the horizontal direction with a “disk” of radius 30 km.

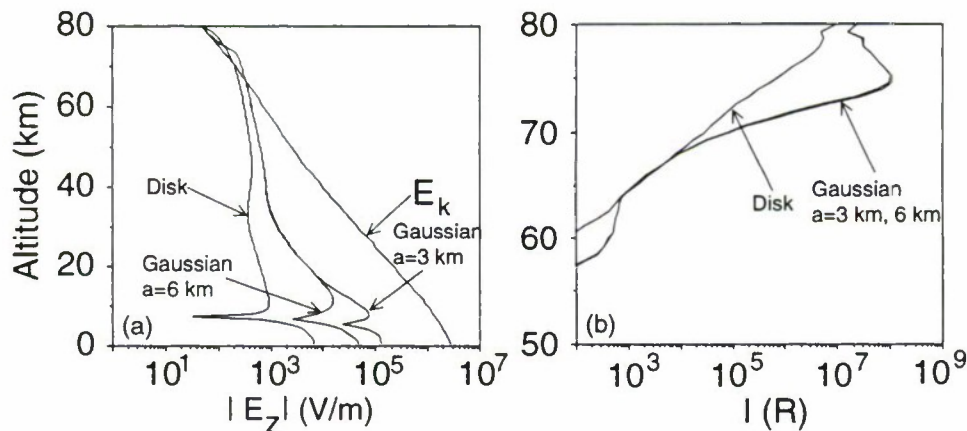


**Fig. 3.15. Dependence on the thundercloud charge geometries.** Results of calculations of postdischarge electric fields (left panel) and optical emission intensities of the first positive band of  $N_2$  (right panel) for thundercloud charge distributions of: (i) Gaussian spherically symmetric charge density distributions with scale  $a=3$  km (used in most of the calculations in this thesis); (ii) Also Gaussian spherically symmetric distribution but with  $a=6$  km; (iii) Gaussian distribution in the  $z$  direction with  $a=3$  km and flat (uniform) in the horizontal direction with a “disc” of radius 30 km.

The results in Figure 3.15 show that horizontally spread charges generally lead to a lower value (for the same value  $Q$  of the removed thundercloud charge) of the electric fields



everywhere above the thundercloud. The size of the spherical thundercloud charges (3 and 6 km scales) does not appear to significantly affect the electric fields and optical outputs at mesospheric and ionospheric altitudes. In this connection it is interesting to note that if there were no upper conducting boundary (ionosphere), increasing the effective radius of the disk of charge would tend to approach the one dimensional geometry of the electric field due to a sheet of charge. Since the thundercloud charge always has an image charge below the ground, the field would be enhanced between the disk and ground but would rapidly decrease above it with increasing disk radius. Since the ionospheric boundary also generates an image charge, the amplitude of the field is relatively enhanced. Results of calculations shown in Figure 3.15 suggest, however, that the spherical geometry gives the largest possible amplitudes of electric fields above the thundercloud. On the other hand, the disk projects a significant electric field over a wider (in the radial direction) region of space.

The electric field above the stratiform clouds associated with mesoscale convective systems have been measured by *Marshall et al.* [1996] using balloon-borne instruments. The measured amplitudes of electric fields were explained by considering the disk charge with charge density  $\sim 3 \text{ nC m}^{-3}$  centered at 4 km altitude, with thickness 400 m (effective surface charge density  $\sim 1200 \text{ nC m}^{-2}$ ) and diameters ranging from 20 to 200 km. The authors accounted for image charge in the ground, but ignored the effects of ionospheric images. The effects of the upper ionospheric boundary must be taken into account for a correct determination of the electric field values at ionospheric altitudes and the total charge accumulated in the thundercloud, especially for horizontally spread charge distributions. We note that even relatively small values of charge (200 C) distributed over a disk with diameter 60 km (surface charge density only  $\sim 100 \text{ nC/m}^2$ ) would lead to  $\sim 1 \text{ kV/m}$  electric field change above the thundercloud (Figure 3.15), in excellent agreement with observations of *Marshall et al.* [1996]. Thus relatively large values  $\sim 1200 \text{ nC/m}^2$  suggested by *Marshall et al.* [1996] and derived without accounting for the effects of the upper ionospheric boundary may not in fact be required for production of observed amplitudes of the electric field.



### 3.10 RELAXATION TIMES OF QUASI-ELECTROSTATIC FIELDS

The dynamics of the electric field in the conducting medium above thunderclouds directly control the ionization changes and the duration of optical emissions associated with sprites. An important aspect of our model with respect to previous work on the relaxation of quasi-electrostatic fields [Dejnakarintra and Park, 1974; Greifinger and Greifinger, 1976; Hale and Baginski, 1987; Baginski et al., 1988; Hale, 1994] is the self-consistent modeling of the conductivity  $\sigma$ , as discussed in Section 2.4. To demonstrate the importance of the self-consistent treatment of conductivity in comparison with previous work, we compare in Figure 3.16 the temporal variation of the electric field  $|E_z|$  at 70 and 80 km for three different treatments of conductivity  $\sigma$  for the case of removal of a monopole charge (case M1 shown in Figure 2.1).

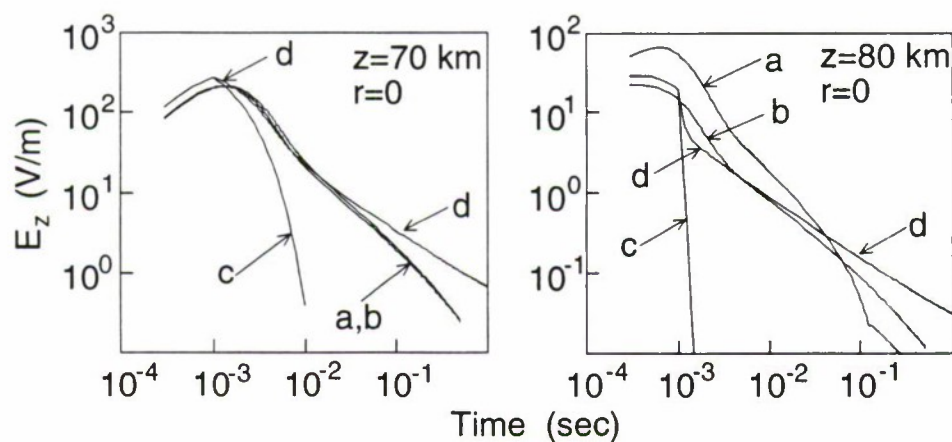


**Fig. 3.16. Relaxation of the quasi-electrostatic field.** The vertical component of the electric field at two selected altitudes at  $r = 0$  as a function of time since the beginning of the lightning stroke for a 200 C source charge for different solutions of conductivity  $\sigma$ : (a) self-consistent formulation; (b) conductivity kept constant in time; (c) relaxation with the local ambient relaxation time ( $\epsilon_0/\sigma$ ); (d) same as (b) but for charge deposited during 1 ms (M2, Figure 2a) (rather than removal) at the beginning of the simulation.

At  $z = 80$  km, the electric field  $|E_z|$  for case (a) is  $\sim 4$  times that for (b), and initially exhibits  $\sim 3$  times longer time duration, followed by a faster decrease, resulting from the

initial decrease of conductivity  $\sigma$  due to heating followed by its increase due to ionization at later times. For case (d) at both altitudes (70 and 80 km) the relaxation rate of the electric field slows down even in comparison with cases (a) and (b); this effect is due to the formation of the quiescent electric field around the source charge. This steady field can be found as the stationary solution of the problem of a point charge in a medium with exponentially increasing (in altitude) conductivity [e.g., *Holzer and Saxon*, 1952]. In all cases, we see significant slowing down of the relaxation rate of the electric field in comparison with the local ambient  $\epsilon_0/\sigma$  (marked (c) in Figure 3.16) rate. The most recent discussion of this effect, which has been observed experimentally and extensively studied theoretically, is given by *Hale* [1994] (see also references cited therein).

Since the slowing down of the electric field relaxation rate is observed on a millisecond time scale [e.g., *Dejnakarintra and Park*, 1974; *Baginski et al.*, 1988; *Hale*, 1994] our quasi-electrostatic formulation which is valid for the near zone fields is fully sufficient for the investigation of the temporal evolution of the quasi-static fields and its consequences in the form of heating, ionization and optical emissions. That this is so can also be confirmed by recent results of *Baginski and Hodel* [1994] who provide a detailed comparison of the solution of the system of equations (2.1) and (2.2) with the full system of Maxwell equations.

The slowing down effect can be physically understood as follows. The atmospheric conductivity exponentially increases with altitude. There exists an altitude below which we can consider charges (both thundercloud and induced polarization charges in the conducting atmosphere) to be “stationary” on a certain time scale. The slowing down of the electric field relaxation can be interpreted as the establishment of a quasi-stationary solution above this “stationary” charge. As time progresses, the imaginary boundary below which we can consider charges and associated fields to be stationary moves downward [e.g., *Greifinger and Greifinger*, 1976]; however, the rate of the field and charge relaxation above this boundary always remains slower than the local relaxation rate  $\epsilon_0/\sigma$ . At each altitude above this boundary there is a nonvanishing value of induced charge and current density which is a consequence of the inhomogeneity of the atmospheric conductivity [*Greifinger*

and Greifinger, 1976]. The relaxation rate would be even further slowed down if there is a source charge which is maintained by an external effect (e.g., regeneration of charge within the thundercloud due to updraft). Such a circumstance is represented by the deposition of charge over 1 ms, as in the case marked (d) in Figure 3.16.

The imaginary downward moving boundary mentioned above is essentially the “moving capacitor plate” model introduced first by *Greifinger and Greifinger* [1976] and successfully used by *Hale and Baginski* [1987] to estimate the current which flows to the ionosphere following a lightning stroke. *Greifinger and Greifinger* [1976] define this boundary as separating two regions dominated by conduction (above) and displacement (below) currents.

Any persisting charges at low altitudes constitute a source of electric field at high altitudes, so that the electric field at high altitudes completely relaxes to zero only when the last remaining charges dissipate at low altitudes, a process which occurs with long relaxation times due to low atmospheric conductivity. Until such time that the polarization charges at the lowest altitudes dissipate away, the electric fields at high altitudes continuously goes through a series of quasi-stationary states corresponding to persisting at low altitudes charges. This effect leads to the apparent slowing down of the relaxation of the electric fields.

An important role is played by surface charges induced at the highly conducting ground and lower ionospheric boundaries which are assumed to be maintained at a constant potential. These charges change dynamically in time consistent with the electric fields and correspondingly affect the dynamics of the fields. The slowing down effect is not a property of two-dimensional system and is also observed in one dimensional geometry.

To illustrate the above points, we show in Figure 3.17 results obtained for cases similar to those shown in Figure 3.16b,d, but for the deposition and removal of a “disk” of charge of 10 C with radius 150 km and vertical extent 3 km. The radial size of the system was assumed to be also 150 km by adopting the boundary condition  $\partial\varphi/\partial r = 0$  at  $r = 150$  km. The electric field in this case is essentially one-dimensional and is directed vertically everywhere in the system. Similar to those of Figure 3.16, results of Figure 3.17 show



slowing down of the electric field relaxation. Note that the field shown is that at 50 km altitude so that the relaxation of the field in this case is entirely determined by the gradients of conductivity and persisting charges (no heating effects included).

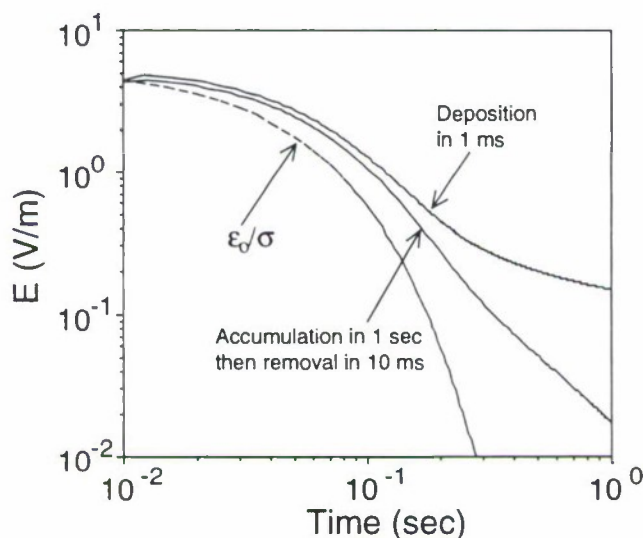


**Fig. 3.17. One dimensional relaxation of the electric field.** The electric field at altitude 50 km as a function of time: (i) relaxation with the local ambient relaxation time ( $\epsilon_0/\sigma$ ); (ii) deposition in 10 ms of a disk of charge of 10 C with diameter 300 km and vertical extent 3 km at altitude 20 km; (iii) the same as (ii) but the charge was accumulated during 1 sec and then removed in 10 ms.

In summary, we can identify three separate physical effects which contribute to the slowing down of the relaxation rate of the quasi-static electric field: (i) the decrease of the ambient electron component of the conductivity due to selfconsistent heating by quasi-electrostatic fields; (ii) the generation of additional surface charges at the highly conducting ground and the lower ionospheric boundaries; (iii) the establishment of quasi-stationary distributions of the electric fields and charge densities around persisting thundercloud charges and polarization charges in the conducting atmosphere above the thundercloud.





# 4

## Sprites as Luminous Columns of Ionization

In this chapter we investigate the formation of columnar channels of breakdown ionization and carrot-like vertical luminous structures depending on the dynamics of the thundercloud charge removal by continuing currents associated with positive cloud-to-ground lightning flashes. We show that the quasi-electrostatic thundercloud fields can potentially lead to intense heating and ionization in structures with typical transverse dimension  $\sim 5\text{-}10$  km and spanning an altitude range from  $\sim 80$  km to well below  $\sim 50$  km. These carrot-like forms closely resemble those observed in sprites. We also show that the appearance of optical emissions can be significantly delayed in time ( $\sim 1\text{-}20$  ms) with respect to the causative lightning discharge. We compare results of model calculations with recent video, optical, and photometric observations of sprites.

### 4.1 PHYSICAL MECHANISM

In the previous chapter it was illustrated that large electric field transients capable of causing breakdown ionization at mesospheric altitudes can be produced in the region between the thundercloud tops and the lower ionosphere following the removal of thundercloud charge by a cloud-to-ground discharge (see Figure 3.1 and accompanying discussion in Section 3.1).

During the process of charge removal from the thundercloud (typically 1-20 ms), the intensities of the quasi-electrostatic fields slowly increase, and may exceed the threshold

of breakdown ionization in a localized region. The altitude at which this would occur, and the radial extent of the ionization region, depends on the value of the threshold field, which in turn depends on the atmospheric neutral density. Once the ionization threshold is exceeded, the conductivity in this localized region rapidly increases by typically several orders of magnitude as was shown in the previous chapter. The enhanced conductivity in such a localized region in turn leads to faster rates of electric field relaxation within it and to significantly enhanced electric field in its vicinity, much like the case of highly curved surfaces (sharp edges) of conducting bodies placed in an electric field. If the relaxation rate of the surrounding medium is not high enough to compensate for the enhanced electric field, the field can further exceed the local threshold for breakdown ionization and spatially extend the region of high conductivity. If the curvature of the resultant conductivity inhomogeneity is still large enough, continuous development and propagation of the ionization channel may thus occur. Formation of these ionization channels may be closely associated with streamer type processes characterized as filamentary plasmas, the dynamics of which are controlled by highly localized nonlinear space charge waves [e.g., *Uman*, 1984, p. 202; *Vitello et al.*, 1994]. In general, we might expect the curvature of the inhomogeneity to sharpen (i.e., the effective radius of the ionized column to decrease) as the streamer propagates downward. However, as we show later, depending on the temporal profile of charge removal from the thundercloud ionization columns with a variety of shapes can be created, including radial convergence or divergence of the luminous regions as the streamer moves downward.

On the basis of these arguments, the regions of air breakdown may have the shape of an ionization column(s) which electrically connects the highly conducting lower ionosphere to lower atmospheric regions. An ionization channel may develop from a “seed” enhancement of local conductivity of any origin (see next sections) and its propagation is physically controlled by the relaxation of the electric field inside its conducting body and the enhancement of the field in the vicinity of its tip as described above.

## 4.2 MODEL PARAMETERS

For the calculations in this chapter we assume the ambient electron density profile 1 shown in Figure 2.4a and ambient ion conductivity profile A illustrated in Figure 2.4b. We use the quasi-electrostatic model described in Chapters 2 and 3 for five different models of charge removal shown in Figure 4.1 with time  $t=0$  corresponding to the start of the charge removal process. These lightning discharge models represent the removal of larger amounts of total charge while being consistent with reasonable lightning current values of  $<300$  kA. As a result, generally larger peak magnitudes of electric fields are produced, leading to a different class of effects than those discussed in Chapter 3.

We note that our model is effectively a one fluid model, and in contrast with the two-fluid approaches [e.g., Vitello *et al.*, 1994] it is based on the continuity equation for charge density (2.3) and may not accurately predict the small scale details of the electron density near the steep boundaries associated with the front of streamers. Calculations indicate that downward propagating ionization channels tend to focus to very sharp edges, an effect which often leads to numerical instability at low altitudes ( $\sim 50$  km). For modeling of the downward propagation we somewhat arbitrarily introduce in our model an “effective” recombination constant  $\alpha=1$  cm<sup>3</sup>/s at 50 km which varies exponentially in altitude with a scale height of 6 km, accounting for the increasing electron losses at low altitudes, and also serves as a smoothing factor preventing unphysically large oscillations in the electron number density. For modeling of upward propagating streamers which can be launched from seeds of plasma at low altitudes (see next section) we assume that the dielectric relaxation time ( $\epsilon_0/\sigma$ ) behind the front of the channel remains constant in accordance with the results of extensive streamer simulations [e.g., Vitello *et al.*, 1994]. This assumption also is used in the next chapter for modeling of blue jets. The thundercloud charges  $+Q$ ,  $-Q$  ( $+Q$  placed at 10 km) form a vertical dipole which develops over several tens of seconds. The  $+Q$  charge is then rapidly discharged to the ground. The response of the system at mesospheric altitudes depends on the altitude and magnitude of  $+Q$  and does not depend on the initial charge configuration



inside the cloud (i.e., magnitude and altitude of  $-Q$ ) as was discussed in Sections 3.1 and 3.3.

The top panels of Figure 4.1 show five different models of charge removal used for calculations in this chapter. The time

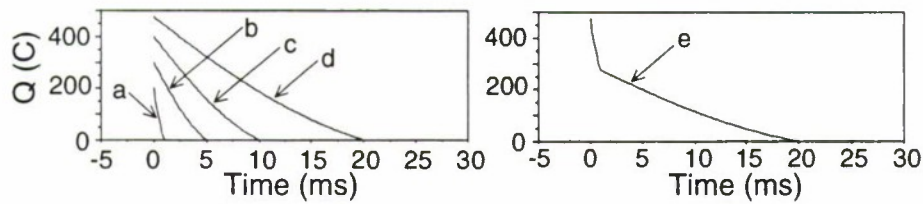


**Fig. 4.1. Models of charge removal.** Five models of thundercloud charge removal used in calculations: (a) removal of 200 C of charge in 1 ms; (b) 300 C in 5 ms; (c) 400 C in 10 ms; (d) 475 C in 20 ms; (e) fast initial removal of 200 C in 1 ms and then slow removal of 275 C in 19 ms.

### 4.3 ELECTRON DENSITY

Results of calculations of the electron number density as a function of time corresponding to case *e* in Figure 4.1 are shown in Figure 4.2a. The case *e* is chosen for detailed discussion since it most closely represents the typical time dynamics of the charge removal from a thundercloud consisting of fast initial removal of a portion of the charge by a lightning stroke followed by a more prolonged period of continuing current [e.g., *Uman*, 1987, p. 200]. At time  $t=2$  ms, a region of significant ionization with characteristic radius  $>10$  km is produced at 70-80 km altitude by the fast (1 ms) removal of the first 200 C, in a manner similar to the cases studied earlier in Section 3.4. Although the electric field is enhanced just outside of this localized region of enhanced conductivity, this increase is compensated by the relatively high ambient conductivity at these altitudes, inhibiting the formation of an

ionization channel. If the removal of charge in this case were limited to 200 C, no ionization channel would be formed and the totality of the resultant effects would be those presented in Chapter 3. In most cases, however, the fast impulsive removal of charge is followed by a period of continuing current which usually lasts tens of ms and can account for a significant fraction of the total charge lowered by a cloud to ground discharge [Uman, 1987, pp. 196, 200]. Such low rates of charge removal can in some cases further increase the curvature of the highly conducting region, leading to the formation of streamer-type channels of breakdown ionization propagating downward as shown in Figure 4.2a. Focusing (Figure 4.2a,  $t = 10$  ms) and subsequent expansion (Figure 4.2a,  $t = 20$  ms) of ionization toward lower altitudes is caused by the fact that the additional slow charge removal enhances the electric field and widens the region of breakdown ionization. This behavior occurs at altitudes ( $< 60$  km) where the ambient conductivity is low enough so that it does not prevent the enhancement of the electric field near the tip of the channel in contrast with that at high altitudes ( $\sim 70$  km).

#### 4.4 ELECTRIC FIELD

The spatial distribution of the enhancement of the electric field above its value at  $t = 15$  ms is shown in Figure 4.2b at different time intervals. The purpose of this kind of normalization is to illustrate the enhancement of the electric field in regions near the tip of the streamer. The characteristic breakdown field  $E_k$  [Papadopoulos *et al.*, 1993] is also shown in the top panel of Figure 4.2b. The electric field remains approximately equal to  $E_k$  at the tip of the streamer. The physical reason for this behavior is the fact that when the electric field exceeds the characteristic breakdown field  $E_k$ , ionization increases lead to enhanced local conductivity which in turn leads to the rapid relaxation of the electric field. As a result, the electric field tends to remain near  $E_k$ . Thus, the ionization channel proceeds with the electric field at its tip staying just barely above the threshold field.

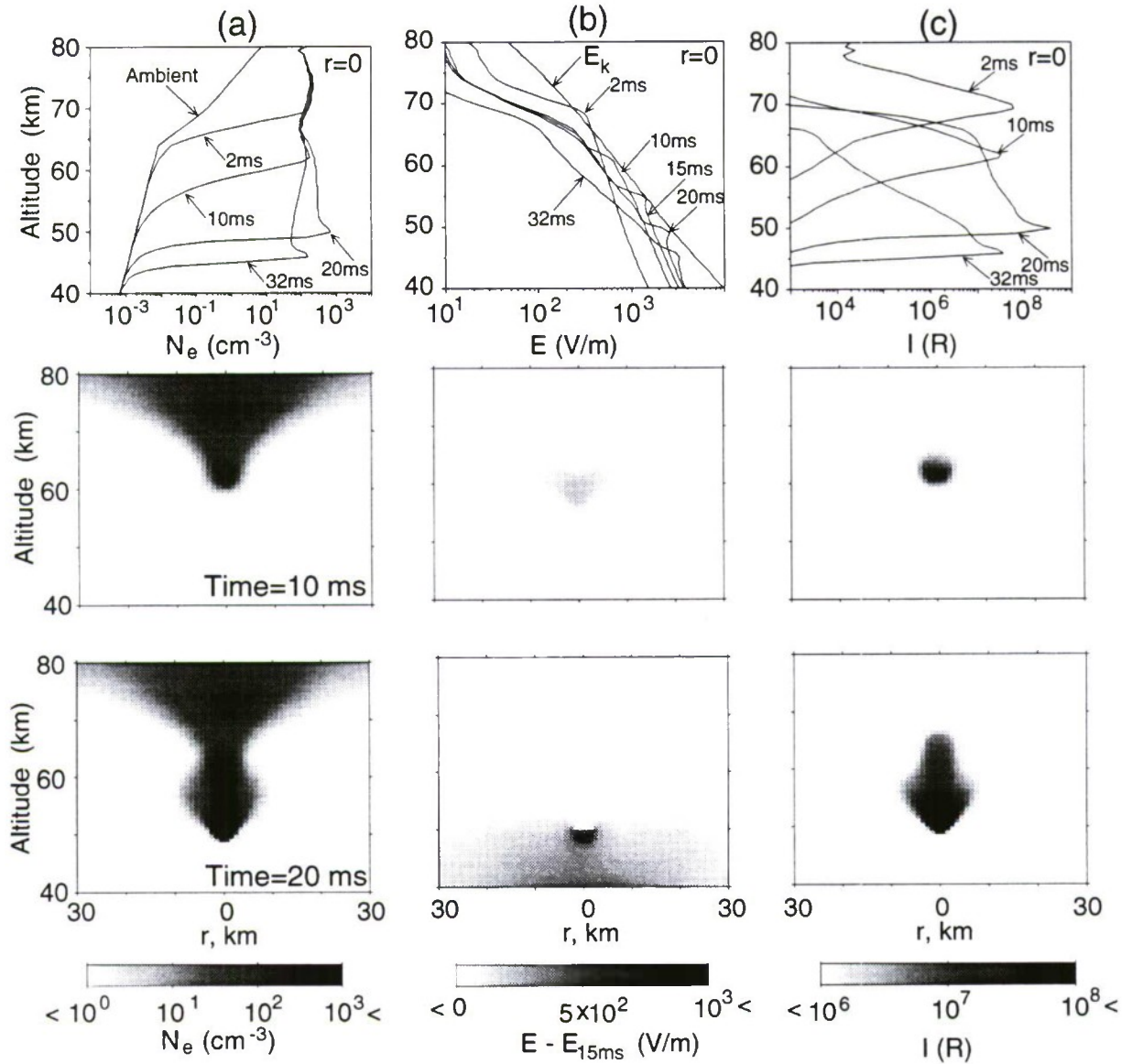


**Fig. 4.2. Formation and downward propagation of an ionization channel.** A cross-sectional view of the distribution of (a) the electron number density  $N_e$ ; (b) absolute values of the electric field  $E$ ; and (c) optical emission intensity  $I$  of the 1st positive band of molecular nitrogen  $N_2$  at selected instants of time. Top panels show altitude scans at  $r = 0$ .

## 4.5 OPTICAL EMISSIONS

The emission intensity corresponding to the first positive band of  $N_2$  is shown in Figure 4.2c, and is significant only in regions where the electric field is above the threshold for optical excitation of this emission band of  $N_2$ . The significantly reduced electric field inside the ionized regions (Figure 4.2a) results in insignificant optical output. The optical emission region is rather wide (radial extent is  $\sim 20$  km) at  $t=2$  ms at  $\sim 70$  km altitude but subsequently becomes narrower ( $\sim 5$  km) at  $\sim 60$  km altitude at  $t=10$  ms, and expands downward at later times. Downward propagation slows down below  $\sim 50$  km altitudes (not shown) due to the exponential increase in electron loss at these altitudes. The average speed of downward propagation of the column in this case is  $\sim 10^3$  km/s.

The optical emissions shown in Figure 4.2c endure for times less than or comparable to the duration of one video frame (1/30 sec). For comparison with video observations, it is thus useful to average over  $\sim 30$  ms. Figure 4.3 shows the distribution of the intensity of the first positive band of  $N_2$  averaged over 32 ms for cases *a, b, c, d*, and *e*. Case *a* is similar to the cases of fast charge removal studied in the previous chapter of this dissertation. The increase of the electric field outside the conducting region in this case is compensated by the relatively high ambient conductivity, inhibiting the formation of an ionization channel. For case *c* the electric field reaches the ionization threshold  $E_k$  only at the very end of the charge removal at  $t \sim 10$  ms, so that we see the self driven development of an ionization channel propagating downward which tends to focus toward lower altitudes. For case *d*, the total amount of removed charge (475 C) is greater than for case *c* (400 C) so that the electric field exceeds  $E_k$  over a larger region and the corresponding structure of the optical emissions appears to be wider and does not show significant focusing toward lower altitudes. Case *e* shows structure consisting of two parts separated by a gap at  $\sim 67$  km altitude. This feature is consistent with the typical structure of sprites as a high altitude “plume” and adjacent lower altitude “dendritic” (forked) forms [e.g., Winckler *et al.*, 1996].

In case *b* we placed a “ball” of highly conducting plasma with radius  $\sim 5$  km and electron



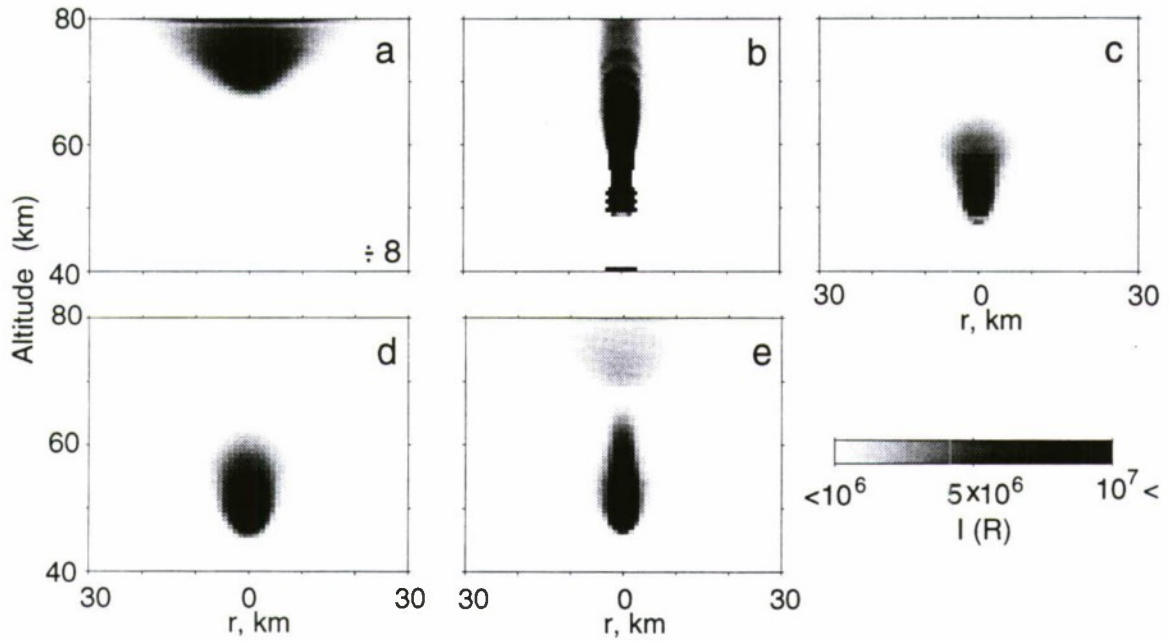


**Fig. 4.3. Time averaged optical emission intensity.** The distribution of time averaged optical emission intensity  $I$  (Rayleighs) of first positive band of  $N_2$  is shown on linear scale and for models of charge removal as illustrated in Figure 4.1. Note 1/8 scale modification for case *a*.

density  $N_e \sim 10^4 \text{ cm}^{-3}$  at 45 km altitude. This somewhat artificial initial condition is used to demonstrate how preexisting inhomogeneities of the ambient conductivity may dramatically modify the properties of the breakdown. The ionization channel is initiated in case *b* at  $\sim 50$  km altitude due to the enhanced conductivity and the associated electric field and propagates upward showing a slight expansion toward higher altitudes. The propagation speed is very high ( $\sim 10^4$  km/s) and is mostly defined by the almost simultaneous enhancement of the electric field above the characteristic breakdown field  $E_k$  in a region between the charge induced in the tip of the column and the upper conducting boundary assumed to be at 80 km.

#### 4.6 CURRENT AND CHARGE TRANSFER TO THE IONOSPHERE

The current which flows within the ionization channel is dominantly due to the electron component of conductivity. From Figure 4.2 the radius of the column can be estimated to be  $\sim 5$  km, and the electron density is  $\sim 10^{22} \text{ cm}^{-3}$ . The electron drift velocity in an electric field  $E$  comparable to the critical breakdown field  $E_k$  (Section 2.4.2) can be estimated as  $v_d = \mu_e E_k$ , where for  $E \sim E_k$   $\mu_e \simeq 4 \times 10^{-2} N_o/N \text{ m}^2/\text{V/s}$  (see equation (2.5)). The resultant value of the electron drift velocity is  $v_d \sim 10^5 \text{ m/s}$ , so that the current flowing within the ionization channel is  $\sim 100 \text{ A}$ . The total charge transfer to the ionosphere by this current on a time scale of  $\sim 30 \text{ ms}$  (roughly the duration of optical emissions) is  $\sim 3 \text{ C}$ . The optical emission, however, is not a direct indication of current flow in the ionization channel and most of the charge to the ionosphere is transferred on much longer time scales (hundreds of ms) well after the initial transient appearance of the optical emission. Since the electric field which appears at mesospheric altitudes following a cloud-to-ground lightning is mostly defined by the magnitude and altitude of the removed (monopole) charge and its image in the ground, it is expected that the total transfer of negative charge (for +CG discharge case) to the ionosphere is comparable with the amount of positive charge originally removed from the cloud. Physically, conduction currents flowing in the atmosphere and mesosphere after a +CG discharge tend to bring positive charge down from the ionosphere to compensate the postdischarge electric field. The amount of charge required to achieve this compensation is comparable to the charge removed from the thundercloud. It is illustrative to note in this context that a static charge placed in an inhomogeneous conducting medium generates around itself an integral amount of screening charge (with opposite sign) which is equal in magnitude to the originally placed charge. Ionization channels associated with sprites act as highly conducting wires connecting the ionosphere and lower atmospheric regions which contribute to faster compensation of the postdischarge electric fields. However, it should be stressed that the electric field can be relaxed simply due to the ambient atmospheric conductivity, and that the associated current flow from/to the ionosphere in case of +CG/-CG must normally accompany of every lightning discharge. This current is enhanced by

atmospheric ionization, and is accompanied by intense optical emissions known as sprites, only for the most intense discharges which transport hundreds of coulombs of charge from cloud-to-ground.

The conservation of current within the streamer as it propagates in the atmosphere requires focusing of the streamer propagating downward and expansion of the streamer propagating upward as is discussed in more detail in the next chapter (Section 5.3). The most probable physical process which may stop the focusing of a downward propagating ionization channel is diffusion. For example, the ambipolar diffusion of electrons may stop the focusing process as soon as the column has a cross section  $\leq 10^3 \text{ m}^2$  at  $\sim 50 \text{ km}$  and may lead to the splitting of the sprite into many small scale filaments. The splitting process cannot be properly modeled with our azimuthally symmetric model; nevertheless the model results are in reasonable agreement with the dynamics of the decay of luminosity which first starts at high altitudes (Figure 4.2c, top panel) as observed by *Rairden and Mende* [1995].

## 4.7 COMPARISON WITH OBSERVATIONS OF SPRITES

### 4.7.1 Comparison With Video Observations

Figure 4.4b shows the expected red and blue video response at  $t=20 \text{ ms}$  for case *e*, calculated using the procedure described in Section 3.5. The blue color becomes increasingly significant at lower altitudes, being only a factor of 2 below the red at  $\sim 50 \text{ km}$ . The range of the optical emission intensity ( $10^2$ - $10^3 \text{ kR}$ ) shown in Figure 4.4b is consistent with video observations [*Sentman et al.*, 1995].

The quenching altitude of the 1st positive band of  $N_2$  is  $\sim 53 \text{ km}$  and that of the 2nd positive band is  $\sim 30 \text{ km}$  [*Valance and Jones*, 1974, p. 119]. Additional calculations (see, for example, results for blue jets for altitude range 20-50 km, in the next chapter) indicate that blue can become the dominant color below  $\sim 40 \text{ km}$  due to the quenching effects combined with particular properties of video filters which generally overemphasize blue



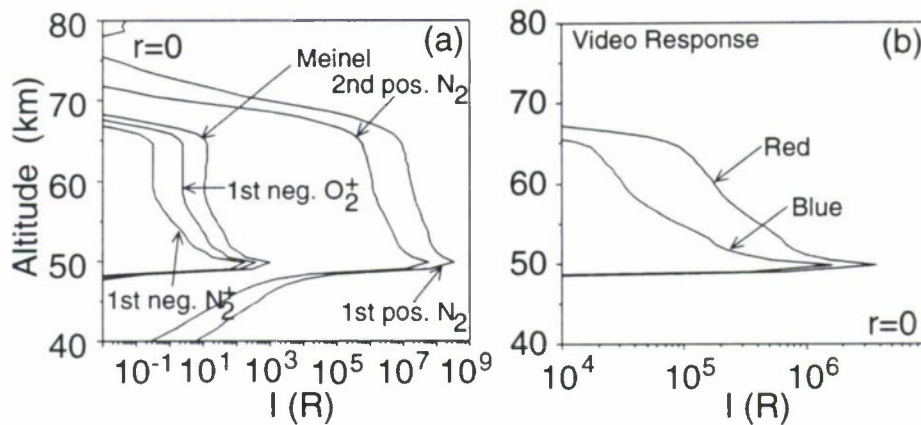


**Fig. 4.4. Optical emission intensity for selected bands and corresponding video response.** Altitude scans at ( $r=0$ ) of optical emission intensity  $I$  corresponding to different optical bands; (b) Expected red and blue video response corresponding to optical emissions shown in (a).

color (Section 3.5), in agreement with video observations of bluish lower altitude tendrils in most of sprites [Sentman *et al.*, 1995].

The variety of sprite shapes shown in Figure 4.3 are within the range of the measured transverse and horizontal sizes of sprites. However, the five cases shown in Figure 4.3 do not represent the complete diversity of shapes which have been experimentally documented or which can occur under different conditions. Model calculations (not shown) indicate that the transverse size of sprites can be very large (e.g.,  $\sim 50 \times 50$  km) depending primarily on the total amount of charge removed from the thundercloud (i.e., effective volume of space in which the post discharge electric field exceeds the characteristic breakdown field  $E_k$ ), the dynamics of charge removal, and the ambient conductivity profile. Localized conductivity enhancements (e.g., case *b*) which occur due to external sources (i.e., electron precipitation from the magnetosphere, meteors, runaway electrons, density perturbations left from a previous sprite, etc.) may significantly enhance the electric field and control the transverse scale of ionization channels and may lead to the creation of clusters of sprites by a single cloud-to-ground discharge. Under certain conditions, such preexisting enhancements of



conductivity may stimulate both upgoing (toward the ionosphere) and downgoing channels of ionization.

Video observations [Rairden and Mende, 1995] suggest the duration of sprites may be as large as  $\sim 40$  ms. On the other hand, photometric measurements of [Fukunishi *et al.*, 1995] suggest that the full-width-half-maximum duration is  $\sim 2$  ms. The longer persistence of the optical emissions observed in video may be due to the spectral response of a video camera in the near infrared region of the spectrum where the emission from the sprite might last longer in time than in the visible range [Winckler *et al.*, 1996], consistent with the fact that the threshold of excitation for the red emission ( $N_2$  1 st positive band) is lower. Another reason for the persistence of optical emissions might be connected with the flow of the current in the body of the ionization channel. The conduction current always exist in the body of the ionization channel as it propagates due to the finite electric field  $E \leq E_k$  (e.g., Figure 4.2b,  $t = 2, 10, 15, 20$  ms), and decays as soon as the channel stops (e.g., Figure 4.2b,  $t = 32$  ms). The observed persistence of the luminosity of sprites for several tens of ms [Rairden and Mende, 1995] might be a strong indication of the persistence of the electric field and the associated current flow in the body of the sprite (Section 4.6).

#### 4.7.2 Comparison With Photometric Observations

Figure 4.5 shows results of the spatially integrated optical emission intensity as a function of time  $t$  for the different cases of charge removal  $a, b, c, d$ , and  $e$  shown in Figure 4.1. The onset of the optical emission does not necessarily coincide with the onset of the causative cloud-to-ground discharge ( $t=0$ ) and can in fact be significantly delayed in time (up to  $\sim 20$  ms for case  $d$ ). This result is in agreement with photometric measurements by Winckler *et al.* [1996] who reported delays of  $\sim 3$  ms, and by Fukunishi *et al.* [1996] who reported delays ranging from several ms up to several tens of ms (see Section 1.2.7). Physically, this effect can be understood in terms of the threshold dependence on the electric field of the intensity of optical emission and ionization processes. Optical emissions appear nearly instantaneously in time when the corresponding threshold is reached. Results in Figure 4.5 for cases  $a$  and

*e* show that short pulses with  $\sim 3$  ms duration which immediately follow the causative cloud to ground discharge are created by the initial rapid removal of 200 C of charge in 1 ms. These few ms pulses are different than the shorter duration (few hundred  $\mu$ s) ionospheric flashes called “elves” which are likely to be produced by heating of the ambient electrons by electromagnetic pulses (EMPs) radiated by the discharge and are observed within a few hundred microseconds of the causative cloud-to-ground discharge [Fukunishi *et al.*, 1996; Inan *et al.*, 1996b]. As was discussed in Section 2.1, the EMP-induced interactions are not included in our quasi-static formulation.

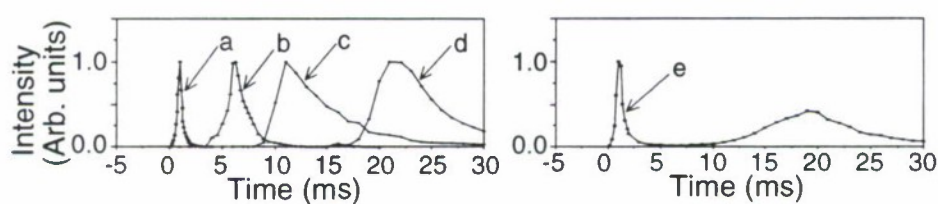


**Fig. 4.5. Spatially integrated optical emission intensity as a function of time.** Spatially integrated optical emission intensity of the first positive band of  $N_2 I$  as a function of time  $t$  corresponding to five models of thundercloud charge removal described in Figure 4.1.

### 4.7.3 Comparison With Spectroscopic Observations

The altitude distribution of emission intensities (at  $r=0$ ) corresponding to five different optical bands are shown in Figure 4.4a for case *e* and at  $t=20$  ms. The emission levels in these bands depend on the value of the electric field (i.e., the level of electron heating) and the electron density (ambient plus that produced due to ionization) and might be different for different altitudes and regimes of charge removal. However, our calculations show that under quasi-electrostatic heating conditions the Meinel band of  $N_2^+$  and 1st negative band of  $O_2^+$  are typically excited at intensities well below those of the ambient nighttime airglow ( $\sim 10^4$  R and  $\sim 10^2$  R, respectively [Chamberlain, 1978, pp. 214-218]). The first and

second positive bands of  $N_2$  and the 1st negative band of  $N_2^+$  have ambient levels of  $\sim 10^4$  R,  $\sim 5$  R, and  $\sim 5$  R, respectively [Chamberlain, 1978, pp. 214-218], and under different quasi-electrostatic heating conditions can be excited at levels well above the ambient levels.

Recent spectral measurements of sprites confirmed the dominant presence of the first positive band of  $N_2$  [Mende *et al.*, 1995; Hampton *et al.*, 1996]. Most of the energy of the second positive band of  $N_2$  is concentrated in the wavelength region of  $\sim 300$ -400 nm [Vallance Jones, 1974, Table 4.11, p. 131] (see also Figure 3.7) which is below the spectral range resolved in Mende *et al.* [1995] (450-800 nm) and Hampton *et al.* [1996] (540-840 nm) measurements, consistent with the fact that this band was not detected. As was discussed in Section 1.2.8, with the available signal-to-noise ratio of the measurements of Mende *et al.* [1995] and Hampton *et al.* [1996], in order to be detectable other spectral bands would have had to be at levels no less than a factor of ten of that of the  $N_2$  first positive band. In accordance with our model results, the intensities of the Meinel and 1st negative bands of  $N_2^+$  and the 1st negative band of  $O_2^+$  are generally produced at levels several orders of magnitude lower, also fully consistent with the fact that these bands were not detected by Mende *et al.* [1995] and Hampton *et al.* [1996].

#### 4.8 SPRITES AND RUNAWAY ELECTRONS

The possible role of runaway electrons in producing X-rays that are sometimes observed prior to lightning discharges and in the initiation of the lightning discharge itself was considered by McCarthy and Parks [1992], Gurevich *et al.* [1992, 1994] and Roussel-Dupre *et al.* [1994] (see also references cited therein), who showed that secondary cosmic ray electrons of energy  $\sim 1$  MeV can become runaways whenever the local electric field  $E$  exceeds the threshold field  $E_t = (4\pi N_m Z q_e^3 a)/(mc^2)$ , where  $N_m$  is the number density of air molecules,  $Z \simeq 14.5$ ,  $a \simeq 11$ ,  $m$  is the electron rest mass, and  $c$  is the velocity of light [Gurevich *et al.*, 1994].

Bell *et al.* [1995] considered the effects of an upward traveling beam of  $\sim 1$  MeV runaway



electrons accelerated by large quasi-electrostatic fields above thunderclouds as a possible mechanism for production of sprites. The main energy loss for the runaway electrons occurs from inelastic collisions with  $O_2$  and  $N_2$  molecules, resulting in optical excitation of the neutrals, and subsequent optical emissions. Results of a one-dimensional model suggest that the runaway electrons can produce optical emissions similar in intensity and spectra to those observed in sprites, but only for large quasi-electrostatic fields produced by positive cloud-to-ground discharges lowering 250 C or more to ground from an altitude of at least 10 km. In general, the threshold runaway field  $E_t$  is  $\sim 10$  times lower than the threshold field of the conventional breakdown  $E_k$  (see Section 2.4.2) and on this basis alone we might expect the runaway mechanism to proceed at lower quasi-electrostatic field levels [Taranenko and Roussel-Dupre, 1996]. However, in the lower atmosphere, the runaway avalanche breakdown process starts from very low ambient production rates, requiring many e-folding distances before observable effects can be produced [Bell *et al.*, 1995]. As a result, production of significant optical emission levels via the runaway mechanism requires charge transfers similar to quasi-electrostatic heating mechanism [Bell *et al.*, 1995].

Figure 4.6a from [Bell *et al.*, 1995] shows the optical intensity per unit volume of the 1st positive band of  $N_2$  produced by the runaway breakdown process. The five curves shown correspond to specific values of the total charge  $Q$  removed from a thundercloud at 10 km altitude in 1 ms and indicate that the optical output sensitively depends on the removed charge value. The same result holds for all the other excited bands, not shown here for the sake of brevity.

Figure 4.6b shows the optical intensity per unit volume of the 1st and 2nd positive bands of  $N_2$ , the Meinel and 1st negative bands of  $N_2^+$ , and the 1st negative band of  $O_2^+$  produced by runaway electrons accelerated by quasi-electrostatic thundercloud fields for  $Q = 275$  C [Bell *et al.*, 1995]. The two positive bands of  $N_2$  dominate the spectrum up to  $\sim 80$  km, above which the Meinel band of  $N_2^+$  also becomes important. Video observations indicate that the brightest region of a sprite lies between 66 and 74 km and that some sprites exhibit significant intensity at altitudes as low as 40-50 km [e.g., Sentman *et al.*, 1995]. As shown



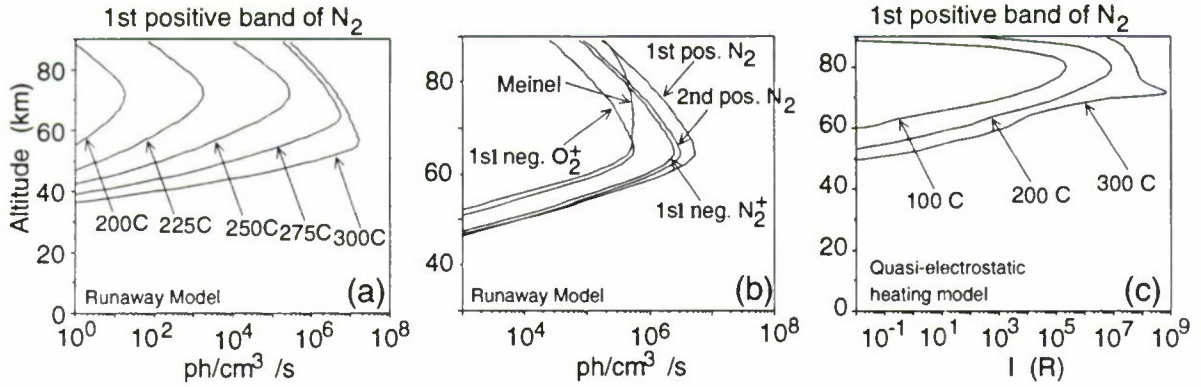


**Fig. 4.6. Optical emissions produced by runaway electrons.** (a) The volume emission rate (in photons  $\text{cm}^{-3} \text{s}^{-1}$ ) profile of the 1st positive band of  $\text{N}_2$  for selected thundercloud charge values, and (b) the volume emission rate of selected bands for  $\text{N}_2$ ,  $\text{N}_2^+$  and  $\text{O}_2^+$  for a thundercloud charge of 275 C, obtained from runaway electron model; (c) The optical emission intensity (in Rayleighs) profiles of the first positive band of  $\text{N}_2$  obtained from quasi-electrostatic heating model for different thundercloud charge values. For a typical  $\sim 10$  km ( $\sim 10^6$  cm) diameter of a sprite the horizontal scale in (a) and (b) can be interpreted as the intensity in Rayleigh (see (2.11)). Figure is reproduced from [Bell *et al.*, 1995].

in Figure 4.6, the optical emission intensities produced by the runaway breakdown process tend to peak in the 55-70 km altitude range, and substantial intensity can be found at altitudes as low as 45 km.

Figure 4.6c shows the intensity of the first positive band of  $\text{N}_2$  produced by the quasi-electrostatic heating mechanism for different values of the thundercloud charge  $Q$  removed from 10 km altitude in 1 ms. These simulation conditions are identical to those used to obtain results of the runaway model shown in Figure 4.6a. Two important features are apparent: Firstly, the runaway process produces optical emissions which span a wider range of altitudes than those produced by the quasi-electrostatic heating; Secondly, the emission intensities generated in the runaway process sensitively depends on the removed thundercloud charge value and become negligible for charges  $Q < 250$  C.

Bell *et al.* [1995] recognized two other notable differences between the runaway breakdown and quasi-electrostatic heating model: i) the ratio  $R_{12}$  of the intensity of the 1st positive band of  $\text{N}_2$  to the 2nd positive band of  $\text{N}_2$  is  $\sim 2$  at all altitudes above 60 km for the runaway model, while for the quasi-electrostatic heating model  $R_{12} \simeq 10$  above 80 km

altitude (see Figures 3.9b and 4.4a); and ii) in the runaway model the intensity of the Meinel band of  $N_2^+$  and the 2nd positive band of  $N_2$  are roughly equal at 80 km altitude, while for the quasi-electrostatic heating mechanism the intensity of the Meinel band of  $N_2^+$  is smaller than that of the 2nd positive band of  $N_2$  by a factor of  $\sim 10^3$  (see Figure 3.9b). As a result of these differences, *Bell et al.* [1995] suggested that spectral analysis of sprites may delineate the conditions under which the two different generation mechanisms are operative. For example, altitude profiles of spectral ratios could determine the regions dominated by each mechanism.

As a discussion point and a subject for future studies it is important to realize that the temporal behavior of the runaway electrons may significantly complicate the interpretation of spectral measurements of sprites (see Section 1.2.8). For example, impulsive (e.g.,  $< 1$  ms) production of a large number of energetic secondary electrons would lead to the rapid cooling of these electrons (e.g., for times  $> 1$  ms). Since the electric field values required for the runaway process are comparable with those for conventional quasi-electrostatic heating these cooled electrons might remain at a heated level defined by the quasi-electrostatically heated electron distribution, instead of the energetic distribution initially created by the runaway beam. The recent report of *Winckler et al.* [1996] that sprites begin with an intense, wideband flash covering both the blue and red portions of the spectrum, with a fast decaying blue portion (see Section 1.2.7 for more details), may indicate the presence of a cooling process in which initially energetic secondary electrons produced by a runaway beam are cooled to the energy level of conventional heating as described above.

Although in the stationary case the secondary electron distribution produced by runaway electrons and the resultant complexity of optical emissions are similar to that created by energetic precipitating particles in aurora (see Appendix B ) we note that in view of our previous arguments the impulsive nature of the runaway process may lead to a highly variable (on a time scale of  $\sim 1$  ms) spectral content. This subject requires further investigation (see Section 6.2).



# 5

## Blue Jets Produced by Pre-Discharge Thundercloud Fields

In this chapter we show that, under certain conditions, pre-discharge quasi-electrostatic thundercloud fields immediately above the thundercloud can lead to the formation and upward propagation of streamer type ionization channels with features in good agreement with recent video observations of blue jets.

### 5.1 PHYSICAL MECHANISM

We propose that blue jets are also associated with streamer type processes occurring on an atmospheric spatial scale. The difference between sprites and jets in the framework of our quasi-electrostatic heating model can be understood as follows:

Sprites are relatively fast processes (time scale  $\sim 1-10$  ms) occurring at mesospheric altitudes due to the impulsive appearance of large quasi-electrostatic fields following cloud-to-ground lightning discharges. The time scale of sprites and their energetics are thus closely associated with properties of the causative cloud-to-ground discharge. Ionization regions associated with sprites enhance atmospheric conductivity and serve as additional factors leading to more rapid relaxation of the post-discharge electric fields. Jets are much slower processes (time scale  $\sim 300$  ms) which are not associated with cloud-to-ground lightning discharges and can be initiated near the thundercloud tops in cases of slow accumulation



of large amounts of charge at altitudes  $\sim 20$  km. The upward propagation of jets can only be sustained if thundercloud acts as a “battery” which is energetic enough to continuously compensate lost of thundercloud charge due to ionization and conduction current associated with jet. Slower time scales of jets thus are mostly controlled by the dynamics of charge separation processes inside the cloud.

### 5.1.1 Blue Jets as Streamers

As was already discussed in the previous Chapter, streamers can be defined in general terms as transient filamentary plasmas, the dynamics of which are controlled by highly localized nonlinear space charge waves [see *Vitello et al.*, 1994; *Grange et al.*, 1995; *Lagarkov and Rutkevich*, 1994, and references therein]. The morphology of streamers is very complex even for the simplest geometries [e.g., *Vitello et al.*, 1994]. However, a series of rigorous numerical simulations [*Dhali and Williams*, 1987; *Vitello et al.*, 1994] has revealed several robust features of streamers which are discussed below in terms of their application to blue jets. The streamer velocity  $v_s$  usually lies in the range  $\sim 10^2$ - $10^3$  km/s depending on the streamer polarity, the applied electric field ( $E$ ), the initial radius, the density of the seed ionization which initiates the streamer process, the background electron density [e.g., *Dhali and Williams*, 1987], and the geometry of the boundaries (e.g., point to plane corona discharge) [*Grange et al.*, 1995]. The polarity of a streamer is defined by the sign of the space charge induced in its “head”. A negative streamer propagates due to ejection of electrons from its head. Positive streamers require a population of ambient electrons (e.g., produced by cosmic rays) for their development, have relatively low velocities of  $\sim 100$  km/s, comparable to electron drift velocities ( $v_d$ ) in the body of the streamer, and occur for low applied electric fields [*Dhali and Williams*, 1987] and in point-to-plane corona discharges [e.g., *Grange et al.*, 1995]. The minimum propagation velocity of the positive streamers is equal to 100 km/sec in air [e.g., *Petrov et al.*, 1994]. The streamer velocity generally depends on the steepness of the applied voltage pulse in time, remains  $\sim 100$  km/s

for relatively low voltage rise rates ( $< 50 \text{ kV}/\mu\text{s}$ ) but becomes larger for rise rates  $> 50 \text{ kV}/\mu\text{s}$  [e.g., *Petrov et al.*, 1994].

Assuming that the radius  $r_s$  of the streamer column is approximately equal to that of its head, the streamer velocity  $v_s$ , its radius  $r_s$  and the dielectric relaxation time  $\tau_s$  within the streamer ( $\tau_s = \epsilon_0/\sigma_s$ , where  $\sigma_s$  is the streamer conductivity) are related simply by [*Vitello et al.*, 1994]:

$$\frac{\delta}{r_s} = \frac{v_s \tau_s}{r_s} \simeq \frac{E_b}{E_h} \quad (5.1)$$

where  $E_h$ ,  $E_b$  are the electric fields at the streamer head and in the streamer body, respectively, and  $\delta = v_s \tau_s$  is an effective “skin depth” for the electric field inside the streamer. In most cases  $0.1 < E_b/E_h < 1$  so that  $\delta$  is comparable to the streamer radius  $r_s$  [*Lagarkov and Rutkevich*, 1994, p.16]. Since diffusion effects do not appear to play a significant role in the formation of the streamer [*Dhali and Williams*, 1987; *Vitello et al.*, 1994], the effective skin depth  $\delta$  is the only parameter which characterizes the spatial scale of the streamer. On this basis, we suggest that streamer type solutions are possible for a variety of transverse dimensions, including the kilometer spatial scales typical for blue jets, provided that the appropriate initial conditions can occur near the top of the thundercloud. In this context, blue jets are similar to previously studied positive streamers which initiate point-to-plane corona discharges in laboratory experiments [e.g., *Grange et al.*, 1995], except for the differences in the electric field production, geometry and maintenance of the field by the thundercloud charge distribution, and the altitude variation of atmospheric neutral density and conductivity.

### 5.1.2 Formation of Blue Jets

The positive (top) and the negative (bottom) thundercloud charges (Figure 5.1) slowly (seconds) accumulate due to the current  $\vec{J}'_s$  (see Section 2.1) associated with the separation of charges inside the cloud, and directed opposite to the resulting electric field. The current may be related to the small and light positively charged ice splinters driven by updrafts, and

heavy negatively charged hail particles driven downward by gravity [e.g., *Uman*, 1987, p. 65]. Unusually intense hail activity was indeed observed in association with jets [*Wescott et al.*, 1995b; 1996], and is a strong indication of intense electrical activity inside the cloud.

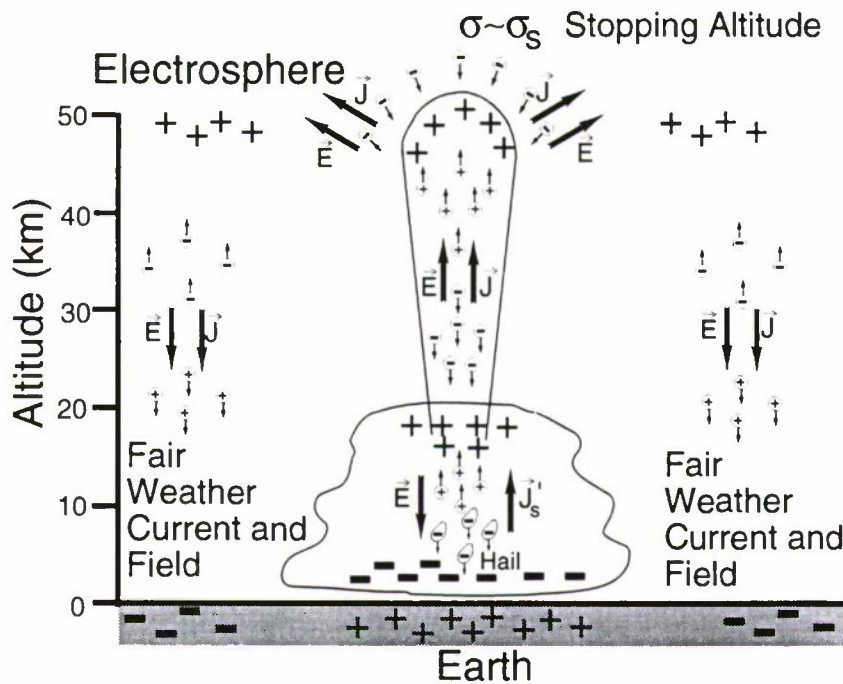


**Fig. 5.1. Mechanism of Blue Jets.** Currents, charges and electric fields associated with the blue jet. The Figure is partly adapted from [*Uman*, 1987, p. 30].

Under certain relatively rare conditions, a charge of  $Q=300\text{--}400$  C can accumulate in thunderclouds at  $\sim 20$  km altitude. This charge may have an extended dish-like distribution and can lead to breakdown ionization in regions with lateral extent  $\sim 10^2\text{--}10^3$  m. The ionization may also be connected with the accumulation of long lived ( $\sim 1\text{--}2$  sec at  $\sim 20$  km [*Lowke*, 1992]) metastable  $O_2$  molecules due to upward directed discharges preceding the development of jets [*Wescott et al.*, 1995a], corona discharges initiated by hydrometeors [*Griffiths and Phelps*, 1976] or highly charged hailstones triggering instability of charged droplets [*Grigor'ev and Shiryayeva*, 1989]. Once formed, the ionized region can act as



the seed for the development of an upward propagating positive streamer. We propose that jets are the mesospheric analog of the positive type streamers produced in laboratory point-to-plane corona discharge experiments.

The electric field is non zero inside the streamer as it propagates and an upward directed current ( $I_s$ ) always flows in the streamer body (Figure 5.1). The streamer propagates freely when the current  $I_s$  is maintained by a source in or near the cloud. Otherwise, the negative charge flowing within the streamer body towards the positive thundercloud charge would reduce the source charge and the electric field and would eventually suppress the propagation of the streamer. Thus, the streamer can propagate as long as the source current  $\vec{J}'_s$  can deliver sufficient positive charge to the top of the thundercloud. An equal amount of negative charge is accumulated at the thundercloud base so that the overall charge in the cloud-streamer system is conserved. The thundercloud thus plays the role of a “battery” and the net effect of the streamer attached to this “battery” is to deliver positive charge to the conducting electrosphere, contributing to the maintenance of the fair weather potential. The streamer propagation can also cease when it reaches the critical altitude at which the dielectric relaxation time  $\tau_s$  within the streamer body is comparable to the relaxation time  $\tau$  of the ambient conducting atmosphere ( $\tau = \epsilon_0/\sigma$ ). At this altitude, all of the current flowing through the channel created by the streamer can be supplied by the flow of atmospheric ions, and the electric field at the tip of the streamer is not enhanced since the ambient conductivity  $\sigma$  is comparable to the conductivity  $\sigma_s$  inside the streamer head.

## 5.2 MODEL PARAMETERS

For calculations in this Chapter we use the ambient electron density profile 1 shown in Figure 2.4a and the ion conductivity profile A illustrated in Figure 2.4b.

In our model, the effective source current  $\vec{J}'_s$  (see Figure 5.1 and discussion in Section 2.1) is introduced in such a way as to compensate any changes in the thundercloud charge  $\rho_s$  due to the conduction losses (which in the case of blue jets also include the current flow and



associated charge accumulation due to the streamer attached to the top of the cloud). As discussed in Section 2.1 the introduction of  $\vec{J}'_s$  allows us to separately specify the charge dynamics inside of the cloud as a given function of time.

We assume that a positive thundercloud charge is located at 20 km altitude, has a spherically symmetric Gaussian distribution with a spatial scale of  $a=3$  km, builds up over a time scale  $\tau_f$ , and is dissipated over a time of  $\tau_d$ . This positive charge is presumed to be accompanied by negative charge at lower altitudes, as shown in Figure 5.1. In determining the dynamics of the resulting blue jet, we neglect the effects of the lower thundercloud charge due to its proximity to the ground. This negative charge may in fact also be removed by a series of negative lightning discharges which sometimes are observed several seconds before the appearance of blue jets [Wescott *et al.*, 1995b; 1996].

Equations (2.2) and (2.3) which are used for the calculations of the electric field and charge density are contained in the more general two-fluid streamer equations [e.g., Vitello *et al.*, 1994]. In comparison, equation (2.3) does not contain a term describing exponential growth of the electron density due to ionization processes (see, for example, equation (2.9) in Section 2.4.4). The increase in the electron density  $N_e$  is self-consistently included in our model through changes in conductivity  $\sigma$ . However, since for typical parameters used we have  $v_d \sim v_s$ , our formulation cannot be used to accurately determine the small scale details of the electron number density  $N_e$  near the steep boundary at the streamer head. Results of extensive modeling [e.g., Vitello *et al.*, 1994] indicate that for a well developed streamer, the relaxation time  $\tau_s$  behind the streamer front remains approximately constant. We use this result as an additional external condition in our model, placing a bound on the growth of the electron density  $N_e$  in the streamer front.

A characteristic breakdown electric field  $E_k^0 = 3.7 \times 10^6 N/N_o$  V/m ( $N_o = 2.688 \times 10^{25} \text{ m}^{-3}$ ) is defined for calculations in this chapter as the field at which the effective ionization coefficient  $\nu_i$  is equal to the attachment coefficient  $\nu_a$  (see Figure 2.6),  $\sim 15\%$  larger than the

characteristic air breakdown value  $E_k = 3.2 \times 10^6 N/N_o$  V/m defined by *Papadopoulos et al.* [1993] and used in sprite ionization column calculations reported in the previous chapter.

For electric fields  $E > E_k^o$ , the electron density  $N_e$  grows exponentially in time with a rate  $(\nu_i - \nu_a) > 0$  determined as a function of the electric field by the equations (2.6) and (2.7). For electric fields  $E < E_k^o$  (i.e.,  $(\nu_i - \nu_a) < 0$  as is the case just behind the streamer front) electrons may be quickly removed by dissociative attachment to  $O_2$ . However, such may not always be the case due to the extremely effective detachment process of electrons in the presence of metastable  $O_2$  [Lowke, 1992], leading to a reduction of the breakdown field  $E_k$  by factor of about 6, in some cases. As already discussed in Section 2.4.3, the role of dissociative attachment of electrons to  $O_2$  is difficult to assess since the measured rates for associative detachment and for collisional detachment are known only within one to three orders of magnitude, respectively [Davies, 1983]. In view of the complexity of the role of detachment, we conservatively assume for calculations in this chapter that  $(\nu_i - \nu_a) = 0$  for electric fields  $E < E_k^o$ . In addition to the above arguments, the more conservative threshold level of  $E_k^o$  (i.e.,  $3.7 \times 10^6 N/N_o$  instead of  $3.2 \times 10^6 N/N_o$ ) is used here for blue jets calculations in view of the sensitive dependence of the optical excitation coefficients on the electric field at low values of  $E$ . The chosen value of  $E_k^o$  places the optical emission production at electric field levels where the ratio of the excitation coefficients of the 1st and 2nd positive bands of  $N_2$  is  $\sim 10$  rather than several orders of magnitude (Figure 2.7).

Model calculations indicate that the streamer morphology above a thundercloud can be complex, exhibiting large variability in lateral extent  $r_s$ , stopping altitude and vertical velocity of propagation  $v_s$ , depending mostly on the initial conditions and the source function (e.g., the current  $\vec{J}'_s$ ). Such variability is in general agreement with the degrees of freedom allowed for streamer solutions in equation (5.1) and with recent observations of a new phenomenon known as "blue starters" [Wescott et al., 1995b; 1996], which exhibit shorter lifetimes, wider range of velocity variations ( $\sim 27$ -157 km/s) and smaller transverse and vertical extents in comparison with jets [Wescott et al., 1995a; 1996].

We assume  $\tau_f=1$  sec and  $\tau_d=0.5$  sec, and consider  $\tau_s$  as an input parameter. The initial ionization region and the initial radius of the jet  $r_s$  are then defined mostly by the effective volume of space over which the electric field  $E$  exceeds  $E_k^0$ , depending on the magnitude and distribution of the thundercloud charge  $Q$ . The initial ionization that forms naturally above the thundercloud plays the same role as the seed ionization in streamer simulations [e.g., Vitello *et al.*, 1994].

Our model results indicate that the dependence of the streamer characteristics on  $\tau_s$  and  $Q$  are in agreement with (5.1). The model solutions are very sensitive to initial conditions and demonstrate large variability in possible outputs. This sensitive dependence makes it difficult to identify a physical mechanism which automatically and selfconsistently selects initial conditions characteristic for blue jets. It is important to stress, however, that when we select the “correct” initial conditions, model calculations reproduce the selfconsistent development of the streamer and demonstrates agreement with almost every observed feature of blue jets. Such a case showing agreement with the observed characteristics of jets [Wescott *et al.*, 1995a] is described in the following section.

### 5.3 ELECTRON NUMBER DENSITY, ELECTRIC FIELD AND CURRENT

Figure 5.2 shows the electric field and the electron number density  $N_e$  corresponding to a jet produced by a thundercloud charge  $Q = 375$  C assuming  $\tau_s=0.05$  sec. Altitude scans of the electric field (at  $r=0$ ) are shown in the left hand panel at selected instants of time, and in comparison with  $E_k$ . The enhancement of the electric field at the tip of the streamer is apparent in the middle panel of the Figure 5.2a. The characteristic spatial scale  $\delta$  is comparable with  $r_s$ . The electric field barely exceeds  $E_k$ , since the ionization coefficient  $\nu_i$  becomes very large ( $\nu_i \gg \tau_s^{-1}$ ) for slight increases in the electric field above  $E_k$ . Accordingly, it can be assumed that  $E_b \simeq E_h$  in (5.1). The electron number density  $N_e$  shown in the right hand panel illustrates the formation of a beam-like distribution expanding upward with a radius  $\sim 2$  km at the cloud top and  $\sim 7$  km at  $\sim 45$  km altitude.



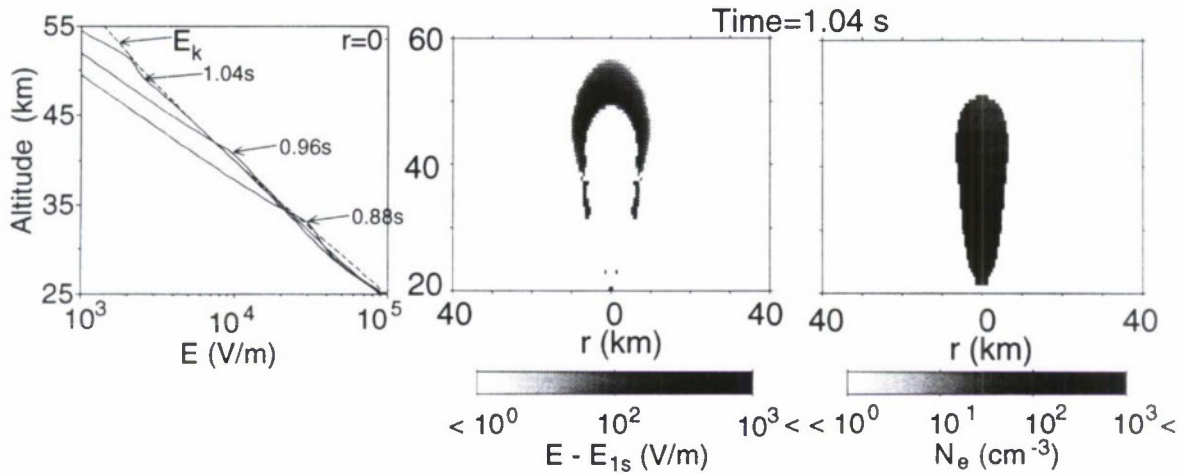


**Fig. 5.2. Electric field and electron density associated with a blue jet.** A crosssectional view of the distribution of the absolute values of the electric field  $E$  and the electron density  $N_e$  at selected instants of time. Right hand panel shows altitude scans at  $r=0$ .

The results of the numerical model can be qualitatively interpreted based on simple analytical estimates. Behind the front of the jet the electric field  $E \simeq E_k$  (Figure 5.2a), so that a current  $I_s \simeq q_e N_e v_d \pi r_s^2$  flows in the streamer body where  $q_e$  is the electronic charge, and  $v_d = \mu_e E_k$ . This current  $I_s$  is estimated to be  $\sim 200$  A, and can deliver  $\sim 100$  C to the thundercloud during the lifetime of the jet. The electron mobility  $\mu_e$  for  $E \simeq E_k$  is  $\mu_e \simeq 4 \times 10^{-2} N_o / N$  (see equation (2.5)), so that the electron drift velocity  $v_d \simeq 100$  km/s, independent of altitude. The current  $I_s$  is conserved along the jet. Since  $v_d$  is constant, the conservation of  $I_s$  implies that the quantity  $N_e r_s^2$  should also be conserved. In our model, we assume  $\tau_s = \epsilon_o / \sigma_s$  to be constant, where the conductivity in the streamer body  $\sigma_s = q_e N_e \mu_e$ , which is equivalent to requiring  $N_e \simeq N$ . The conservation of streamer current  $I_s$  thus implies that  $r_s \sim N^{-1/2}$ , consistent with the general tendency of the jet to expand toward higher altitudes, in good agreement with our numerical results, especially below 40 km. Above 40 km, the expansion slows down because of the increasing role of ionospheric ions in carrying the streamer current, as well as the reduction in the source charge  $Q$  (so that the current  $I_s$  is reduced in later stages of streamer propagation). A comparison of



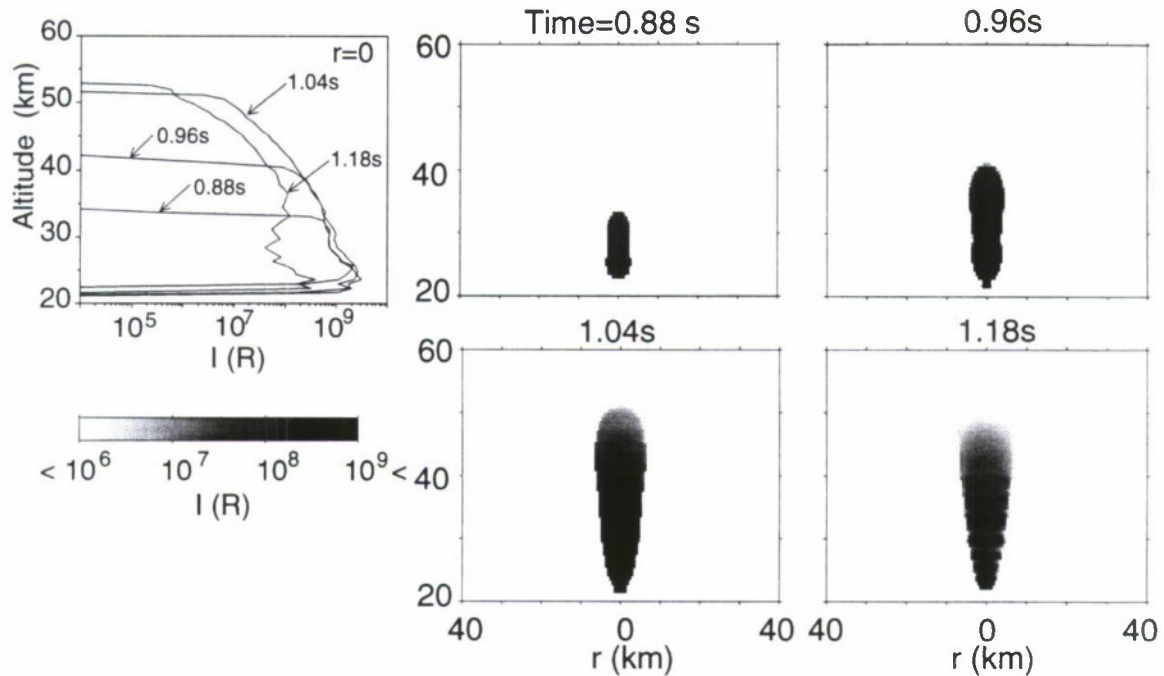
the conditions  $\tau_s = \text{const}$  and  $r_s \sim N^{-\frac{1}{2}}$  with equation (5.1) shows that  $v_s \sim N^{-\frac{1}{2}}$ , in good agreement with our numerical results. At the initial stage of the jet formation at 24 km altitude we have  $v_s \sim 40$  km/s; the streamer speed subsequently reaches  $\sim 100$  km/s at  $\sim 35$  km altitude and remains in the range 100-130 km/s until the jet stops. The numerical values of the electron density and streamer radii at 24 km and 35 km are  $10^3$  and  $180 \text{ cm}^{-3}$  and 2 and 5 km, respectively. These values are reasonably consistent with the conservation of the current  $I_s$  and the condition (5.1).

## 5.4 OPTICAL EMISSIONS

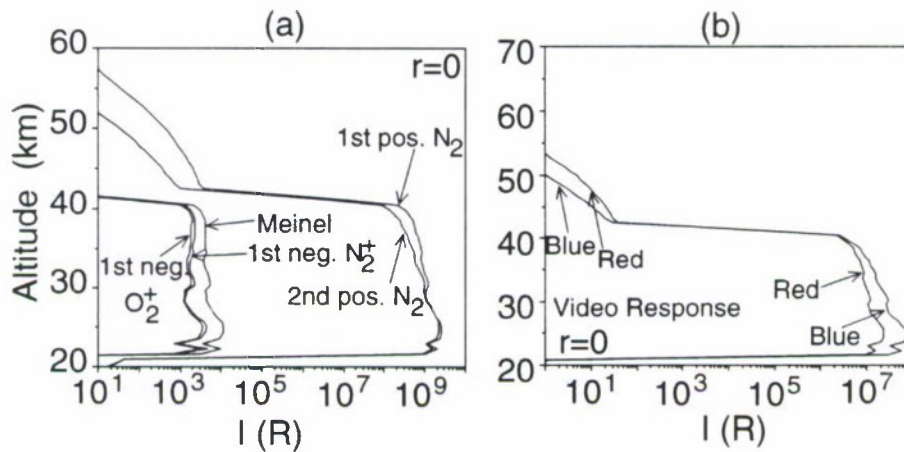
The optical emission intensity of the second positive band of  $\text{N}_2$  is shown in Figure 5.3. The jet propagates upward with an average velocity of 88 km/s and stops at  $\sim 50$  km altitude mainly due to our chosen temporal variation of the source thundercloud charge  $Q(t)$  with decay time  $\tau_d = 0.5$  sec. If the charge  $Q$  is instead kept constant after 1 sec, the jet propagates to a slightly higher altitude ( $\sim 53$  km) and stops when  $\tau_s \simeq \varepsilon/\sigma$ , which for the ion conductivity profile used occurs at 49 km altitude. The optical emission has the shape of an upward expanding beam with transverse dimensions being essentially the same as the ionization column shown in Figure 5.3. The corresponding cone angle is  $\sim 20^\circ$ . Figure 5.3 shows that the optical emission intensity fades away at  $t = 1.18$  sec simultaneously at all points along the jet.

Figure 5.4a shows the altitude distribution of the optical emission intensity at the axis of symmetry ( $r = 0$ ) for selected bands at  $t = 1.04$  sec. The first and second positive bands of  $\text{N}_2$  dominate and have similar intensities. Figure 5.4b shows the red and blue video responses at  $t = 1.04$  sec.

Figure 5.5 shows the spatially integrated value of the optical emission intensity as a function of time. The intensity peaks  $\sim 200$  ms after the start of the jet and disappears over  $\sim 150$ -200 ms, defined primarily by the chosen value of  $\tau_d$ . Additional calculations (not shown) indicate that the jet can last as long as the thundercloud charge can support the flow



**Fig. 5.3. Optical emission intensity associated with a blue jet.** A cross-sectional view of the distribution of optical emission intensity of the first positive band of  $N_2$  at selected instants of time. Right hand panel shows altitude scans at  $r=0$ .



**Fig. 5.4. Optical emission intensity for different optical bands.** (a) Altitude scans at ( $r=0$ ) of optical emission intensity  $I$  corresponding to different optical bands; (b) Expected red and blue video response corresponding to optical emissions shown in (a).

of current from the cloud to the ionosphere. In this case, the jet is stationary and has the shape of a significantly expanded upward luminous column which electrically connects the thundercloud and the higher conducting regions of the atmosphere.

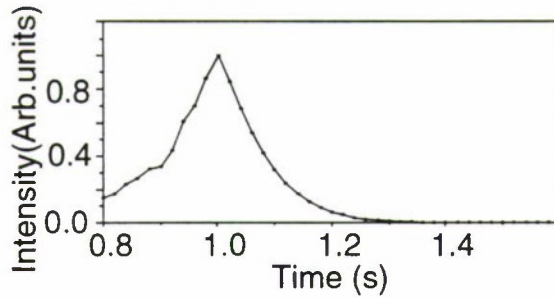


Fig. 5.5. Spatially integrated optical emission intensity as a function of time.

## 5.5 COMPARISON WITH VIDEO OBSERVATIONS OF BLUE JETS

### 5.5.1 Geometrical Shape and Velocity of Blue Jets

The dynamics of the source charge  $Q$  may play a dominant role in defining the radial extent  $r_s$  and velocity  $v_s$  of jets. Equation (5.1) and the continuity of the streamer current  $I_s$  indicate that the velocity  $v_s$  can stay constant with altitude if  $r_s \sim N^{-1}$  and  $N_e \sim N^2$ . The initial radii of jets in such a case should be very small (100-500 m) to produce the observed collimated (with cone angle  $< 30^\circ$ ) beam-like shape of the lower parts of jets with altitude extent of several atmospheric scales. Such a result may be consistent with the fan-like upper parts of blue jets [Wescott *et al.*, 1995a] (see also lower image in Figure 1.12); however, the optical emission intensity ( $I \sim N_e$ ) in this case dramatically decreases with altitude with a scale height of  $\sim 3$  km.

### 5.5.2 Brightness and Color of Blue Jets

Figure 5.4b indicates that the optical emission intensity changes by a factor of  $\sim 10^2$  between the lower and upper ends of the jet, in good agreement with observations [Wescott *et al.*, 1995a]. However, the predicted absolute intensities  $\sim 5 \times 10^4$  kR (Figure 5.4b) are  $\sim 1$ -2 orders of magnitude above those observed ( $\sim 10^3$  kR [E. Wescott, private communication]). In this regard, we note that the excitation rates of the optical emissions depend sensitively on the electric field (e.g.,  $E_k^0$ ) and may change several orders of magnitude in response to small

variations in the electric field. In addition, the uncertain role of detachment processes (as discussed in previous sections) may have lead to an overestimation of the optical emission intensities.

Concerning the relation between red and blue colors we note that the distribution as a function of wavelength of the first and second positive bands of  $N_2$  may significantly differ at low altitudes from that observed in aurora at ionospheric altitudes and used in our calculations of the red/blue video response for measurements of sprites in Figure 5.4b. For example, the  $\Delta v=3,4$  sequences of the first positive band of  $N_2$ , producing red visible emissions, may be significantly degraded in comparison with that shown in Figure 5.4b due to a reduction in the populations of high vibrational levels with increasing pressure [e.g., *Morrill et al.*, 1988]. Since the first and second positive bands are the only significant emissions (Figure 5.4a) the second positive band is the most probable source of the blue color of jets.

## 5.6 BLUE JETS AND RUNAWAY ELECTRONS

In the context of blue jets, runaway electrons may possibly be involved in producing the initial ionization in the streamer head. As was previously discussed, the runaway breakdown mechanism appears attractive since it has a threshold field  $E_t$  which is  $\sim 10$  times lower than the conventional breakdown field  $E_k$ . However, in the lower atmosphere, the runaway electron process starts from very low ambient production rates of energetic electrons produced by cosmic rays ( $S_0$ ), requiring many e-folding distances before observable effects can be produced [*Bell et al.*, 1995]. As a result, the electric field should in fact significantly exceed ( $>5$  times) the threshold field  $E_t$  in order to reach a regime of significant ionization and optical output.

To elaborate further, consider the case  $E = 7E_t$  and two different altitudes of 30 and 40 km. Runaway electron e-folding distances for these altitudes are  $l_f \sim 50$  m and  $\sim 200$  m, respectively [*Bell et al.*, 1995]. To support a streamer with  $\tau_s=0.05$  s and  $r_s=2$  km, the



runaway process should produce sufficient secondary electrons (e.g.,  $N_s \simeq 10^3 \text{ cm}^{-3}$ ; see Figure 5.2) on a time scale much shorter than  $\tau_s$ , say  $\Delta t \simeq 1 \text{ ms}$ . Using  $N_s \simeq cN_R N \sigma_o \Delta t$ , where  $c$  is speed of light,  $\sigma_o = 2.3 \times 10^{-18} \text{ cm}^2$  [Bell *et al.*, 1995] the required number of runaway electrons can be estimated as  $N_R \simeq 3.9 \times 10^{-5}$  and  $1.8 \times 10^{-4} \text{ cm}^{-3}$  at altitudes 30 and 40 km, respectively. The number of required e-foldings  $n_f$  can be estimated from  $N_R \simeq S_o l_f / c e^{n_f}$ , and is equal to 20.1 and 21.6 for 30 and 40 km, respectively, where  $S_o = 4.4 \times 10^{-7} \text{ cm}^{-3} \text{ s}^{-1}$ , at 30 km and  $S_o = 10^{-7} \text{ cm}^{-3} \text{ s}^{-1}$  at 40 km [Bell *et al.*, 1995]. Thus, runaway electrons should move at least  $\sim 1 \text{ km}$  at 30 km and  $\sim 4 \text{ km}$  at 40 km altitude to produce sufficient density  $N_s$  of secondaries. These values are lower than observed scales of jets, so that the runaway mechanism may well contribute to their production. In other words, secondary electrons  $N_s$  may play a major role in establishing the current and space charge balance, as well as the general shape of the streamer. Since the thermalization time of secondaries is expected to be very fast at  $\sim 30 \text{ km}$  altitudes, the streamer development in case of ionization by runaway electrons may be similar to that caused by the quasi-electrostatic heating, including the propagation velocity  $v_s \sim 100 \text{ km/s}$ . However, the optical spectra of the resultant emissions may differ since the secondary electrons produced by the runaway process would in general be more energetic [Bell *et al.*, 1995].

# 6

## Summary and Suggestions for Future Research

### 6.1 SUMMARY OF RESULTS

A new form of electrodynamic coupling between thunderstorms and the mesosphere and lower ionosphere has been identified, involving heating, ionization and optical emission effects produced by quasi-electrostatic thundercloud fields, and accounting for the basic features of mesospheric optical emissions called sprites and jets.

Sprites are proposed to be a consequence of large electric field transients capable of causing electron heating, breakdown ionization and excitation of optical emissions at mesospheric altitudes following the removal of a thundercloud charge by a cloud-to-ground discharge. These transients can be produced by the combined action of induced spatially distributed space charge which exists in the region between the thundercloud tops and the lower ionosphere and the charge left in the cloud after the lightning discharge. Results obtained with a two dimensional and selfconsistent model of the nonlinear upward coupling of quasi-electrostatic thundercloud fields are consistent with the observed spectra, temporal duration, and spatial extent of sprites.

The heating of the mesosphere/lower ionosphere by quasi-electrostatic fields can lead to significant modification of the conductivity of these regions. Model calculations predict

significant (several orders of magnitude) modification of the lower ionospheric conductivity in a region with 50-60 km transverse extent. This modification can be in the form of depletions of electron density due to dissociative attachment to  $O_2$  molecules or enhancements of electron density due to breakdown ionization of  $O_2$  and  $N_2$ . Ionization changes produced by consecutive lightning discharges can accumulate, leading to the build up of ionization “bubbles” or attachment “holes” above thunderstorms.

Results of the model calculations corresponding to fast ( $\sim 1$  ms) removal of 100-300 C of thundercloud charge from 10 km altitudes are in good agreement with observations of the upper part (“head” and “hair” [Sentman *et al.*, 1995]) of the sprites. The typical region of brightest optical emission has horizontal and vertical dimensions  $\sim 10$  km, centered at altitudes  $\sim 70$  km and is interpreted as the head of sprite. Our model results also indicate the formation of low intensity glow (“hair”) above this region due to the excitation of optical emissions at altitudes  $\sim 85$  km during the  $\sim 500 \mu s$  at the beginning of the lightning discharge. Comparisons of the optical emission intensity of the 1st and 2nd positive bands of  $N_2$ , Meinel and 1st negative bands of  $N_2^+$ , and 1st negative band of  $O_2^+$  show that the 1st positive band of  $N_2$  is the dominant emission under conditions of heating by quasi-electrostatic thundercloud fields.

The dependencies of quasi-electrostatic heating upon the altitude profile of ion conductivity, number density of electrons and duration of the lightning discharge indicate that the level of optical emissions is defined mainly by the relation between the lightning discharge duration and the conductivity of the upper atmosphere (i.e., relaxation time of the electric field in the conducting medium). For low ambient conductivities the lightning discharge duration can be significantly longer than 1 ms and still produce similar levels of optical emissions. The maximum possible intensity of optical emissions is determined mainly by the value of the removed thundercloud charge and its altitude.

Comparison of the model results for different types of lightning discharges (+CG, -CG, IC) indicate that positive cloud-to-ground discharges lead to the largest electric fields and

optical emissions at ionospheric altitudes, but only because they are typically associated with the removal of larger amounts of charge from higher altitudes. Studies of different geometries of thundercloud charges suggest that spherically distributed charges produce more intense electric fields and optical emissions than horizontally spread charges.

The quasi-electrostatic model of lower ionospheric heating and ionization indicates that most of the observed features of sprites with vertically oriented columnar structure can be explained in terms of the formation and self-driven propagation of streamer type channels of breakdown ionization. Optical emissions of the dominant first positive and second positive bands of molecular nitrogen may form carrot-like vertical structures with typical transverse dimensions of  $\sim 5$ -10 km which can span the altitude range from  $\sim 80$  km to well below  $\sim 50$  km, with detailed structure depending primarily on the time history of charge removal from the thundercloud by the cloud-to-ground lightning discharge. The appearance of optical emissions associated with sprites can be delayed in time ( $\sim 1$ -20 ms) with respect to the causative cloud-to-ground discharge.

Our results indicate that blue jets are streamer type processes occurring on atmospheric spatial scales, with most features of jets as observed in video [Wescott *et al.*, 1995a] being reproduced in the context of the quasi-electrostatic model, including the velocity of upward propagation of  $\sim 100$  km/s, the general shape of jets as upward expanding beams of luminosity with cone angles  $< 30^\circ$ , and the stopping altitudes ( $\sim 50$  km) for jets. Model results are in agreement with video observations showing that the optical brightness drops  $\sim 2$  orders of magnitude between the lower part and the tip of the jet, and the fact that the luminosity fades away simultaneously everywhere along the cone of the jet. The blue color of jets as observed in video is interpreted as the emission from the second positive band of molecular nitrogen excited upon electron impact. Jets are produced during the accumulation phase of the thundercloud charge, so that it is not necessary for large amounts of charge to be removed. Thus, jets are not necessarily associated with lightning discharges and may appear only in relatively rare cases of large ( $\sim 300$ -400C) thundercloud charge accumulation at high ( $\sim 20$  km) altitudes. It is conceivable that a horizontally extended thundercloud



charge distribution, consisting of many charge centers located at lower altitudes ( $< 20\text{km}$ ), may produce the electric field equivalent to that of simple monopole of  $\sim 300\text{-}400\text{C}$  at  $\sim 20\text{ km}$  altitude.

## 6.2 SUGGESTIONS FOR FUTURE RESEARCH

The existing quasi-electrostatic heating model should be extended to treat two fluid equations for the electron and ion components to allow a more general treatment of streamer processes associated with sprites and jets. Important questions not yet addressed concern the chemical and thermal effects produced by quasi-electrostatic fields and runaway electrons associated with sprites and jets in the mesosphere and the selfconsistent modification of the quasi-electrostatic fields by runaway electrons. The existing model should be modified to include the two dimensional dynamics of runaway electrons and their secondary electron products (see Sections 4.8, 5.6). Relative excitation intensities, spatial distribution, and duration of various emissions (ranging from infrared to ultraviolet) stimulated simultaneously by quasi-electrostatic heating and runaway processes need to be evaluated, and criteria should be formulated for comparisons with future spectroscopic measurements of sprites (see discussion in section 4.8). It is important to relate these characteristics to the lightning characteristics and ambient conditions in the atmosphere, mesosphere and lower ionosphere.

Sprites and jets occur under conditions of exceptionally intense electrical and lightning activity which is characteristic of large mesoscale convective systems [e.g., Lyons, 1996]. Recent theoretical and experimental findings [Inan *et al.*, 1996d] suggest that even relatively small quasi-electrostatic fields above thunderclouds are capable of maintaining the ionospheric electrons at a persistently heated level well above their ambient thermal energy. Changes in the thundercloud charge distribution (e.g., in lightning discharges) lead to heating/cooling above/below this quiescent level, and can be experimentally detected as changes in the amplitudes and phases of subionospherically propagating VLF signals

[Inan *et al.*, 1996a,d]. These changes occur simultaneously with lightning discharges, and are referred to as early/fast VLF events. These rapid ionospheric conductivity changes may thus be evidence for thermal and aeronomic coupling between the troposphere and the mesosphere/lower ionosphere regions, with potentially more important (longer term) implications than the spectacular optical displays (i.e., sprites and/or elves) observed during the brief transients immediately after lightning discharges. In view of these findings, an important next step in future research should be to determine the spatial structure and temporal dynamics of long term energy transfer from thunderstorm generated electric fields to the mesosphere/lower ionosphere and to determine the consequences of this deposited energy on the long term chemical balance of the D-region of the ionosphere. Important topics to investigate here would be: (i) the spatial distributions of the temperature and number density of the different kinds of charged particles and the number density of rotationally, vibrationally and optically excited molecules, and (ii) the importance of these effects in the global thermal and chemical balance of the upper atmosphere.

It is also important to investigate whether the variety of observed shapes of sprites can all be explained in terms of the quasi-electrostatic and runaway mechanisms. Lower ionospheric conductivity inhomogeneities (e.g., created by particle precipitation) may play a key role in formation of sprite structures (see section 4.1); possible sources of the electron, ion or neutral density inhomogeneities in the mesosphere/lower ionosphere above thunderstorms need to be investigated. The existing electrodynamic models should be modified to treat typical variety of spatial configurations of such inhomogeneities. The most recent theoretical developments [Pasko *et al.*, 1996d] suggest that heating of the neutral atmosphere above thunderstorms (for which there is some experimental evidence [e.g., Taylor, 1979]) may play an important role in the modulation of the neutral atmospheric density and may lead to the creation of the observed shapes of sprites. The possible means of heating the neutral atmosphere above thunderstorms, for example by internal gravity waves [Taylor, 1979] and through collisional transfer of energy from heated ionospheric electrons to neutrals [Pasko *et al.*, 1996d] should also be investigated.



# A

## Comparison with Kinetic Solutions and Swarm Experiments

In this appendix, we evaluate the validity of parametric approximations for mobility, ionization, attachment and optical excitation rates (Sections 2.4.1, 2.4.2, 2.4.3, 2.5) with the results of kinetic solutions [Taranenko *et al.*, 1993a,b] and with the results of the electron swarm experiments where available [e.g., Davies, 1983]. For this purpose, we consider the altitude profile (at  $r = 0$ ) of the electric field which approximately corresponds to a charge of 300 C placed at 10 km altitude km (M2 model from Figure 2.1). We then divide the altitude range from 10 to 90 km in equidistant intervals with 1 km steps. At each altitude, the value of the electric field is divided into 50 linear intervals so that the first value is 0 and last value is the maximum value of the electric field at this altitude. The resulting discretization of the electric fields and altitudes is illustrated in Figure A.1. The stationary electron distribution function  $f(v)$  corresponding to the each of the points shown in Figure A.1 (i.e., for different electric fields and densities of atmospheric gas) is obtained from the solution of the Boltzman equation, taking into account inelastic collisions consisting of rotational, vibrational, optical, dissociative, dissociative with attachment and ionizational losses [Taranenko *et al.*, 1993a]. The mobility, ionization, attachment and optical excitation rates are calculated using the obtained distribution functions and known cross sections for these processes [Taranenko *et al.*, 1993a,b]. Results obtained with this approach are directly comparable to swarm laboratory experiments [e.g., Davies, 1983] in which when the



electron mobility is measured for different magnitudes of applied electric fields and ambient neutral gas densities.

### A.1 ELECTRON MOBILITY

The electron mobility can be calculated as

$$\mu_e = \frac{1}{EN_e} \int v f(v) d^3v \quad (\text{A.1})$$

where the distribution function is assumed to be normalized so that  $N_e = \int f(v) d^3v$ . Results are shown in Figure A.1b by dots. We also show the corresponding values obtained from experimental measurements by *Davies* [1983] (open circles) and those obtained using the analytical approximation (2.5) (dashed line). For lower values of the electric fields ( $EN_o/N < 10^4$  V/m) the analytic approximation (2.5) is supported by measurements of *Hegerberg and Reid* [1980] (not shown). The normalized mobility values of  $\mu_e N/N_o = 1.36$  m<sup>2</sup>/V/s for  $EN_o/N < 1.62 \times 10^3$  V/m corresponds to the thermal state of the electrons (with no heating). The value of the mobility in this region of electric fields is found to be in good agreement with that derived from hydrodynamic equations using effective collision frequencies and average fractions of energy transferred in one collision from electrons to neutrals at an electron temperature  $T_e = 200$  K [*Gurevich*, 1978, pp. 32, 99, 103]. The results of the three different approaches (kinetic, experimental, analytical) shown in Figure A.1b agree with each other reasonably well.

### A.2 IONIZATION AND ATTACHMENT COEFFICIENTS

The ionization  $\nu_i$  and attachment  $\nu_a$  coefficients can be calculated as:

$$\nu_i = \frac{N}{N_e} \int v f(v) \sigma_i(v) d^3v, \quad (\text{A.2})$$

$$\nu_a = \frac{N_{O_2}}{N_e} \int v f(v) \sigma_a(v) d^3v, \quad (\text{A.3})$$

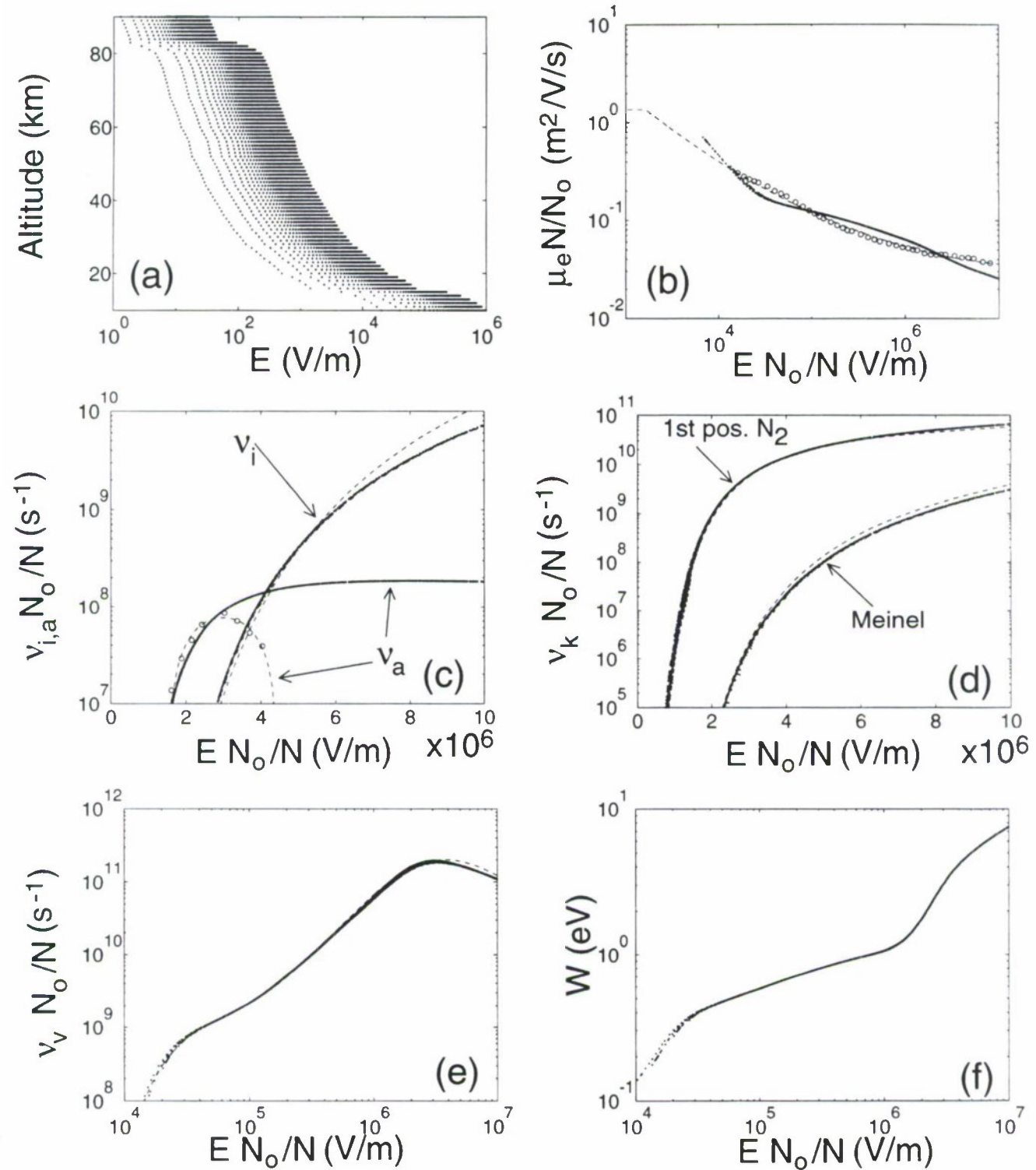


**Fig. A.1. Comparison of analytical approximations with kinetic solutions and results of swarm experiments.** (a) The discretization of altitudes and electric field values for the kinetic solutions; (b) The electron mobility corresponding to different models is shown in the same format as in Figure 2.5; (c) The ionization and attachment coefficients corresponding to different models are shown in the same format as in Figure 2.6; (d) The excitation coefficients of selected optical bands corresponding to different models are shown in the same format as in Figure 2.7; (e) The excitation coefficient of vibrationally excited  $N_2$  molecules; (f) The average energy of the electron distribution.

where  $\sigma_i$  and  $\sigma_a$  are corresponding cross sections. Comparison of the results of kinetic calculations (A.2), (A.3) (dots) and the analytical approximations (2.6) (2.7) (dashed lines) for  $\nu_i$  and  $\nu_a$  are shown in the Figure A.1c. For the attachment coefficient we also show results of experimental measurements by *Davies* [1983] (open circles). We note once again the reasonable agreement between the different approaches. For the electron attachment coefficient in the range of electric fields  $EN_o/N > 4 \times 10^6$  V/m we see a significant difference between the experimental data and the results of kinetic solutions (most probably caused by detachment effects as discussed in [*Davies*, 1983]); however, in this region of electric fields the attachment coefficient becomes much smaller than the ionization coefficient so that the relative inaccuracy of the parametric model does not affect our numerical results.

### A.3 OPTICAL EMISSIONS

The excitation rate per one electron of a given energy state  $k$  for a particular species  $j$  has the value:

$$\nu_k = \frac{N_j}{N_e} \int v f(v) \sigma_k(v) d^3v, \quad (\text{A.4})$$

where  $\sigma_k$  is the cross section for excitation of state  $k$ . For the sake of brevity in Figure A.1d we show only results corresponding to the excitation rates of the 1st positive band of  $N_2$  and the Meinel band of  $N_2^+$ . The comparison between kinetic solutions (A.4) (dots) and the analytical approximations (2.10) (dashed lines) demonstrate that the later can be used with negligible error, as we have done in our model calculations.

### A.4 VIBRATIONAL EXCITATION OF MOLECULAR NITROGEN

In Figure A.1e we show the excitation rate (per one electron) of the vibrationally excited  $N_2$  molecules:

$$\nu_v = \frac{N_2}{N_e} \int v f(v) \sigma_v(v) d^3v, \quad (\text{A.5})$$

where  $\sigma_v$  is the cross section corresponding to this process [Taranenko, 1993]. Although not discussed in this thesis, production of vibrationally excited  $N_2$  molecules may play an important role in the chain of reactions leading to  $4.3 \mu\text{m}$  infrared emissions of  $CO_2$  [e.g., Picard *et al.*, 1987]. Results of kinetic solutions in this case can also be approximated by a relatively simple analytical formula:

$$\log(\nu_v \frac{N_o}{N}) = \sum_{i=0}^5 a_i x^i \quad (\text{A.6})$$

where  $x = \log(\frac{EN_o}{N})$ , and  $a_0 = -1284.6$ ,  $a_1 = 1154.1$ ,  $a_2 = -408.37$ ,  $a_3 = 71.513$ ,  $a_4 = -6.1882$ ,  $a_5 = 0.21158$ , which is shown in Figure A.1e by a dashed line. The approximation given by (A.5) is valid for the range of electric fields  $10^4 < EN_o/N < 10^7 \text{V/m}$ .

## A.5 AVERAGE ELECTRON ENERGY

For illustrative purposes in Figure A.1f we provide the average energy of the electron distribution

$$W = \frac{1}{N_e} \int \frac{m_e v^2}{2} f(v) d^3 v \quad (\text{A.7})$$

as a function of the electric field. Calculations show that even in cases of relatively strong ionization, as shown in Figure 3.4 for the removed charge 250 C, the peak average energy of the electron distribution does not exceed  $\sim 5 \text{ eV}$ , indicating that most of the ionization is produced by the relatively small number of electrons in the tail of the electron distribution function which appear in the region of energies of  $\sim 15 \text{ eV}$  (corresponding to ionization threshold of  $N_2$  and  $O_2$ ).





# B

## Comparison with Auroral Optical Emissions

It is interesting to compare the spectral content of optical emissions associated with aurorae and those produced at the same altitudes by electrons heated by electric fields resulting from intensive cloud to ground lightning discharges.

The typical omnidirectional flux of auroral electrons (in erg/cm<sup>2</sup>/s/eV) can be approximated by the expression [Meier *et al.*, 1989]:

$$\Phi(\mathcal{E}) = \Phi_M(\mathcal{E}) + 0.4\Phi_{\max} \frac{\mathcal{E}'}{\mathcal{E}} e^{-\frac{\mathcal{E}}{b}}, \quad (\text{B.1})$$

where

$$\Phi_M(\mathcal{E}) = \frac{P}{2\pi(\mathcal{E}')^3} e^{-\frac{\mathcal{E}}{\mathcal{E}'}} \quad (\text{B.2})$$

and  $\Phi_{\max}$  is the maximum value of  $\Phi_M$ ,  $\mathcal{E}$  is energy in keV, and  $b = 0.8\mathcal{E}'$  if  $\mathcal{E}' < 0.5$  keV, or  $b = 0.1\mathcal{E}' + 0.35$  if  $\mathcal{E}' \geq 0.5$  keV,  $\mathcal{E}$  is the characteristic energy, and  $P$  is the energy flux. The excitation rate of the  $k$ th excitation process involving the  $j$ th species can be calculated as:

$$\nu_k = N_j \int_{\mathcal{E}} \Phi(\mathcal{E}) \sigma_k(\mathcal{E}) d\mathcal{E}, \quad (\text{B.3})$$

where  $\sigma_k$  corresponds to  $k$ th excitation process cross section.

Results of calculations of  $\nu_k$  using (B.3) for selected optical bands and range of the characteristic energies  $\mathcal{E}'$  0.1-10 keV for  $P = 30$  ergs/cm<sup>2</sup>/s are shown in Figure B.1b along with the electron flux for three selected values of  $\mathcal{E}'$  (Figure B.1a). The 1st negative and Meinel bands of  $N_2^+$  are clearly dominant, and the auroral emissions exhibit a rich spectral complexity in comparison with those produced by quasi-electrostatic fields (e.g., Figure 3.9b).

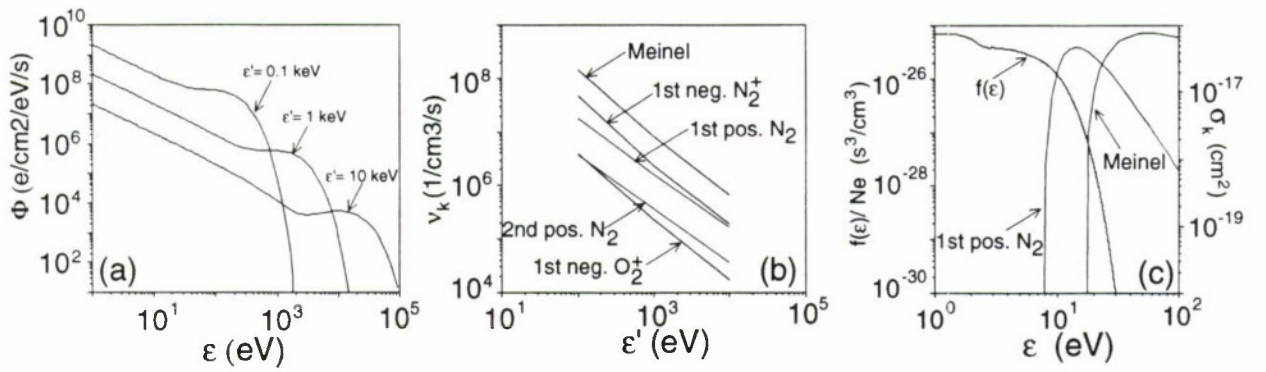


**Fig. B.1. Comparison with auroral optical emissions.** (a) Omnidirectional flux of auroral electrons; (b) Excitation rates of selected optical bands corresponding to (a) ; (c) Typical distribution function of heated electrons and cross sections of the optical excitation of 1st positive band of  $N_2$  and Meinel band of  $N_2^+$ .

Figure B.1b shows the excitation rates rather than the emission rates. At altitudes of  $\sim 85$  km used for our calculations, the Meinel  $N_2^+$  band is quenched, since the quenching height for this band is  $\sim 90$  km. The resulting emission rate is thus  $\sim 2$ -3 times lower than the excitation rate plotted in Figure B.1b. The rest of the bands shown have quenching heights much lower than 85 km so that the corresponding excitation rates can be interpreted as emission rates.

The primary reason for the spectral differences between in the auroral precipitation and quasi-electrostatic heating cases is the relative structure of the electron distribution function as a function of energy and the corresponding excitation cross sections. In the case of electron heating by quasi-static electric fields, the distribution function sharply decreases

with increasing energy in the region of electron energies of 10-15 eV (due to the effective loss of electron energy as a result of inelastic collisions [*Taranenko et al.*, 1993]) as illustrated in Figure B.1c, for  $h = 85$  km and an applied electric field of 45 V/m. For illustration, the distribution of excitation cross sections for  $N_2$  1st positive and  $N_2^+$  Meinel bands [*Taranenko*, 1993] are also shown in Figure B.1c. In the auroral case, the distribution function has a wide extent and covers a broad energy range up to  $10^4$ -  $10^5$  eV (Figure B.1a). In simpler terms, the secondary electron distribution in aurorae are produced by impact of higher energy precipitating electrons and thus has a distribution with larger numbers of electrons at higher energies.





# Bibliography

- Armstrong, W. C., Recent advances from studies of the Trimpi effect, *Antarctic J.*, 18, 281, 1983.
- Baginski, M. E., L. C. Hale, and J. J. Olivero, Lightning-related fields in the ionosphere, *Geophys. Res. Lett.*, 15, 764, 1988.
- Baginski, M. E., and A. S. Hodel, A case study comparing the lossy wave equation to the continuity equation in modeling late-time fields associated with lightning, *Applied Computational Electromagnetics Society Journal*, 9, 98, 1994.
- Bell, T. F., V. P. Pasko, and U. S. Inan, Runaway electrons as a source of Red Sprites in the mesosphere, *Geophys. Res. Lett.*, 22, 2127, 1995.
- Boccippio, D.J., E. R. Williams, S. J. Heckman, W. A. Lyons, I. T. Baker, and R. Boldi, Sprites, ELF transients, and positive ground strokes, *Science*, 269, 1088, 1995.
- Boeck, W. L., O. H. Vaughan, Jr., R. Blakeslee, B. Vonnegut, and M. Brook, Lightning induced brightening in the airglow layer, *Geophys. Res. Lett.*, 19, 99, 1992.
- Boeck, W. L., O. H. Vaughan, R. J. Blakeslee, B. Vonnegut, M. Brook, and J. McKune, Observations of lightning in the stratosphere, *J. Geophys. Res.*, 100, 1465, 1995.
- Braham, Jr., R.R. The water and energy budgets of the thunderstorm and their relation to thunderstorm development, *J. Meteor.*, 9, 227, 1952.
- Brook, M., M. Nakano, P. Krehbiel, and T. Takeuti, The electrical structure of the Hokuriku winter thunderstorms, *J. Geophys. Res.*, 87, 1207, 1982.

- Buneman, O., A compact non-iterative Poisson-solver, *SUIPR report No. 294*, Stanford University, 1969.
- Chamberlain, J. W., *Theory of planetary atmospheres*, Academic Press, New York, 1978.
- Davies, D.K., Measurements of swarm parameters in dry air, *Theoretical Notes*, Note 346, Westinghouse R&D Center, Pittsburg, May, 1983.
- Dejnakarintra, M., and C. G. Park, Lightning-induced electric fields in the ionosphere, *J. Geophys. Res.*, 79, 1903, 1974.
- Dhali, S.K., and P. F. Williams, Two-dimensional studies of streamers in gases, *J. Appl. Phys.*, 62, 4696, 1987.
- Dowden, R. L., C. D. C. Adams, J. B. Brundell and P. E. Dowden, Rapid onset, rapid decay (RORD), phase and amplitude perturbations of VLF subionospheric transmissions, *J. Atmos. Terr. Phys.*, 56, 1513, 1994.
- Fishman, G. J., P. N. Bhat, R. Mallozzi, J. M. Horack, T. Koshut, C. Kouveliotou, G. N. Pendleton, C. A. Meegan, R. B. Wilson, W. S. Paciesas, S. J. Goodman, and H. J. Christian, Discovery of intense gamma-ray flashes of atmospheric origin, *Science*, 264, 1313, 1994.
- Franz, R. C. et al., Television image of a large upward electric discharge above a thunderstorm system, *Science*, 249, 48, 1990.
- Fukunishi, H., Y. Takahashi, M. Kubota, K. Sakanoi, U. S. Inan, and W. A. Lyons, Lightning-induced transient luminous events in the lower ionosphere, *Geophys. Res. Lett.*, in press, 1996.
- Glukhov, V. S., V. P. Pasko, and U. S. Inan, Relaxation of transient lower ionospheric disturbances caused by lightning-whistler-induced electron precipitation bursts, *J. Geophys. Res.*, 97, 16971, 1992.
- Grange, F., N. Soulem, J. F. Loiseau, and N. Spyrou, Numerical and experimental determination of ionizing front velocity in a DC point-to-plane corona discharge, *J. Phys. D: Appl. Phys.*, 28, 1619, 1995.
- Greifinger, C., and P. Greifinger, Transient ULF electric and magnetic fields following a lightning discharge, *J. Geophys. Res.*, 81, 2237, 1976.

- Griffiths, R. F., and C. T. Phelps, A model of lightning initiation arising from positive corona streamer development, *J. Geophys. Res.*, **31**, 3671, 1976.
- Grigor'ev, A. I., and S. O. Shiryayeva, Mechanism for development of the stepped leader and intracloud branching of streak lightning, *Sov. Phys. Tech. Phys.*, **34**, 502, 1989.
- Gurevich, A. V., *Nonlinear phenomena in the ionosphere*, Berlin: Springer-Verlag, 1978.
- Gurevich, A. V., G. M. Milikh, and R. A. Roussel-Dupre, Runaway electron mechanism of air breakdown and preconditioning during a thunderstorm, *Phys. Lett. A*, **165**, 463, 1992.
- Gurevich, A. V., G. M. Milikh, and R. A. Roussel-Dupre, Nonuniform runaway air- breakdown, *Phys. Lett. A*, **187**, 197, 1994.
- Hale, L. C., and M. E. Baginski, Current to the ionosphere following a lightning stroke, *Nature*, **329**, 814, 1987.
- Hale, L. C., Coupling of ELF/ULF energy from lightning and MeV particles to the middle atmosphere, ionosphere, and global circuit, *J. Geophys. Res.*, **99**, 21089, 1994.
- Hampton, D. L., M. J. Heavner, E. M. Wescott, and D. D. Sentman, Optical spectral characteristics of sprites, *Geophys. Res. Lett.*, **22**, 89, 1996.
- Hegerberg, R., and I. D. Reid, Electron drift velocities in air, *Aust. J. Phys.*, **33**, 227, 1980.
- Holden, D. N., C. P. Munson, and J. C. Devenport, Satellite observations of transionospheric pulse pairs, *Geophys. Res. Lett.*, **22**, 889, 1995.
- Holzer, R. E., D. S. Saxon, Distribution of electrical conduction currents in the vicinity of thunderstorms, *J. Geophys. Res.*, **57**, 207, 1952.
- Holzworth, R. H., M. C. Kelley, C. L. Siefring, L. C. Hale and J. T. Mitchell, Electrical measurements in the atmosphere and the ionosphere over an active thunderstorm. 2. Direct current electric fields and conductivity, *J. Geophys. Res.*, **90**, 9824, 1985.
- Idone, V.P., A.B. Saljoughy, R. W. Henderson, P. K. Moore, and R. B. Pyle, A reexamination of the peak current calibration of the National Lightning Detection Network, *Geophys. Res. Lett.*, **98**, 18323, 1993.
- Illingworth, A. J., Electric field recovery after lightning as the response of the conducting atmosphere to a field change, *Quart. J. R. Met. Soc.*, **98**, 604, 1972.



- Inan, U. S., D. C. Shafer, W. Y. Yip, and R. E. Orville, Subionospheric VLF signatures of nighttime D-region perturbations in the vicinity of lightning discharges, *J. Geophys. Res.*, **93**, 11455, 1988.
- Inan, U. S., T. F. Bell, and J. V. Rodriguez, Heating and ionization of the lower ionosphere by lightning, *Geophys. Res. Lett.*, **18**, 705, 1991.
- Inan, U. S., J. V. Rodriguez, and V. P. Idone, VLF signatures of lightning-induced heating and ionization of the nighttime D-region, *Geophys. Res. Lett.*, **20**, 2355, 1993.
- Inan, U. S., T. F. Bell, V. P. Pasko, D. D. Sentman, and E. M. Wescott, and W. A. Lyons, VLF signatures of ionospheric disturbances associated with sprites, *Geophys. Res. Lett.*, **22**, 3461, 1995.
- Inan, U. S., A. Slingeland, V. P. Pasko, and J. Rodriguez, VLF signatures of mesospheric/lower ionospheric response to lightning discharges, *J. Geophys. Res.*, **101**, 5219, 1996a.
- Inan, U. S., W. A. Sampson, and Y. N. Taranenko, Space-time structure of lower ionospheric optical flashes and ionization changes produced by lightning EMP, *Geophys. Res. Lett.*, **23**, 133, 1996b.
- Inan, U. S., S. C. Reising, G. J. Fishman, and J. M. Horack, On the association of terrestrial gamma-ray bursts with lightning discharges and sprites, *Geophys. Res. Lett.*, **23**, 1017, 1996c.
- Inan, U. S., V. P. Pasko, and T. F. Bell, 'Early/Fast VLF events as evidence of sustained heating of the ionosphere above thunderclouds, *Geophys. Res. Lett.*, **23**, 1067, 1996d.
- Lagarkov, A. N., and I. M. Rutkevich, *Ionization waves in electrical breakdown in gases*, Springer-Verlag, New York, 1994.
- Lowke, J. J., Theory of electrical breakdown in air - the role of metastable oxygen molecules, *J. Phys. D: Appl. Phys.*, **25**, 202, 1992.
- Lyons, W. A., Characteristics of luminous structures in the stratosphere above thunderstorms as imaged by low-light video, *Geophys. Res. Lett.*, **21**, 875, 1994.
- Lyons, W. A., Low-light video observations of frequent luminous structures in the stratosphere above thunderstorms, *Monthly Weather Review*, **122**, 1940, 1995.

- Lyons, W. A., Sprite observations above the U.S. high plains in relation to their parent thunderstorm systems, *J. Geophys. Res.*, in review, 1996.
- Malan, D. J., *Physics of lightning*, The English Universities Press Ltd, London, 1963.
- Marshall, T. C., and W. D. Rust, Two types of vertical electrical structures in stratiform precipitation regions of mesoscale convective systems, *Bull. Amer. Meteor. Soc.*, 74, 2159, 1993.
- Marshall, T. C., M. Stolzenburg, W. D. Rust, Electric field measurements above mesoscale convective systems, *J. Geophys. Res.*, 101, 6979, 1996.
- McCarthy, M. P., and G. K. Parks, On the modulation of X Ray fluxes in thunderstorms, *J. Geophys. Res.*, 97, 5857, 1992.
- Mende, S. B., R. L. Rairden, and G. R. Swenson, and W. A. Lyons, Sprite spectra: N<sub>2</sub> I PG band identification, *Geophys. Res. Lett.*, 22, 2633, 1995.
- Meier, R. R., D. J. Strickland, J. H. Hecht, and A. B. Christensen, Deducing composition and incident electron spectra from ground-based auroral optical measurements: A study of auroral red line processes, *J. Geophys. Res.*, 94, 13541, 1989.
- Morrill, J., B. A. Garragher, and W. Benesh, Population development of auroral molecular nitrogen species in a pulsed electric discharge, *J. Geophys. Res.*, 93, 963, 1988.
- Milikh, G. M., K. Papadopoulos, C. L. Chang, On the physics of high altitude lightning, *Geophys. Res. Lett.*, 22, 85, 1995.
- Ogawa, T., Fair-weather electricity, *J. Geophys. Res.*, 90, 5951, 1985.
- Orville, R. E., Calibration of a magnetic direction finding network using measured triggered lightning return stroke peak currents, *J. Geophys. Res.*, 96, 17135, 1991.
- Papadopoulos, K., G. Milikh, A. Gurevich, A. Drobot, and R. Shanny, Ionization rates for atmospheric and ionospheric breakdown, *J. Geophys. Res.*, 98, 17593, 1993.
- Pasko, V. P., and U. S. Inan, Recovery signatures of lightning-associated VLF perturbations as a measure of the lower ionosphere, *J. Geophys. Res.*, 99, 17,523, 1994.
- Pasko, V. P., U. S. Inan, Y. N. Taranenko, and T. F. Bell, Heating, ionization and upward discharges in the mesosphere due to intense quasi-electrostatic thundercloud fields, *Geophys. Res. Lett.*, 22, 365, 1995.

- Pasko, V. P., U. S. Inan, and T. F. Bell, Sprites as luminous columns of ionization produced by quasi-electrostatic thundercloud fields, *Geophys. Res. Lett.*, 23, 649, 1996a.
- Pasko, V. P., U. S. Inan, and T. F. Bell, Blue jets produced by quasi-electrostatic pre-discharge thundercloud fields, *Geophys. Res. Lett.*, 23, 301, 1996b.
- Pasko, V. P., U. S. Inan, T. F. Bell, and Y. N. Taranenko, Sprites produced by quasi-electrostatic heating and ionization in the lower ionosphere, *J. Geophys. Res.*, in review, 1996c.
- Pasko, V. P., U. S. Inan, and T. F. Bell Ionospheric Effects due to Electrostatic Thundercloud Fields, *Geophys. Res. Lett.*, in review, 1996d.
- Petrov, N. I., V. R. Avanskii, and N. V. Bombenkova, Measurements of the electric field in the streamer zone and in the sheath of the channel of a leader discharge, *Tech. Phys.*, 39, 546, 1994.
- Potter, D., *Computational physics*, John Wiley & Sons, London, 1973.
- Picard, R. H., J. R. Winick, R. D. Sharma, A. S. Zachor, P. J. Espy, and C. R. Harris, Interpretation of infrared measurements of the high-latitude thermosphere from a rocket-borne interferometer, *Adv. Space Res.*, 7, (10)23, 1987.
- Rairden, R. L., and S. B. Mende, Time resolved sprite imagery, *Geophys. Res. Lett.*, 22, 3465, 1995.
- Reid, G. C., The middle atmosphere, *NASA CP-2090*, National Aeronautics and Space Administration, 27-42, 1979.
- Roussel-Dupre, R. A., A. V. Gurevich, T. Tunnell, and G. M. Milikh, Kinetic theory of runaway air breakdown, *Phys. Rev. E*, 49, 2257, 1994.
- Roussel-Dupre, R. A., and A. V. Gurevich, On runaway breakdown and upward propagating discharges, *J. Geophys. Res.*, 101, 2297, 1996.
- Rowland, H. L., R. F. Fernsler, J. D. Huba, and P. A. Bernhardt, Lightning driven EMP in the upper atmosphere, *Geophys. Res. Lett.*, 22, 361, 1995.
- Rust, W. D., T. C. Marshall, M. Stolzenburg, M. G. Boteman, T. R. Shepherd, B. F. Smull, Observations of electrical structure of midlatitude mesoscale convective systems: Review and update, in *Proceedings of 10th International Conference on Atmospheric Electricity*, p. 108, Osaka, Japan, June 10-14, 1996.



- Sentman, D. D., and E. M. Wescott, Observations of upper atmospheric optical flashes recorded from an aircraft, *Geophys. Res. Lett.*, 20, 2857, 1993.
- Sentman, D. D., and E. M. Wescott, *Red sprites and blue jets*, Geophysical Institute Video Production, University of Alaska, Fairbanks, 9 July, 1994.
- Sentman, D. D., and E. M. Wescott, Red sprites and blue jets: Thunderstorm-excited optical emissions in the stratosphere, mesosphere, and ionosphere, *Phys. Plasmas*, 2, 2514, 1995.
- Sentman, D. D., E. M. Wescott, D. L. Osborne, D. L. Hampton, and M. J. Heavner, Preliminary results from the Sprites94 campaign: Red Sprites, *Geophys. Res. Lett.*, 22, 1205, 1995.
- Sipler, D. P., and M. A. Biondi, Measurements of  $O(^1D)$  quenching rates in the *F* region, *J. Geophys. Res.*, 77, 6202, 1972.
- Stergis, C.G., G.C. Rein, and T. Kangas, Electric field measurements in the stratosphere *J. Atmos. Terr. Phys.*, 11, 77, 1957.
- Swarztrauber, P., and R. Sweet, Efficient FORTRAN subprograms for the solution of elliptic partial differential equations, *NCAR Technical Note*, NCAR/TN-109+IA, July, 1975.
- Taranenko, Y. N., U. S. Inan, and T. F. Bell, Interaction with the lower ionosphere of electromagnetic pulses from lightning: heating, attachment, and ionization, *Geophys. Res. Lett.*, 20, 1539, 1993a.
- Taranenko, Y. N., U. S. Inan, and T. F. Bell, The interaction with the lower ionosphere of electromagnetic pulses from lightning: excitation of optical emissions, *Geophys. Res. Lett.*, 20, 2675, 1993b.
- Taranenko, Y. N., Interaction with the lower ionosphere of electromagnetic pulses from lightning: heating, attachment, ionization, and optical emissions, Ph.D. dissertation, Stanford Univ., Calif., September, 1993.
- Taranenko, Y. N., and R. A. Roussel-Dupre, High altitude discharges and gamma-ray flashes: a manifestation of runaway air breakdown, *Geophys. Res. Lett.*, 23, 571, 1996.
- Taylor, L. L., Mesospheric heating due to intense tropospheric convection, NASA Contractor Report 3132, Washington, D. C., 1979.



- Tzur, I. and R. G. Roble, The interaction of a polar thunderstorm with its global electrical environment, *J. Geophys. Res.*, **90**, 5989, 1985.
- Valence-Jones, A., *Aurora*, D. Reidel publishing Co., Dordrecht, 1974.
- Vaughan, O. H., Jr., and B. Vonnegut, Recent observations of lightning discharges from the top of a thunderstorm into the clear air above, *J. Geophys. Res.*, **94**, 13179, 1989.
- Vaughan, O. H., Jr., R. J. Blakeslee, W. L. Boeck, B. Vonnegut, M. Brook, and J. McKune Jr., A cloud-to-space lightning as recorded by the space shuttle payload-bay TV cameras, *Mon. Weather Rev.*, **120**, 1459, 1992.
- Volland H., Atmospheric Electrodynamics, *Springer-Verlag*, New York, 1984.
- Vitello, P. A., B. M. Penetrante, and J. N. Bardsley, Simulation of negative-streamer dynamics in nitrogen, *Phys. Rev. E*, **49**, 5574, 1994.
- Wen, C., and J. M. Wetzler, Electron avalanches influenced by detachment and conversion processes, *IEEE Trans. Electr. Insul.*, **23**, 999, 1988.
- Wescott, E. M., D. Sentman, D. Osborne, D. Hampton, and M. Heavner, Preliminary results from the Sprites94 aircraft campaign: 2. Blue jets, *Geophys. Res. Lett.*, **22**, 1209, 1995a.
- Wescott, E.M., D. D. Sentman, M. J. Heavner, and D. L. Hampton, Blue starters, discharges above an intense thunderstorm over Arkansas, July 1, 1994, *EOS Trans. AGU, 1995 Fall Meeting*, **76**, F104, 1995b.
- Wescott, E. M., D. D. Sentman, M. J. Heavner, D. L. Hampton, D. L. Osborne, and O. H. Vaughan Jr., Blue Starters: Brief upward discharges from intense arkansas thunderstorm, *Gephys. Res. Lett.*, **23**, in press, 1996.
- Wilson, C. T. R., The electric field of a thundercloud and some of its effects, *Proc. Phys. Soc. London*, **37**, 32D, 1925.
- Wilson, C. T. R., A theory of thundercloud electricity, *Proc. R. Soc. London Ser A*, **236**, 297, 1956.
- Winckler, J. R., Further observations of cloud-ionosphere electrical discharges above thunderstorms, *J. Geophys. Res.*, **100**, 14335, 1995.
- Winckler, J. R., W. A. Lyons, T. Nelson, and R. J. Nemzek, New high-resolution ground-based studies of cloud-ionosphere discharges over thunderstorms (CI or Sprites), *J. Geophys. Res.*, **101**, 6997, 1996.

Uman, M. A., *Lightning*, Dover Publications, 1984.

Uman, M.A., *The lightning discharge*, Academic Press, Orlando, 1987.

Uman, M.A., The earth and its atmosphere as a leaky spherical capacitor, *Am. J. Phys.*, 42, 1033, 1974.